EUROPEAN ORGANIZATION FOR NUCLEAR RESEARCH (CERN)

FERMILAB-PUB-15-070-CMS

CERN-PH-EP/2015-004
2015/02/11

CMS-EGM-13-001

Performance of electron reconstruction and selection with the CMS detector in proton-proton collisions at $\sqrt{s} = 8$ TeV

The CMS Collaboration*

arXiv:1502.02701v1 [physics.ins-det] 9 Feb 2015

Abstract

The performance and strategies used in electron reconstruction and selection at CMS are presented based on data corresponding to an integrated luminosity of 19.7 fb^{-1}, collected in proton-proton collisions at $\sqrt{s} = 8$ TeV at the CERN LHC. The paper focuses on prompt isolated electrons with transverse momenta ranging from about 5 to a few 100 GeV. A detailed description is given of the algorithms used to cluster energy in the electromagnetic calorimeter and to reconstruct electron trajectories in the tracker. The electron momentum is estimated by combining the energy measurement in the calorimeter with the momentum measurement in the tracker. Benchmark selection criteria are presented, and their performances assessed using Z, Y, and J/ψ decays into e^++e^- pairs. The spectra of the observables relevant to electron reconstruction and selection as well as their global efficiencies are well reproduced by Monte Carlo simulations. The momentum scale is calibrated with an uncertainty smaller than 0.3%. The momentum resolution for electrons produced in Z boson decays ranges from 1.7 to 4.5%, depending on electron pseudorapidity and energy loss through bremsstrahlung in the detector material.

Submitted to the Journal of Instrumentation

© 2015 CERN for the benefit of the CMS Collaboration. CC-BY-3.0 license

*See Appendix A for the list of collaboration members

Contents

1 Introduction . . . 1
2 CMS detector . . . 3
3 Data and simulation . . . 4
4 Electron reconstruction . . . 6
4.1 Clustering of electron energy in the ECAL . . . 6
4.2 Electron track reconstruction . . . 8
4.3 Electron particle-flow clustering . . . 13
4.4 Association between track and cluster . . . 14
4.5 Resolving ambiguity . . . 14
4.6 Relative ECAL to tracker alignment with electrons . . . 15
4.7 Charge estimation . . . 15
4.8 Estimation of electron momentum . . . 16
5 Electron selection . . . 25
5.1 Identification . . . 25
5.2 Isolation requirements . . . 30
5.3 Rejection of converted photons . . . 31
5.4 Reference selections . . . 33
6 Electron efficiencies and misidentification probabilities . . . 34
6.1 Reconstruction efficiency . . . 35
6.2 Selection efficiency . . . 37
6.3 Misidentification probability . . . 39
7 Summary and conclusions . . . 39
A The CMS Collaboration . . . 47

1 Introduction

Electron reconstruction and selection is of great importance in many analyses performed using data from the CMS detector, such as standard model precision measurements, searches and measurements in the Higgs sector, and searches for processes beyond the standard model. These scientific analyses require excellent electron reconstruction and selection efficiencies together with small misidentification probability over a large phase space, excellent momentum resolution, and small systematic uncertainties. A high level of performance has been achieved in steps, evolving from the initial algorithms for electron reconstruction developed in the context of online selection [1]. The basic principles of offline electron reconstruction, outlined in the CMS Physics Technical Design Report [2, 3], rely on a combination of the energy measured in the electromagnetic calorimeter (ECAL) and the momentum measured in the tracking detector (tracker), to optimize the performance over a wide range of transverse momentum (p_{T}). Throughout the paper, "energy" and "momentum" refer, respectively, to the energy of the electromagnetic shower initiated by the electron in the ECAL and to the track momentum measurement in the tracker, while the term "electron momentum" is used to refer to the combined information. The energy calibration and resolution in the ECAL were discussed in Ref. [4], and general issues in track reconstruction in Ref. [5]. Preliminary results on electron reconstruction and selection were also given in Refs. [6–8]. One of the main challenges for precise reconstruction of electrons in CMS is the tracker material, which causes significant bremsstrahlung along

the electron trajectory. In addition, this bremsstrahlung spreads over a large volume due to the CMS magnetic field. Dedicated techniques have been developed to account for this effect [3]. These procedures have been optimized using simulation, and commissioned with data taken since 2009.

This paper describes the reconstruction and selection algorithms for isolated primary electrons, and their performance in terms of momentum calibration, resolution, and measured efficiencies. The results are based on data collected in proton-proton collisions at $\sqrt{s} = 8\,\text{TeV}$ at the CERN LHC that correspond to an integrated luminosity of $19.7\,\text{fb}^{-1}$. Figure 1 shows the two-electron invariant mass spectrum from data collected with dielectron triggers. The step near 40 GeV is due to the thresholds used in the triggers. The J/ψ, ψ(2S), Υ(1S), the overlapping Υ(2S) and Υ(3S) mesons, and the Z boson resonances can be seen, and are used to assess the performance of the electron momentum calibration and resolution, and to measure the reconstruction and selection efficiencies.

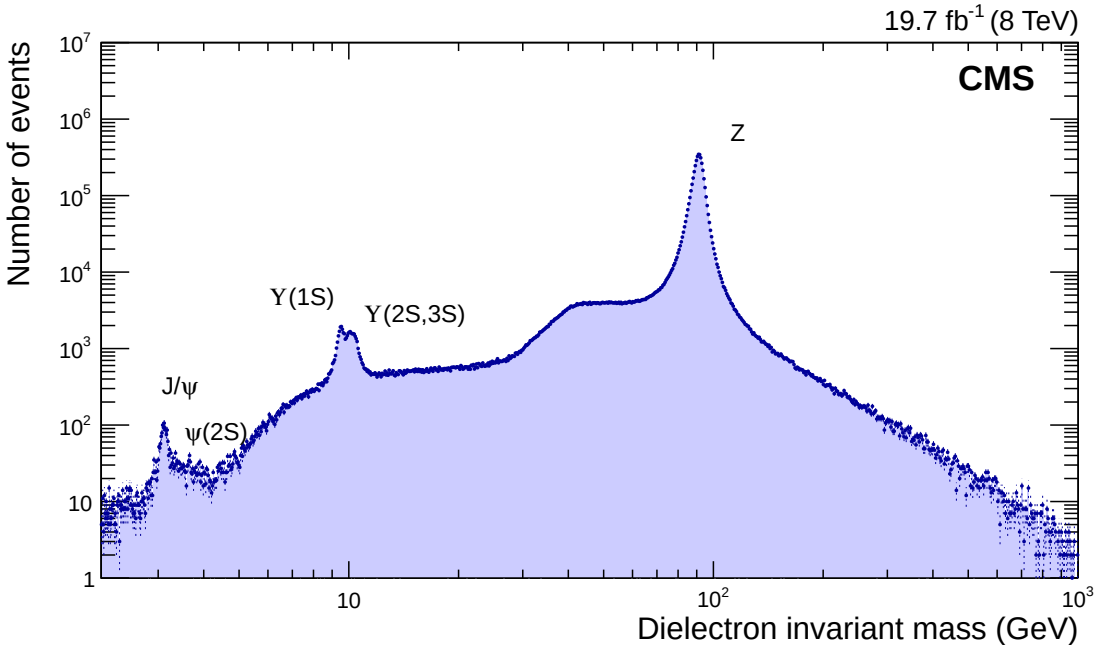

Figure 1: Two-electron invariant mass spectrum for data collected with dielectron triggers. Electron momenta are obtained by combining information from the tracker and the ECAL.

A crucial and challenging process used as a benchmark in the paper is the decay of the Higgs boson into four leptons through on-shell Z boson and virtual Z boson (Z*) intermediate states [9]. In the case of a decay into four electrons or two muons and two electrons, one electron can have a very small p_{T} that requires good performance down to $p_{\text{T}} \approx 5\,\text{GeV}$. At the other extreme, electrons with p_{T} above a few 100 GeV are often used to search for high-mass resonances [10] and other new processes beyond the standard model.

The paper is organized as follows. Sections 2 and 3 briefly describe the CMS detector, the online selections, the data, and Monte Carlo (MC) simulations used in this analysis. The electron reconstruction algorithms, together with the performance of the electron-momentum calibration and resolution, are detailed in Section 4. The different steps in electron selection, namely the identification and the isolation techniques, are described in Section 5. Measurements of reconstruction and selection efficiencies and misidentification probabilities are presented in Section 6, and results are summarized in Section 7.

2 CMS detector

The central feature of the CMS apparatus is a superconducting solenoid of 6 m internal diameter, providing a magnetic field of 3.8 T. The field volume contains a silicon pixel and strip tracker, a lead tungstate crystal ECAL, and a brass and scintillator hadron calorimeter (HCAL), each one composed of a barrel and two endcap sections. Muons are measured in gas ionization detectors embedded in the steel flux return yoke outside of the solenoid. Extensive forward calorimetry complements the coverage provided by the barrel and endcap detectors. A more detailed description of the CMS detector together with a definition of the coordinate system and relevant kinematic variables can be found in Ref. [11]. In this section, the origin of the coordinate system is at the geometrical centre of the detector, however, in all later sections, unless otherwise specified, the origin is defined to be the reconstructed interaction point (collision vertex).

The tracker and the ECAL, being the main detectors involved in the reconstruction and identification of electrons, are described in greater detail in the following paragraphs. The HCAL, which is used at different steps of electron reconstruction and selection, is also described below.

The CMS tracker is a cylindric detector 5.5 m long and 2.5 m in diameter, equipped with silicon that provides a total surface of 200 m^2 for an active detection region of $|\eta| \leq 2.5$ (the acceptance). The inner part is based on silicon pixels and the outer part on silicon strip detectors. The pixel tracker (66 million channels) consists of 3 central layers covering a radial distance r from 4.4 cm up to 10.2 cm, complemented by two forward endcap disks covering $6 \leq r \leq 15$ cm on each side. With this geometry, a deposition of hits in at least 3 layers or disks per track for almost the entire acceptance is ensured. The strip detector (9.3 million channels) consists of 10 central layers, complemented by 12 disks in each endcap. The central layers cover radial distances $r \leq 108$ cm and $|z| \leq 109$ cm. The disks cover up to $|z| \leq 280$ cm and $r \leq 113$ cm. Since the tracker extends to $|\eta| = 2.5$, precise detection of electrons is only possible up to this pseudorapidity, despite the larger coverage of the ECAL. In this paper the acceptance of electrons is restricted to $|\eta| \leq 2.5$, corresponding to the region where electron tracks can be reconstructed in the tracker.

A consequence of the presence of the silicon tracker is a significant amount of material in front of the ECAL, mainly due to the mechanical structure, the services, and the cooling system. Figure 2 shows the thickness of the tracker as a function of η in the $|\eta| \leq 2.5$ acceptance region, presented in terms of radiation lengths X_0 [5]. It rises from $\approx$0.4 X_0 near $|\eta| \approx 0$, to $\approx$2.0 X_0 near $|\eta| \approx 1.4$, and decreases to $\approx$1.4 X_0 near $|\eta| \approx 2.5$. This material, traversed by electrons before reaching the ECAL, induces a potential loss of electron energy via bremsstrahlung. The emitted photons can also convert to e^+e^- pairs, and the produced electrons and positrons can radiate photons through bremsstrahlung, leading to the early development of an electromagnetic shower in the tracker.

The ECAL is a homogeneous and hermetic calorimeter made of $PbWO_4$ scintillating crystals. It is composed of a central barrel covering the pseudorapidity region $|\eta| \leq 1.479$ with the internal surface located at $r = 129$ cm, and complemented by two endcaps covering $1.479 \leq |\eta| \leq 3.0$ that are located at $z = \pm 315.4$ cm. The large density (8.28 g/cm^3), the small radiation length (0.89 cm), and the small Molière radius (2.3 cm) of the $PbWO_4$ crystals result in a compact calorimeter with excellent separation of close clusters. A preshower detector consisting of two planes of silicon sensors interleaved with a total of 3 X_0 of lead is located in front of the endcaps, and covers $1.653 \leq |\eta| \leq 2.6$.

The ECAL barrel is made of 61 200 trapezoidal crystals with front-face transverse sections of

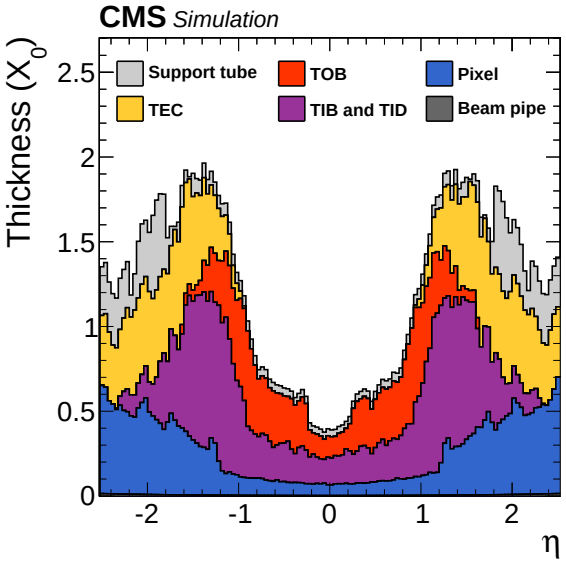

Figure 2: Total thickness of tracker material traversed by a particle produced at the centre of the detector expressed in units of X_0, as a function of particle pseudorapidity η in the $|\eta| \leq 2.5$ acceptance region. The contribution to the total material of each of the subsystems that comprise the CMS tracker is given separately for the pixel tracker, strip tracker consisting of the tracker endcap (TEC), the tracker outer barrel (TOB), the tracker inner barrel (TIB), and the tracker inner disks (TID), together with contributions from the beam pipe and the support tube that surrounds the tracker [5].

$22 \times 22\,\text{mm}^2$, giving a granularity of 0.0174 in η and 0.0174 rad in ϕ, and a length of 230 mm ($25.8\,X_0$). The crystals are installed using a quasi-projective geometry, with each one tilted by an angle of 3° relative to the projective axis that passes through the centre of CMS, to minimize electron and photon passage through uninstrumented regions. The crystals are organized in 36 supermodules, 18 on each side of $\eta = 0$. Each supermodule contains 1 700 crystals, covers 20 degrees in ϕ, and is made of four modules along η. This structure has a few thin uninstrumented regions between the modules at $|\eta| = 0$, 0.435, 0.783, 1.131, and 1.479 for the end of the barrel and the transition to the endcaps, and at every 20° between supermodules in ϕ.

The ECAL endcaps consist of a total of 14 648 trapezoidal crystals with front-face transverse sections of $28.62 \times 28.62\,\text{mm}^2$, and lengths of 220 mm ($24.7\,X_0$). The crystals are grouped in 5×5 arrays. Each endcap is separated into two half-disks. The crystals are installed within a quasi-projective geometry, with their main axes pointing 1 300 mm in z beyond the centre of CMS (-1 300 mm for the endcap at $z > 0$), resulting in tilts of 2 to 8° relative to the projective axis that passes through the centre of CMS.

The HCAL is a sampling calorimeter, with brass as the passive material, and plastic scintillator tiles serving as active material, providing coverage for $|\eta| < 2.9$. The calorimeter cells are grouped in projective towers of granularity 0.087 in η and 0.087 rad in ϕ in the barrel, and 0.17 in η and 0.17 rad in ϕ in the endcaps, the exact granularity depending on $|\eta|$. A more forward steel and quartz-fiber hadron calorimeter extends the coverage up to $|\eta| < 5.2$.

3 Data and simulation

The data sample corresponds to an integrated luminosity of $19.7\,\text{fb}^{-1}$ [12], collected at $\sqrt{s} = 8\,\text{TeV}$. The results take advantage of the final calibration and alignment conditions of the CMS

detector, obtained using the procedures described in Refs. [4, 13].

The first level (L1) of the CMS trigger system, composed of specially designed hardware processors, uses information from the calorimeters and muon detectors to select events of interest in 3.6 μs. The high-level trigger (HLT) processor farm decreases the event rate from about 100 kHz (L1 rate) to about 400 Hz for data storage [11].

The electron and photon candidates at L1 are based on ECAL trigger towers defined by arrays of 5×5 crystals in the barrel and similar but more complex arrays of crystals in the endcaps. The central trigger tower with largest transverse energy $E_{\mathrm{T}} = E \sin(\theta)$, together with its next-highest adjacent E_{T} tower form a L1 candidate. Requirements are set on the energy distribution among the central and neighbouring towers, on the amount of energy in the HCAL downstream the central tower, and on the E_{T} of the electron candidate. The HLT electron candidates are constructed through associations of energy in ECAL crystals grouped into clusters (as discussed in Section 4.1) around the corresponding L1 electron candidate and a reconstructed track with direction compatible with the location of ECAL clusters. Their selection relies on identification and isolation criteria, together with minimal thresholds on E_{T}. The identification criteria are based on the transverse profile of the cluster of energy in the ECAL, the amount of energy in the HCAL downstream the ECAL cluster, and the degree of association between the track and the ECAL cluster. The isolation criterion makes use of the energies that surround the HLT electron candidate in the tracker, in the ECAL, and in the HCAL.

The electron triggers, corresponding to the first selection step of most analyses using electrons, require the presence of at least one, two or three electron candidates at L1 and HLT. Table 1 shows the lowest unprescaled L1 and HLT E_{T} thresholds.

Table 1: Lowest, unprescaled E_{T} threshold values in GeV used for the L1 and HLT single-, double- and triple-electron triggers.

	Single	Double	Triple
L1	20	13, 7	12, 7, 5
HLT	27	17, 8	15, 8, 5

The performance of electron reconstruction and selection is checked with events selected by the double-electron triggers. These are mainly used to collect electrons from Z boson decays, but also from low-mass resonances, usually at a smaller rate. To study efficiencies, two additional dedicated double-electron triggers are introduced to maximize the number of $\mathrm{Z} \to \mathrm{e}^+\mathrm{e}^-$ events collected without biasing the efficiency of one of the electrons. Both triggers require a tightly selected HLT electron candidate, and either a second looser HLT electron or a cluster in the ECAL, that together have an invariant mass above 50 GeV. Finally, studies of background distributions and misidentification probabilities are performed using events with $\mathrm{Z} \to \mathrm{e}^+\mathrm{e}^-$ or $\mathrm{Z} \to \mu^+\mu^-$ decays that contain a single additional jet misidentified as an electron, the latter also using triggers with two relatively high-p_{T} muons.

Several simulated samples are exploited to optimize reconstruction and selection algorithms, to evaluate efficiencies, and to compute systematic uncertainties. The reconstruction algorithms are tuned mostly on simulated events with two back-to-back electrons with uniform distributions in η and p_{T}, with $1 < p_{\mathrm{T}} < 100$ GeV. Simulated Drell–Yan (DY) events, corresponding to generic quark + antiquark $\to \mathrm{Z}/\gamma^* \to \mathrm{e}^+\mathrm{e}^-$ production, are used to study various reconstruction and selection efficiencies. Results from the MADGRAPH 5.1 [14] and POWHEG [15–17] generators are compared to evaluate systematic uncertainties. These programs are interfaced to PYTHIA 6.426 [18] for showering of partons and for jet fragmentation. The PYTHIA tune Z2* [19] is used to generate the underlying event.

Pileup signals caused by additional proton-proton interactions in the same time frame of the event of interest are added to the simulation. There are on average approximately 15 reconstructed interaction vertices for each recorded interaction, corresponding to about 21 concurrent interactions per beam crossing.

The generated events are processed through a full GEANT4-based [20, 21] detector simulation and reconstructed with the same algorithms as used for the data. A realistic description of the detector conditions (tracker alignment, ECAL calibration and alignment, electronic noise) is implemented in the simulation. In addition, for some specific tasks requiring a more precise understanding of the detector, a run-dependent version of the simulation is used to match the evolution of the detector response with time observed in data. This run-dependent simulation includes the evolution of the transparency of the crystals and of the noise in the ECAL, and accounts in each event for the effect of energy deposition from interactions in a significantly increased time window relative to the one containing the event of interest.

4 Electron reconstruction

Electrons are reconstructed by associating a track reconstructed in the silicon detector with a cluster of energy in the ECAL. A mixture of a stand-alone approach [3] and the complementary global "particle-flow" (PF) algorithm [22, 23] is used to maximize the performance.

This section specifies the algorithms used for clustering the energy deposited in the ECAL, building the electron track, and associating the two inputs to estimate the electron properties. Most of these algorithms have been optimized using simulation, and adjusted during data taking periods. A large part of the section is dedicated to the estimation of electron momentum, the chain of momentum calibration, and the performance of the momentum scale and resolution.

4.1 Clustering of electron energy in the ECAL

The electron energy usually spreads out over several crystals of the ECAL. This spread can be quite small when electrons lose little energy via bremsstrahlung before reaching ECAL. For example, electrons of 120 GeV in a test beam that impinge directly on the centre of a crystal deposit about 97% of the energy in a 5×5 crystal array [24]. For an electron produced within CMS, the effect induced by radiation of photons can be large: on average, 33% of the electron energy is radiated before it reaches the ECAL where the intervening material is minimal ($\eta \approx 0$), and about 86% of its energy is radiated where the intervening material is the largest ($|\eta| \approx 1.4$).

To measure the initial energy of the electron accurately, it is essential to collect the energy of the radiated photons that mainly spreads along the ϕ direction because of the bending of the electron trajectory in the magnetic field. The spread in the η direction is usually negligible, except for very low p_T ($p_T \lesssim 5$ GeV). Two clustering algorithms, the "hybrid" algorithm in the barrel, and the "multi-5×5" in the endcaps, are used for this purpose and are described in the following paragraphs. For the clustering step, the η and ϕ directions and E_T are defined relative to the centre of CMS.

The hybrid algorithm exploits the geometry of the ECAL barrel (EB) and properties of the shower shape, collecting the energy in a small window in η and an extended window in ϕ [2]. The starting point is a seed crystal, defined as the one containing most of the energy deposited in any considered region, that has a minimum E_T of $E_{T,\,seed} > E_{T,\,seed}^{min}$. Arrays of 5×1 crystals in $\eta \times \phi$ are added around the seed crystal, in a range of N_{steps} crystals in both directions of

ϕ, if their energies exceed a minimum threshold of $E^{\text{min}}_{\text{array}}$. The contiguous arrays are grouped into clusters, with each distinct cluster required to have a seed array with energy greater than a threshold of $E^{\text{min}}_{\text{seed-array}}$ in order to be collected in the final global cluster, called the supercluster (SC). These threshold values are summarized in Table 2. They were originally tuned to provide best ECAL-energy resolution for electrons with $p_{\text{T}} \approx 15\,\text{GeV}$, but eventually minor adjustments were made to provide the current performance over a wider range of p_{T} values.

The multi-5×5 algorithm is used in the ECAL endcaps (EE), where crystals are not arranged in an $\eta \times \phi$ geometry. It starts with the seed crystals, the ones with local maximal energy relative to their four direct neighbours, which must fulfill an E_{T} requirement of $E_{\text{T, seed}} > E^{\text{min}}_{\text{T, EEseed}}$. Around these seeds and beginning with the largest E_{T}, the energy is collected in clusters of 5×5 crystals, that can partly overlap. These clusters are then grouped into an SC if their total E_{T} satisfies $E_{\text{T, cluster}} > E^{\text{min}}_{\text{T, cluster}}$, within a range in η of $\pm\eta^{\text{range}}$, and a range in ϕ of $\pm\phi^{\text{range}}$ around each seed crystal. These threshold values are summarized in Table 2. The energy-weighted positions of all clusters belonging to an SC are then extrapolated to the planes of the preshower, with the most energetic cluster used as reference point. The maximum distance in ϕ between the clusters and their reference point are used to define the preshower clustering range along ϕ, which is then extended by $\pm 0.15\,\text{rad}$. The range along η is set to 0.15 in both directions. The preshower energies within these ranges around the reference point are then added to the SC energy.

Table 2: Threshold values of parameters used in the hybrid superclustering algorithm in the barrel, and in the multi-5×5 superclustering algorithm in the endcaps.

Barrel		Endcaps	
Parameter	Value	Parameter	Value
$E^{\text{min}}_{\text{T, seed}}$	1 GeV	$E^{\text{min}}_{\text{T, EEseed}}$	0.18 GeV
$E^{\text{min}}_{\text{seed-array}}$	0.35 GeV	$E^{\text{min}}_{\text{T, cluster}}$	1 GeV
$E^{\text{min}}_{\text{array}}$	0.1 GeV	η^{range}	0.07
N_{steps}	17 (≈0.3 rad)	ϕ^{range}	0.3 rad

The SC energy corresponds to the sum of the energies of all its clusters. The SC position is calculated as the energy-weighted mean of the cluster positions. Because of the non-projective geometry of the crystals and the lateral shower shape, a simple energy-weighted mean of the crystal positions biases the estimated position of each cluster towards the core of the shower. A better position estimate is obtained by taking a weighted mean, calculated using the logarithm of the crystal energy, and applying a correction based on the depth of the shower [2].

Figure 3 illustrates the effect of superclustering on the recovery of energy from simulated $Z \to e^+e^-$ events, comparing the energy reconstructed within the SC to the one reconstructed using a simple matrix of 5×5 crystals around the most energetic crystal in a) the barrel and b) the endcaps. The tails at small values of the reconstructed energy E over the generated one (E_{gen}) are seen to be significantly reduced through the superclustering.

In addition, as part of the PF-reconstruction algorithm, another clustering algorithm is introduced that aims at reconstructing the particle showers individually. The PF clusters are reconstructed by aggregating around a seed all contiguous crystals with energies of two standard deviations (σ) above the electronic noise observed at the beginning of the data-taking run, with $E_{\text{seed}} > 230\,\text{MeV}$ in the barrel, and $E_{\text{seed}} > 600\,\text{MeV}$ or $E_{\text{T, seed}} > 150\,\text{MeV}$ in the endcaps. An important difference relative to the stand-alone approach is that it is possible to share the energy of one crystal among two or more clusters. Such clusters are used in different steps of electron reconstruction, and are hereafter referred to as PF clusters.

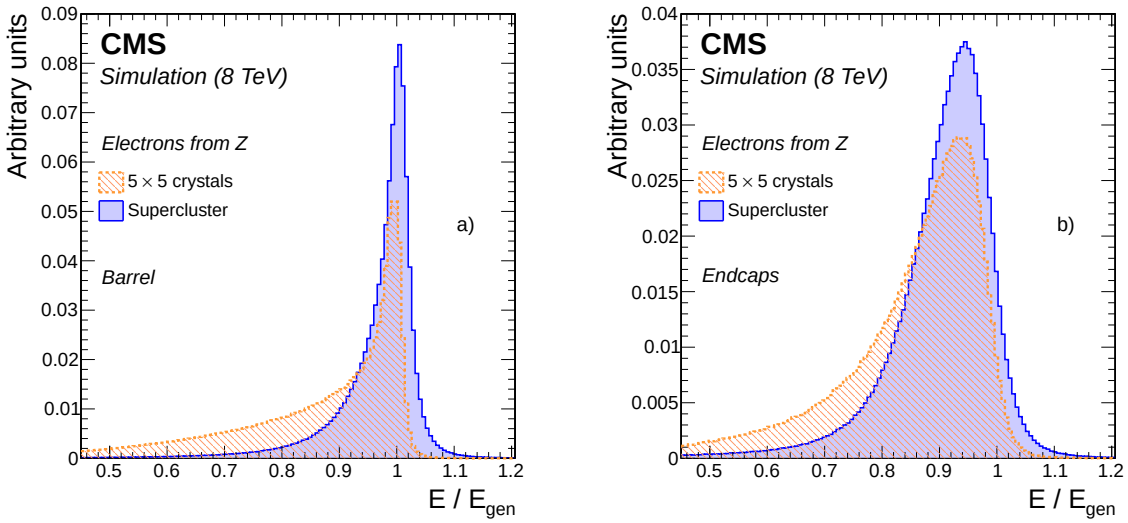

Figure 3: Comparison of the distributions of the ratio of reconstructed over generated energy for simulated electrons from Z boson decays in a) the barrel, and b) the endcaps, for energies reconstructed using superclustering (solid histogram) and a matrix of 5×5 crystals (dashed histogram). No energy correction is applied to any of the distributions.

4.2 Electron track reconstruction

Electron tracks can be reconstructed in the full tracker using the standard Kalman filter (KF) track reconstruction procedure used for all charged particles [5]. However, the large radiative losses for electrons in the tracker material compromise this procedure and lead in general to a reduced hit-collection efficiency (hits are lost when the change in curvature is large because of bremsstrahlung), as well as to a poor estimation of track parameters. For these reasons, a dedicated tracking procedure is used for electrons. As this procedure can be very time consuming, it has to be initiated from seeds that are likely to correspond to initial electron trajectories. The key point for reconstruction is to collect the hits efficiently, while preserving an optimal estimation of track parameters over the large range of energy fractions lost through bremsstrahlung.

4.2.1 Seeding

The first step in electron track reconstruction, also called seeding, consists of finding and selecting the two or three first hits in the tracker from which the track can be initiated. The seeding is of primary importance since its performance greatly affects the reconstruction efficiency. Two complementary algorithms are used and their results combined. The ECAL-based seeding starts from the SC energy and position, used to estimate the electron trajectory in the first layers of the tracker, and selects electron seeds from all the reconstructed seeds. The tracker-based seeding relies on tracks that are reconstructed using the general algorithm for charged particles, extrapolated towards the ECAL and matched to an SC. These algorithms were first commissioned with data taken in 2010, using electrons from W boson decays. The distributions in data were found to agree with expectations, even at low p_{T}, and tuning of the parameters obtained from simulation has been left essentially unchanged.

In the ECAL-based seeding, the SC energy and position are used to extrapolate the electron trajectory towards the collision vertex, relying on the fact that the energy-weighted average position of the clusters is on the helix corresponding to the initial electron energy, propagated through the magnetic field without emission of radiation. The back propagation of the helix

parameters through the magnetic field from the SC is performed for both positive and negative charge hypotheses. The intersections of helices with the innermost layers or disks predict the seeding hits. The SC are selected to limit the number of misidentified seeds using an E_T requirement of $E_T^{SC} > 4\,GeV$, together with a hadronic veto selection of $H/E_{SC} < 0.15$, with E_{SC} being the energy of the SC, and H the sum of the HCAL tower energies within a cone of $\Delta R = \sqrt{(\Delta\eta)^2 + (\Delta\phi)^2} = 0.15$ around the electron direction. This procedure reduces computing time.

On the other hand, tracker seeds are formed by combining pairs or triplets of hits with the vertices obtained from pixel tracks. Combinations of first and second hits from tracker seeds are located in the barrel pixel layers (BPix), the forward pixel disks (FPix), and in the TEC to improve the coverage in the forward region. Only a subset of the seeds leads eventually to tracks.

For each SC, a seed selection is performed by comparing hits of each tracker seed and the SC-predicted hits within windows in ϕ and z (or in transverse distance r in the forward regions where hits are only in the disks). The windows for the first and second hits are optimized using simulation to maximize the efficiency, while reducing the number of misidentified candidates to a level that can be handled within the CPU time available for electron track reconstruction. The overall efficiency of the ECAL-based seeding is ≈92% for simulated electrons from Z boson decay.

The windows for the first hit are wide, and adapted to the uncertainty in the measurement of ϕ_{SC}, and the spread of the beam spot in z (σ_z, changing with beam conditions, and typically about 5 cm in 2012). The first ϕ window is chosen to depend on E_T^{SC}, to reduce the misidentified candidates, and asymmetrical, to take into account the uncertainty on the collected energy of the SC. When the first hit of a tracker seed is matched, the information is used to refine the parameters of the helix, and to search for a second-hit compatibility with more restricted windows. A seed is selected if its first two hits are matched with the predictions from the SC.

For electrons with $5 < E_T^{SC} < 35\,GeV$, the window size in ϕ ($\delta\phi$) is a function of $1/E_T^{SC}$. The point given at 10 GeV represents the median of the dependence on E_T^{SC}. Tables 3 and 4 give the values of the first and second window acceptance parameters.

Table 3: Values of the δz, δr and $\delta\phi$ parameters used for the first window of seed selection, for three ranges of E_T^{SC}, with σ_z being the standard deviation of the beam spot along the z axis. For electron candidates with negative charge, the same $\delta\phi$ window is used, but with opposite signs.

E_T^{SC} (GeV)	δz (BPix)	δr (FPix or TEC)	$\delta\phi$ (rad) (positive charge)
≤5	$\pm 5\sigma_z$	$\pm 5\sigma_z$	$[-0.075; 0.155]$
10	$\pm 5\sigma_z$	$\pm 5\sigma_z$	$[-0.046; 0.096]$
≥35	$\pm 5\sigma_z$	$\pm 5\sigma_z$	$[-0.026; 0.054]$

Table 4: Values of the δz, δr and $\delta\phi$ parameters used in different regions of the tracker for the second window of seed selection.

δz (cm) (BPix)	δr (cm) (FPix)	δr (cm) (TEC)	$\delta\phi$ (rad) (BPix)	$\delta\phi$ (rad) (FPix or TEC)
±0.09	±0.15	±0.2	±0.004	±0.006

Figure 4 a) and b) show respectively the differences Δz_2 and $\Delta\phi_2$ between the measured and predicted positions in z (in the barrel pixels, BPix), and in ϕ (in all the tracker subdetectors),

for the second window of each electron track seed, in $Z \to e^+e^-$ events in data and in simulation. The distributions in data are slightly wider than in simulation, with the effect more pronounced in $\Delta\phi_2$, which is related directly to the difference in energy resolution between data and simulation.

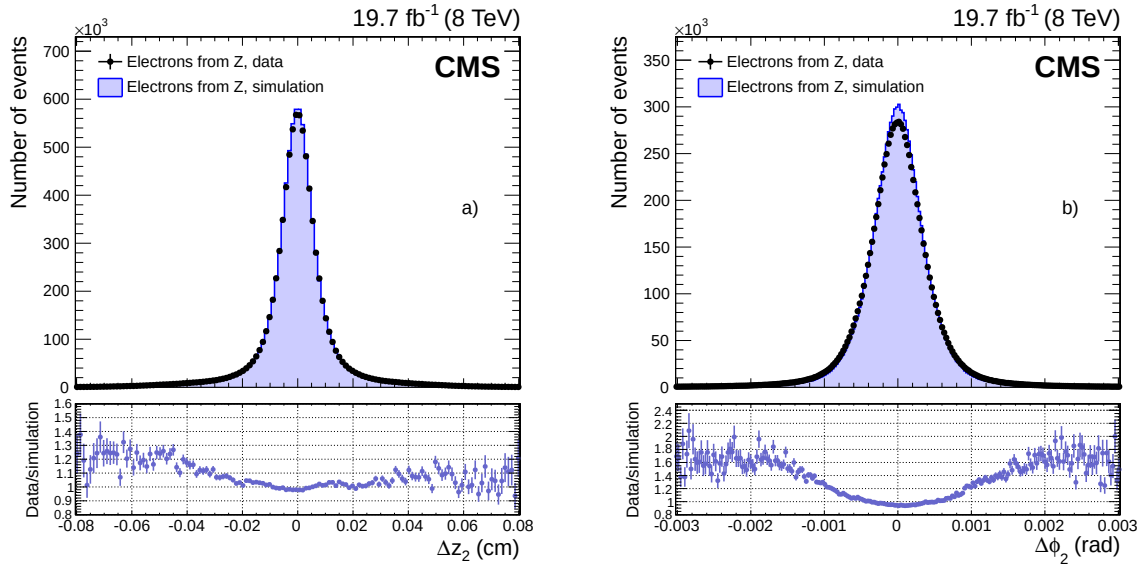

Figure 4: Distributions of the difference between predicted and measured values of the z_2 and ϕ_2 variables for hits in the second window of the ECAL-based seeding, for electrons from $Z \to e^+e^-$ decays in data (dots) and simulation (histograms): a) Δz_2 (barrel pixel), and b) $\Delta\phi_2$ (all tracker subdetectors). The data-to-simulation ratios are shown below the main panels.

Tracker-based seeding is developed as part of the PF-reconstruction algorithm, and complements the seeding efficiency, especially for low-p_T or non-isolated electrons, as well as for electrons in the barrel-endcap transition region.

The algorithm starts with tracks reconstructed with the KF algorithm. The electron trajectory can be reconstructed accurately using the KF approach when bremsstrahlung is negligible. In this case, the KF algorithm collects hits up to the ECAL, the KF track is well matched to the closest PF cluster, and its momentum is measured with good precision. As a first step of the seeding algorithm, each KF track, with direction compatible with the position of the closest PF cluster that fulfills the matching-momentum criterion of $r_{\text{th}} < E/p < 3$, has its seed selected for electron track reconstruction. The cutoff r_{th} is set to 0.65 for electrons with $2 < p_T < 6\,\text{GeV}$, and to 0.75 for electrons with $p_T \geq 6\,\text{GeV}$.

For tracks that fail the above condition, indicating potential presence of significant bremsstrahlung, a second selection is attempted. As the KF algorithm cannot follow the change of curvature of the electron trajectory because of the bremsstrahlung, it either stops collecting hits, or keeps collecting them, but with a bad quality identified through a large value of the χ^2_{KF}. The KF tracks with a small number of hits or a large χ^2_{KF} are therefore refitted using a dedicated Gaussian sum filter (GSF) [25], as described in Section 4.2.2.

The number of hits and the quality of the KF track χ^2_{KF}, the quality of the GSF track χ^2_{GSF}, and the geometrical and energy matching of the ECAL and tracker information are used in a multivariate (MVA) analysis [26] to select the tracker seed as an electron seed.

The electron seeds found using the two algorithms are combined, and the overall efficiency of the seeding is predicted >95% for simulated electrons from Z boson decay.

4.2.2 Tracking

The selected electron seeds are used to initiate electron-track building, which is followed by track fitting. The track building is based on the combinatorial KF method, which for each electron seed proceeds iteratively from the track parameters provided in each layer, including one-by-one the information from each successive layer [5]. The electron energy loss is modelled through a Bethe–Heitler function. To follow the electron trajectory in case of bremsstrahlung and to maintain good efficiency, the compatibility between the predicted and the found hits in each layer is chosen not to be too restrictive. When several hits are found compatible with those predicted in a layer, then several trajectory candidates are created and developed, with a limit of five candidate trajectories for each layer of the tracker. At most, one missing hit is allowed for an accepted trajectory candidate, and, to avoid including hits from converted bremsstrahlung photons in the reconstruction of primary electron tracks, an increased χ^2 penalty is applied to trajectory candidates with one missing hit. Figure 5 shows the number of hits collected using this procedure for electrons from a Z boson sample in data and in simulation, compared with the KF procedure used for all the other charged particles in the barrel and in the endcaps. The Z boson selection is the same as the one described in detail in Section 5. The structure in the figure reflects the geometry of the tracker. This comparison shows that shorter electrons tracks are obtained using the standard KF than using the dedicated electron building. The number of hits for the KF procedure is set to zero when there is no KF track associated with the electron. While the general behaviour is well reproduced, disagreement is observed between data and simulation due to an imperfect description of the active tracker sensors in the simulation.

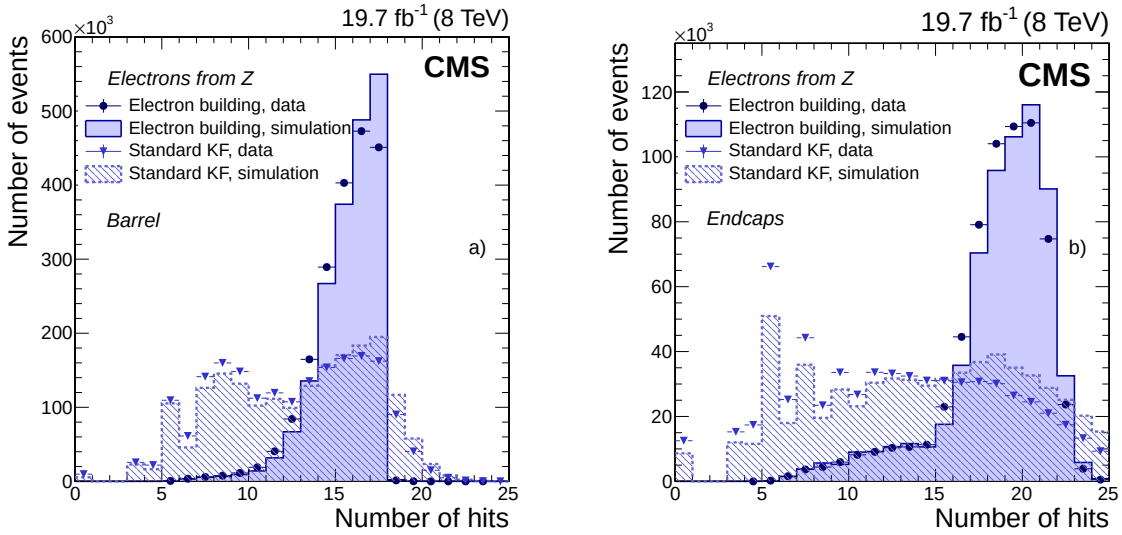

Figure 5: Comparison of the number of hits collected with the dedicated electron building and KF procedures in data (symbols) and in simulation (histograms), for electrons obtained using a $Z \to e^+e^-$ selection, a) in the barrel, and b) in the endcaps.

Once the hits are collected, a GSF fit is performed to estimate the track parameters. The energy loss in each layer is approximated by a mixture of Gaussian distributions. A weight is attributed to each Gaussian distribution that describes the associated probability. Two estimates of track properties are usually exploited at each measurement point that correspond either to the weighted mean of all the components, or to their most probable value (mode). The former provides an unbiased average, while the latter peaks at the generated value and has a smaller standard deviation for the core of the distribution [3]. This is shown in Fig. 6, where the ratio p_T/p_T^{gen} is compared for the two estimates, for simulated electrons from Z boson decays. For

these reasons, the mode estimate is chosen to characterize all the parameters of electron tracks.

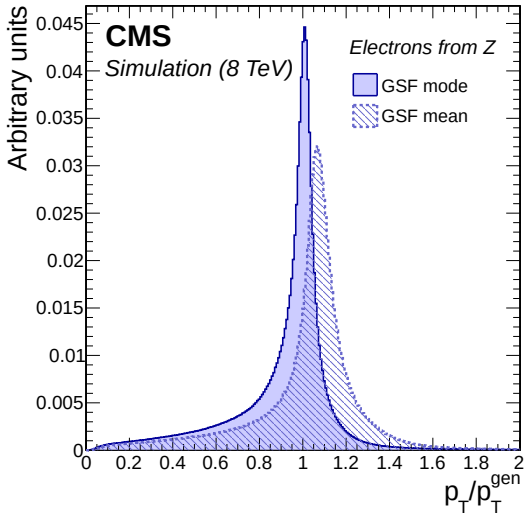

Figure 6: Distribution of the ratio of reconstructed over generated electron p_{T} in simulated $\mathrm{Z} \to \mathrm{e}^{+}\mathrm{e}^{-}$ events, reconstructed through the most probable value of the GSF track components (solid histogram), and its weighted mean (dashed histogram).

This procedure of track building and fitting provides electron tracks that can be followed up to the ECAL, and thereby extract track parameters at the surface of the ECAL. The fraction of energy lost through bremsstrahlung is estimated using the momentum at the point of closest approach to the beam spot (p_{in}), and the momentum extrapolated to the surface of the ECAL from the track at the exit of the tracker (p_{out}), and is defined as $f_{\mathrm{brem}} = [p_{\mathrm{in}} - p_{\mathrm{out}}]/p_{\mathrm{in}}$. This variable is used to estimate the electron momentum, and it enters into the identification procedure. In Fig. 7, this observable is shown for $\mathrm{Z} \to \mathrm{e}^{+}\mathrm{e}^{-}$ data and simulated events, as well as for misidentified electron candidates from jets in data enriched in Z+jets, in four regions of the ECAL barrel and endcaps. Each distribution is normalized to the area of the $\mathrm{Z} \to \mathrm{e}^{+}\mathrm{e}^{-}$ data. The Z boson and background selections are those described in Section 5. When a bremsstrahlung photon is emitted prior to the first three hits in the tracker, leading to an underestimation of p_{in}, or when the amount of radiated energy is very low, the p_{out} and p_{in} have similar values, and p_{out} can be measured to be greater than p_{in}, leading thereby to negative values of f_{brem}. In the central barrel region, the amount of intervening material is small, and the bremsstrahlung fraction peaks at low values, contrary to the outer region, where the amount of material is large and leads to a sizable population of electrons emitting high fractions of their energies through bremsstrahlung. For the background, chiefly composed of hadron tracks misidentified as electrons, the bremsstrahlung fraction generally peaks at very small values.

The disagreement observed between data and simulation in the endcap region is attributed to an imperfect modelling of the material in simulation. In fact, the f_{brem} variable is a perfect tool for accessing the intervening material, and a direct comparison of the mean value of f_{brem} in data and in simulation in narrow bins of η indicates that the description of the material in certain regions is imperfect. For example, a localized region near $|\eta| \approx 0.5$ where there are complicated connections of the TOB to its wheels, and beyond $|\eta| \approx 0.8$ where there is a region of inactive material, do not have the material properly represented in the simulation [27]. The observed difference between data and simulation, relevant for updating the simulated geometry in future analyses, is taken into account in the analysis of 8 TeV data, through specific corrections applied to the electron momentum scale, resolution, and identification and reconstruction

efficiencies extracted from $Z \to e^+e^-$ events, as discussed in Sections 4.8.4 and 6.

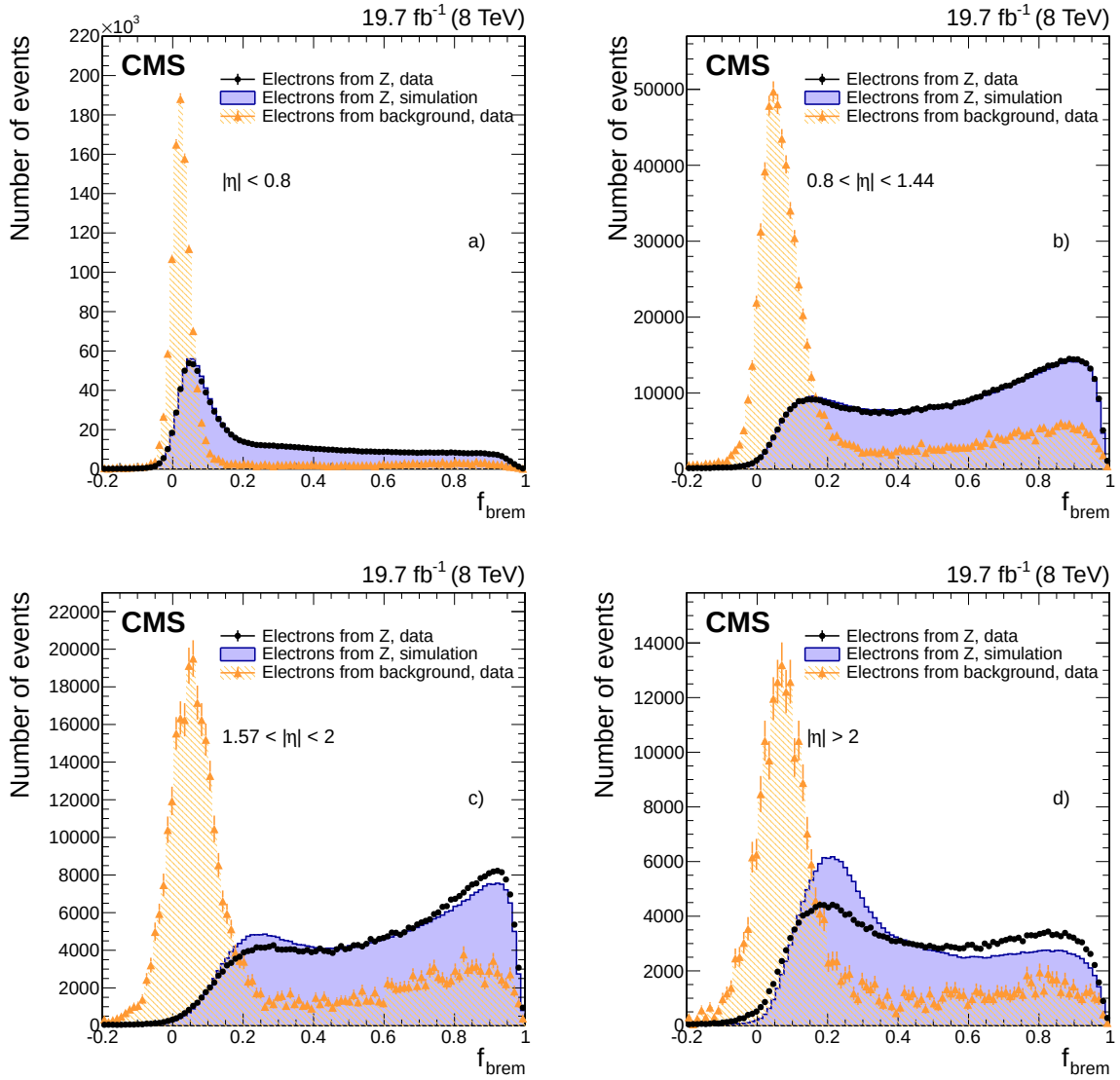

Figure 7: Distribution of f_{brem} for electrons from $Z \to e^+e^-$ data (dots) and simulated (solid histograms) events, and from background-enriched events in data (triangles), in a) the central barrel $|\eta| < 0.8$, b) outer barrel $0.8 < |\eta| < 1.44$, c) endcaps $1.57 < |\eta| < 2$, and d) endcaps $|\eta| > 2$. The distributions are normalized to the area of the $Z \to e^+e^-$ data distributions.

4.3 Electron particle-flow clustering

The PF clustering of electrons is driven by GSF tracks, and is independent of the way they are seeded. For each GSF track, several PF clusters, corresponding to the electron at the ECAL surface and the bremsstrahlung photons emitted along its trajectory, are grouped together. The PF cluster corresponding to the electron at the ECAL surface is the one matched to the track at the exit of the tracker. Since most of the material is concentrated in the layers of the tracker, for each layer a straight line is extrapolated to the ECAL, tangent to the electron track, and each matching PF cluster is added to the electron PF cluster. Most of the bremsstrahlung photons are recovered in this way, but some converted photons can be missed. For these photons, a specific procedure selects displaced KF tracks through a dedicated MVA algorithm, and kinematically

associates them with the PF clusters. In addition, for ECAL-seeded isolated electrons, any PF clusters matched geometrically with the hybrid or multi-5×5 SC are also added to the PF electron cluster.

4.4 Association between track and cluster

The electron candidates are constructed from the association of a GSF track and a cluster in the ECAL. For ECAL-seeded electrons, the ECAL cluster associated with the track is simply the one reconstructed through the hybrid or the multi-5×5 algorithm that led to the seed. For electrons seeded only through the tracker-based approach, the association is made with the electron PF cluster.

The track-cluster association criterion, just like the seeding selection, is designed to preserve highest efficiency and reduced misidentification probability, and it is therefore not very restrictive along the direction of the track curvature affected by bremsstrahlung. For ECAL-seeded electrons, this requires a geometrical matching between the GSF track and the SC, such as:

- $|\Delta\eta| = |\eta_{\mathrm{SC}} - \eta_{\mathrm{in}}^{\mathrm{extrap}}| < 0.02$, with η_{SC} being the SC energy-weighted position in η, and $\eta_{\mathrm{in}}^{\mathrm{extrap}}$ the track η extrapolated from the innermost track position and direction to the position of closest approach to the SC,
- $|\Delta\phi| = |\phi_{\mathrm{SC}} - \phi_{\mathrm{in}}^{\mathrm{extrap}}| < 0.15$, with analogous definitions for ϕ.

For tracker-seeded electrons, a global identification variable is defined using an MVA technique that combines information on track observables (kinematics, quality, and KF track), the electron PF cluster observables (shape and pattern), and the association between the two (geometric and kinematic observables). For electrons seeded only through the tracker-based approach, a weak selection is applied on this global identification variable. For electrons seeded through both approaches, a logical OR is applied on the two selections.

The overall efficiency is ≈93% for electrons from Z decay, and the reconstruction efficiency measured in data is compared to simulation in Section 6.1.

4.5 Resolving ambiguity

Bremsstrahlung photons can convert into e^+e^- pairs within the tracker and be reconstructed as electron candidates. This is particularly important for $|\eta| > 2$, where electron seeds can be used from layers of the tracker endcap that are located far from the interaction vertex and away from the bulk of the material. In such topologies, a single electron seed can often lead to several reconstructed tracks, especially when a bremsstrahlung photon carries a significant fraction of the initial electron energy, so that the hits corresponding to the converted photon are located close to the expected position of the initial track. This creates ambiguities in electron candidates, when two nearby GSF tracks share the same SC.

To resolve this problem, the following criteria are used, based on the small probability of a bremsstrahlung photon to convert in the tracker material just after its point of emission. The number of missing inner hits is obtained from the intersections between the track trajectory and the active inner layers.

- When two GSF tracks have a different number of missing inner hits, the one with the smallest number is retained.
- When the number of missing inner hits is the same, and both candidates have an ECAL-based seed, the one with E_{SC}/p closest to unity is chosen, where p is the track momentum evaluated at the interaction vertex.

- The same criterion is also applied when both candidates have the same number of missing inner hits and just tracker-based seeds.
- When the number of missing inner hits is the same, but only one candidate is just tracker-seeded, the track with an ECAL-based seed is chosen, because the tracks from tracker-based seeds have a higher chance to be contaminated by track segments from conversions.

4.6 Relative ECAL to tracker alignment with electrons

Electrons are also used to probe subtle detector effects such as the ECAL alignment relative to the tracker. The tracker was first aligned using cosmic rays before the start of LHC operations, and constantly refined using proton-proton collisions, reaching an accuracy $< 10\,\mu$m [13]. The relative alignment of the tracker to the ECAL for 2012 data is obtained using electrons from Z boson decays. Tight identification and isolation criteria are applied to both electrons with $E_{\mathrm{T}} > 30\,\mathrm{GeV}$, and the dielectron invariant mass is required to be $|m_{\mathrm{e^+e^-}} - m_{\mathrm{Z}}| < 7.5\,\mathrm{GeV}$, to ensure a high signal purity of 97%, needed for the alignment procedure. In addition, to disentangle bremsstrahlung effects from position reconstruction, only electrons with little bremsstrahlung and best energy measurement are considered. The distances $\Delta\eta$ and $\Delta\phi$, defined in Section 4.4, are compared between data and simulation, the ECAL being aligned with the tracker in the simulation. The position of each supermodule in the barrel and each half-disk in the endcaps is measured relative to the tracker by minimizing the differences between data and simulation as a function of the alignment coefficients. Residual misalignments lower than 2×10^{-3} rad in $\Delta\phi$ and 2×10^{-3} units in $\Delta\eta$, are obtained using this procedure, which is compatible with expectations from simulation.

4.7 Charge estimation

The measurement of the electron charge is affected by bremsstrahlung followed by photon conversions. In particular, when the bremsstrahlung photons convert upstream in the detector, they lead to very complex hit patterns, and the contributions from conversions can be wrongly included in the fitting of the electron track.

A natural choice for a charge estimate is the sign of the GSF track curvature, which unfortunately can be altered by the misidentification probability in presence of conversions, especially for $|\eta| > 2$, where it can reach about 10% for reconstructed electrons from Z boson decay without further selection. This is improved by combining two other charge estimates, one that is based on the associated KF track matched to a GSF track when at least one hit is shared in the innermost region, and the second one that is evaluated using the SC position, and defined as the sign of the difference in ϕ between the vector joining the beam spot to the SC position and the vector joining the beam spot and the first hit of the electron GSF track.

The electron charge is defined by the sign shared by at least two of the three estimates, and is referred to as the "majority method". The misidentification probability of this algorithm is predicted by simulation to be 1.5% for reconstructed electrons from Z boson decays without further selection, offering thereby a global improvement on the charge-misidentification probability of about a factor 2 relative to the charge given by the GSF track curvature alone. It also reduces the misidentification probability at very large $|\eta|$, where it is predicted to be <7% for such electrons. Higher purity can be obtained by requiring all three measurements to agree, termed the "selective method". This yields a misidentification probability of <0.2% in the central part of the barrel, <0.5% in the outer part of the barrel, and <1.0% in the endcaps, which can be achieved at the price of an efficiency loss that depends on p_{T}, but is typically ≈7% for

electrons from Z boson decays. The selective algorithm is used mainly in analyses where the charge estimate is crucial, for example in the study of charge asymmetry in inclusive W boson production [28], or in searches for supersymmetry using same-charge dileptons [29].

The charge misidentification probability decreases strongly when the identification selections become more restrictive, mainly because of the suppression of photon conversions. Table 5 gives the measurement in data and simulation of the charge misidentification probability that can be achieved for a tight selection of electrons (corresponding to the HLT criteria) from $Z \to e^+e^-$ decays in the barrel and in the endcaps, for the majority and the selective methods. These values are estimated by comparing the number of same-charge and opposite-charge dielectron pairs that are extracted from a fit to the dielectron invariant mass. The misidentification probability is significantly reduced relative to the one at the reconstruction level. A good agreement is found between data and simulation in both ECAL regions and for both charge-estimation methods.

Table 5: Charge misidentification probability for a tight selection of electrons from $Z \to e^+e^-$ decays in the barrel and in the endcaps, for the majority and for the selective methods used to estimate electron charge.

	Barrel		Endcaps	
Method	Simulation	Data	Simulation	Data
majority	$0.13 \pm 0.01\%$	$0.14 \pm 0.01\%$	$1.4 \pm 0.2\%$	$1.6 \pm 0.2\%$
selective	$0.017 \pm 0.002\%$	$0.020 \pm 0.002\%$	$0.21 \pm 0.02\%$	$0.23 \pm 0.02\%$

4.8 Estimation of electron momentum

The electron momentum is estimated using a combination of the tracker and ECAL measurements. As for all electron observables, it is particularly sensitive to the pattern of bremsstrahlung photons and their conversions. To achieve the best possible measurement of electron momentum, electrons are classified according to their bremsstrahlung pattern, using observables sensitive to the emission and conversion of photons emitted along the electron trajectory. The SC energy is corrected and calibrated, then the combination between the tracker and ECAL measurements is performed.

4.8.1 Classification

For most of the electrons, the bremsstrahlung fraction in the tracker f_{brem}, defined in Section 4.2.2, is complemented by the bremsstrahlung fraction in the ECAL, defined as $f_{\text{brem}}^{\text{ECAL}} = [E_{\text{SC}}^{\text{PF}} - E_{\text{ele}}^{\text{PF}}]/E_{\text{SC}}^{\text{PF}}$, where $E_{\text{SC}}^{\text{PF}}$ and $E_{\text{ele}}^{\text{PF}}$ are the SC energy and the electron-cluster energy measured with the PF algorithm, that correspond respectively to the initial and final electron energies. The number of clusters in the SC is also used in the classification process.

Electrons are classified in the following categories:

- "Golden" electrons are those with little bremsstrahlung and consequently provide the most accurate estimation of momentum. They are defined by an SC with a single cluster and $f_{\text{brem}} < 0.5$.
- "Big-brem" electrons have a large amount of bremsstrahlung radiated in a single step, either very early or very late along the electron trajectory. They are defined by an SC with a single cluster and $f_{\text{brem}} > 0.5$.
- "Showering" electrons have a large amount of bremsstrahlung radiated all along the electron trajectory, and are defined by an SC containing several clusters.

In addition, two special electron categories are defined. One is termed "crack" electrons, defined as electrons with the SC seed crystal adjacent to an η boundary between the modules of the ECAL barrel, or between the ECAL barrel and endcaps, or at the high $|\eta|$ edge of the endcaps. The second category, called "bad track", requires a calorimetric bremsstrahlung fraction that is significantly larger than the track bremsstrahlung fraction ($f_{\text{brem}}^{\text{ECAL}} - f_{\text{brem}} > 0.15$), which identifies electrons with a poorly fitted track in the innermost part of the trajectory.

Figure 8 a) shows the fraction of the electron population in the above classes, as a function of $|\eta|$ (defined relative to the centre of CMS), for data and simulated electrons from Z boson decays. Crack electrons are not shown in the plot, but complement the proportion to unity. The distributions for the golden and showering classes reflect the η distribution of the intervening material. Data and simulation agree well, except for the regions of η with known mismodelling of material, and for $|\eta| > 2$, where the number of clusters is overestimated in the simulation. The integrated proportions of electrons in the different classes for data and simulation are, respectively, 57.4% and 56.8% for showering, 25.5% and 26.3% for golden, 8.4% and 8.0% for big-brem, 4.1% and 4.1% for bad track, and 4.6% and 4.7% for crack electrons. Figure 8 b) shows the distributions in the ratio of reconstructed SC energy to the generated energy (E_{gen}) for the different classes. The SC performs differently for each class, and provides an energy estimate of limited quality for electrons with sizeable bremsstrahlung. An improved energy estimate is achieved with additional corrections, as discussed in the following section.

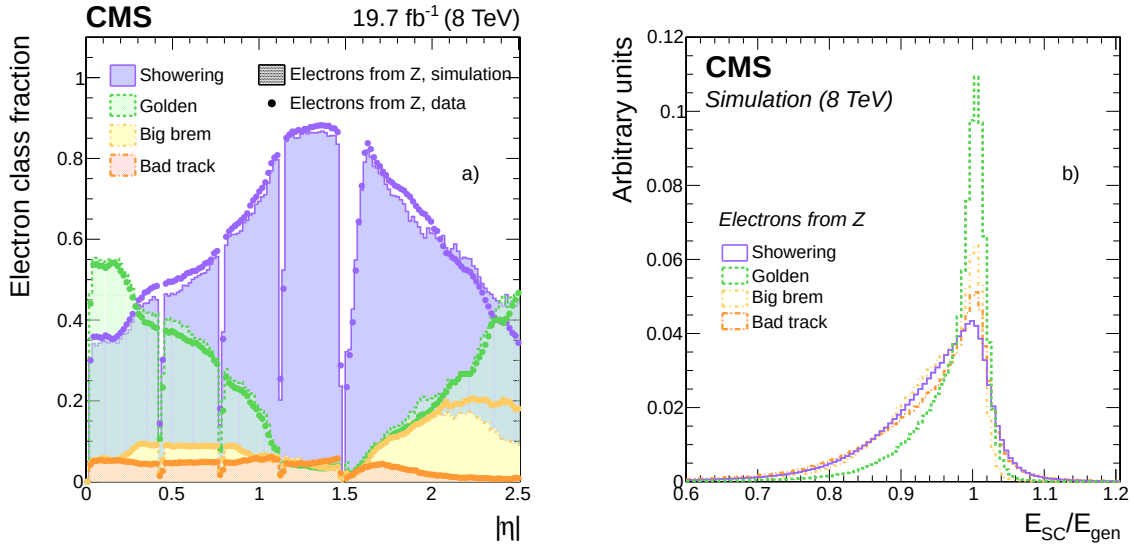

Figure 8: a) Fraction of population in different classes of electrons from Z boson decays as a function of $|\eta|$, for data (dots) and simulated (histograms) events, and b) distribution of $E_{\text{SC}}/E_{\text{gen}}$ for the different classes of simulated electrons. Crack electrons are not shown in either plot.

4.8.2 ECAL supercluster energy

Energy in individual crystals Several procedures are used to calibrate the energy response of individual crystals before the clustering step [4]. The amplitude in each crystal is reconstructed using a linear combination of the 40 MHz sampling of the pulse shape. This amplitude is then converted into an energy value using factors measured separately for the ECAL barrel, endcaps, and the preshower detector. The changes in the crystal response induced by radiation are corrected through the ECAL laser-monitoring system [30, 31], and the correction factors are checked using the reconstructed dielectron invariant mass in $Z \to e^+e^-$ events, and through

the ratio of the ECAL energy and the track momentum (E_{SC}/p) in $W \to e\nu$ events. The intercalibration factors between crystals are obtained with data using different methods, e.g. the ϕ symmetry of the energy in minimum-bias events for a given η, the reconstructed invariant mass of $\pi^0 \to \gamma\gamma$, $\eta \to \gamma\gamma$, and $Z \to e^+e^-$ events, and the E_{SC}/p ratio of electrons in $W \to e\nu$ events.

Supercluster energy correction The SC energy is obtained by summing the individual energies in all the crystals of an SC, and the preshower energies of electrons in the endcaps. At this stage, the main effects impacting the estimation of SC energy are related to energy containment:

- energy leakage in ϕ or η out of the SC,
- energy leakage into the gaps between crystals, modules, supermodules, and the transition region between barrel and endcaps,
- energy leakage into the HCAL downstream the ECAL,
- energy loss in interactions in the material before the ECAL, and
- additional energy from pileup interactions.

An MVA regression technique [32] is used to obtain the SC corrections that are needed to account for these effects. Simulated electrons with a uniform spectrum in η and p_T between 5 and 300 GeV are used to train the regression algorithm, separately for electrons in the barrel and in the endcaps. The regression target is the ratio E_{gen}/E_{SC}. The first input observables are the SC energy to be corrected, and the SC position in η and ϕ, which are related to the intervening material. The energy leakage out of the SC is assessed through the SC shape observables and its number of clusters, together with their individual respective positions, energies, and shape observables. The energy leakage in the gaps between modules, supermodules and in the transition region between the barrel and endcaps is explored through the position of the seed crystal of the SC. The position of the seed cluster relative to the seed crystal is used together with the shower-shape observables to account for energy leakage between the crystals. The ratio H/E_{SC} (defined in Section 4.2.1) is used to estimate the energy leakage into the HCAL. The effects of pileup interactions are assessed through the number of reconstructed interaction vertices and the average energy density ρ in the event (defined as the median of the energy density distribution for particles within the area of any jet in the event, reconstructed using the k_T-clustering algorithm [33, 34] with distance parameter of 0.6, $p_T^{jet} > 3$ GeV and within $|\eta| < 2.5$).

Figure 9 shows the distribution in the ratio of the corrected SC energy over the generated energy E_{SC}^{cor}/E_{gen}, obtained through the regression for two categories of simulated electrons: low-p_T electrons ($7 \leq p_T < 10$ GeV) in the central part of the barrel, and medium-p_T electrons ($30 \leq p_T < 35$ GeV) in the forward part of the endcaps. The distributions are fitted with a "double" Crystal Ball function [35]. The Crystal Ball function is defined as:

$$f_{CB}(x;\alpha,n,m_{CB},\sigma_{CB}) = N \begin{cases} A\left[B - \dfrac{x-m_{CB}}{\sigma_{CB}}\right]^{-n}, & \text{for} \quad \dfrac{x-m_{CB}}{\sigma_{CB}} \leq -\alpha \\ \exp\left(-\dfrac{(x-m_{CB})^2}{2\sigma_{CB}^2}\right), & \text{for} \quad \dfrac{x-m_{CB}}{\sigma_{CB}} > -\alpha \end{cases} \tag{1}$$

where A and B are functions of α and n, and N is a normalization factor. This function is intended to capture both the Gaussian core of the distribution (described by σ_{CB}) and non-Gaussian tails (described by the parameters n and α). The double Crystal Ball function is a

modified Crystal Ball with the σ_{CB}, n, and α parameters distinct for x values below and above the peak position at m_{CB}.

The peak position and the standard deviation of the Gaussian core of the distributions are estimated through the fitted values of m_{CB} and σ_{CB}, respectively. The "effective" standard deviation σ_{eff}, defined as half of the smallest interval around the peak position containing 68.3% of the electrons, is used to assess the resolution, while taking into account possible non-Gaussian tails. A bias of at most 1% affects the peak position, which reflects the asymmetric nature of the E_{CB}/E_{SC} distribution.

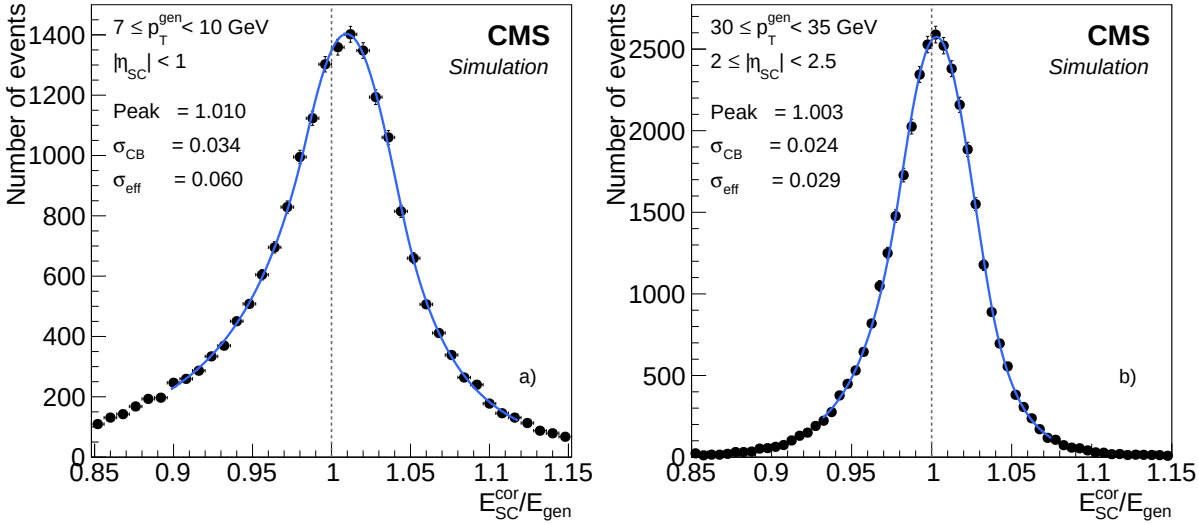

Figure 9: Example distributions of the ratio of corrected over generated supercluster energies (E_{SC}^{cor}/E_{CB}) and their (double Crystal Ball) fits, in two regions of η and p_T after implementing the regression corrections: for electrons a) with $7 \leq p_T < 10\,GeV$ and $|\eta_{SC}| < 1$, and b) with $30 \leq p_T < 35\,GeV$ and $2 \leq |\eta_{SC}| < 2.5$, η_{SC} being defined relative to the centre of CMS. Electrons are generated with uniform distributions in η and p_T.

The peak position of E_{SC}^{cor}/E_{CB} and the effective resolution for E_{SC}^{cor} are shown in Fig. 10, as a function of the number of reconstructed interaction vertices for low-p_T and medium-p_T electrons, in the barrel and in the endcaps. The bias in the peak position is independent of the number of pileup interactions. The effective resolution is in the range of 2–3% for medium-p_T electrons in the barrel, and in the range of 7–9% for low-p_T electrons in the endcaps, degrading slowly with increasing number of pileup interactions.

The use of the MVA regression technique compared to a standard parameterization of the correction for E_{SC} as a function of the electron η, category, and E_T, provides significant improvement of ≈20% in the resolution on average and up to ≈35% in the forward regions, while reducing the bias in the peak position for each electron class over the entire range of electron η and p_T.

Another MVA regression technique, based on the same input variables, is used to estimate the uncertainty in the corrected E_{SC}, separately for electrons in the barrel and in the endcaps, with the absolute difference between E_{CB} and the corrected E_{SC} being the target.

Fine-tuning of calibration and simulated resolution The SC energy corrections described above are based on simulation. Events in data are used to account for any discrepancy between data and simulation in input variables, as well as to correct for biases. The applied remnant

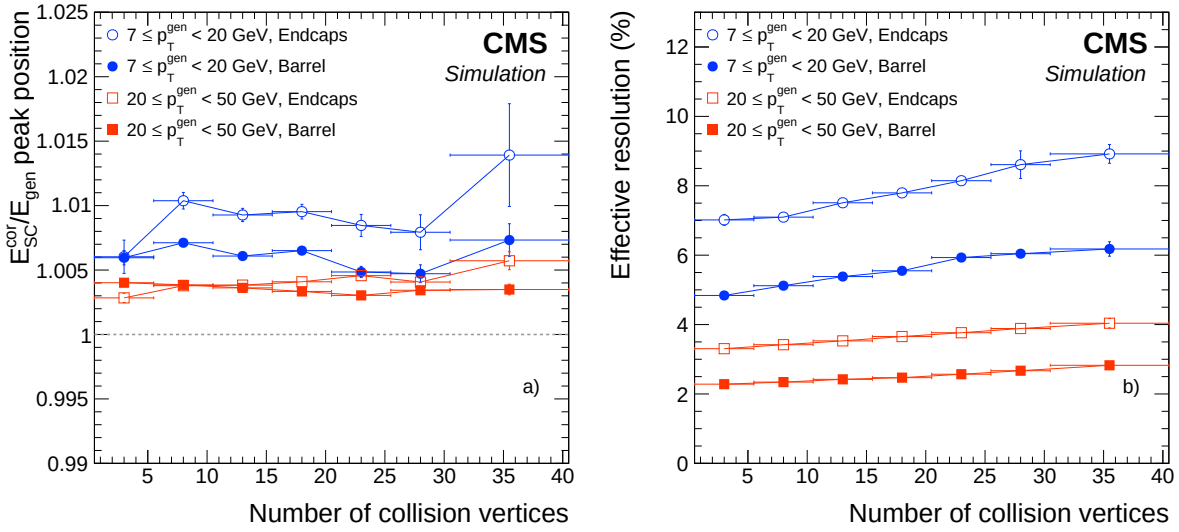

Figure 10: a) Peak position of $E_{\mathrm{SC}}^{\mathrm{cor}}/E_{\mathrm{CB}}$, and b) effective resolution of $E_{\mathrm{SC}}^{\mathrm{cor}}$, as a function of the number of reconstructed interaction vertices, for electrons in the barrel (solid symbols) and endcaps (open symbols) with $7 \leq p_{\mathrm{T}}^{\mathrm{CB}} < 20\,\mathrm{GeV}$ (circles), and $20 \leq p_{\mathrm{T}}^{\mathrm{CB}} < 50\,\mathrm{GeV}$ (squares). Electrons are generated with uniform distributions in η and p_{T}.

corrections are quite small. The energy in individual crystals is already calibrated, and simulation of showers in the ECAL is rather precise and includes the measured uncertainties in the inter-calibration between crystals. The main source of discrepancy between the energy estimate in data and in simulation is the imperfect description of the tracker material in simulation, which affects differently each category of electrons. The evolution of the transparency of the crystals and of the noise in the ECAL during data taking, if not considered through specific run-dependent simulations, leads to an additional difference between data and simulation. Another possible source of discrepancy could be the underestimation of uncertainties in the calibration of individual crystals. Finally, a difference in the ECAL geometry relative to the nominal one can cause the corrections discussed in the previous paragraph, which are obtained using simulated events with the nominal geometry, to be inappropriate for data. While it is now understood that at least one of the above effects contributes to degradation, their relative magnitudes are not as fully clear. More details on this issue can be found in Ref. [27].

The SC energy scale is corrected in the data to match that in simulation. These corrections are assessed using $\mathrm{Z} \to \mathrm{e}^{+}\mathrm{e}^{-}$ events, by comparing the dielectron invariant mass in data and in simulation for four $|\eta|$ regions and two categories of electrons, over 50 running periods, following the procedure described in Ref. [4]. The η regions are defined from the most central to the most forward values as barrel $|\eta| \leq 1$, barrel $|\eta| > 1$, endcaps $|\eta| \leq 2$, and endcaps $|\eta| > 2$. The R_9 variable, defined as the ratio of the energy reconstructed in the 3×3 crystals matrix centered on the crystal with most energy and the SC energy, is used to assess the amount of bremsstrahlung emitted by the electron. The category of electrons with a low level of bremsstrahlung is defined by $R_9 \geq 0.94$, and the one with a high level of bremsstrahlung by $R_9 < 0.94$. The Z boson mass is reconstructed from the SC energies and the opening angles measured from the tracks. The mass distribution in the range between 60 and 120 GeV is fitted using a Breit–Wigner convolved with a Crystal Ball function, both for data and simulation. The scale corrections, obtained from the difference between the peak positions measured in the data and in simulation, are applied to the data, so that the peak position of the Z boson mass agrees with that in simulation, in each category. Overall, these corrections vary between 0.9880 and

1.0076 and their uncertainties between 0.0002 and 0.0029.

The estimate of the SC energy resolution is also affected by the sources of discrepancy between data and simulation. A correction is applied in simulation to match the resolution observed in data [4]. This correction is independent of time, and evaluated for the above categories of η and R_9. The SC energy is modified by applying a factor drawn from a Gaussian distribution, centered on the corrected scale value, and with a standard deviation of $\delta\sigma^{\mathrm{e}}$, corresponding to a required additional constant term in the energy resolution. The value of $\delta\sigma^{\mathrm{e}}$ for each electron category is assessed using a maximum-likelihood fit of the data to a resolution-broadened simulated energy. This constant term in the energy resolution ranges from $(0.92 \pm 0.03)\%$ in the $|\eta| < 1$ and $R_9 \geq 0.94$ category, to $(2.90 \pm 0.03)\%$ in the $|\eta| > 2$ and $R_9 < 0.94$ category. The uncertainty in the SC energy is increased accordingly.

4.8.3 Combination of energy and momentum measurements

The electron momentum estimate p_{comb} is improved by combining the ECAL SC energy, after applying the refinements mentioned in the previous sections, with the track momentum. At energies $\lesssim$15 GeV, or for electrons near gaps in detectors, the track momentum is expected to be more precise than the ECAL SC energy. A regression technique is used to define a weight w that multiplies the track momentum in linear combination with the estimated SC energy as $p_{\mathrm{comb}} = wp + (1-w)E_{\mathrm{SC}}$.

The complementarity of the two estimates depends on the amount of emitted bremsstrahlung. The corrected SC energy and its relative uncertainty, and the track momentum and its relative uncertainty are the main input observables. The addition of the E_{SC}/p ratio and its uncertainty, together with the ratio of the two relative uncertainties, brings a higher-level information that optimizes the performance of the regression. The electron class and the position in the barrel or endcaps are also included as probes of the quality and amount of emitted bremsstrahlung.

After combining the two estimates, the bias in the electron momentum is reduced in all regions and all electron classes, except for showering electrons in the endcaps, where the bias becomes slightly worse. Figure 11 shows the effective resolution in the electron momentum (in percent), after combining the E_{SC} and p estimates, as a function of the generated p_{T}, compared to the effective resolution of the corrected SC energy, for golden electrons in the barrel and for showering electrons in the endcaps. The improvement is typically $\approx$25% for electrons with $p_{\mathrm{T}} \approx 15$ GeV in the barrel, and reaches 50% for golden electrons in the barrel at low p_{T}.

The improvement in resolution is significant for all electrons in the barrel up to energies of about 35 GeV, as can be seen in Fig. 12 a), which displays the effective resolution of the corrected SC energy, of the track momentum, and of the electron momentum after combining E_{SC} and p estimates, as a function of the generated electron energy. Figure 12 b) shows the expected reconstructed mass for a 126 GeV Higgs boson in the $\mathrm{H} \to \mathrm{ZZ}^* \to 4\mathrm{e}$ decay channel. The masses reconstructed using the corrected SC energy are compared to those using the electron momentum obtained after combining the E_{SC} and p estimates. The improvement in the effective resolution is 7%. When considering only the Gaussian core of the distribution, the improvement in the resolution is 9%.

4.8.4 Uncertainty in the momentum scale and in the resolution

The corrections to the momentum scale and resolution discussed above are only obtained from correcting the SC energy in $\mathrm{Z} \to \mathrm{e}^+\mathrm{e}^-$ events. As a consequence, they must be further corrected, first over a large range of p_{T}, especially for the $\mathrm{H} \to \mathrm{ZZ}^*$ analysis which uses electrons with p_{T} as low as 7 GeV, and second for the E_{SC} and p combination. For this purpose, $\mathrm{Z} \to \mathrm{e}^+\mathrm{e}^-$

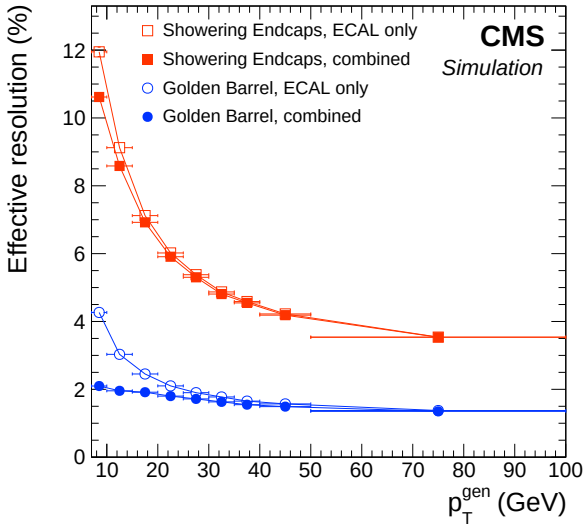

Figure 11: Effective resolution in electron momentum after combining the E_{SC} and p estimates (solid symbols), compared to that of the corrected SC energy (open symbols), as a function of the generated electron p_T. Golden electrons in the barrel (circles) and showering electrons in the endcaps (squares) are shown as examples. Electrons are generated with uniform distributions in η and p_T, and the resolution is shown after applying the resolution broadening.

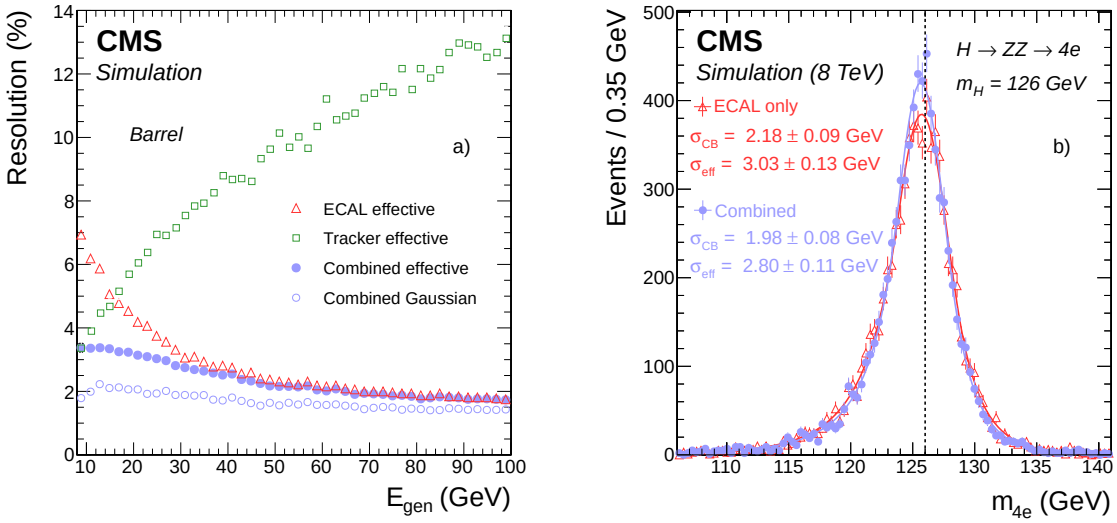

Figure 12: a) Effective resolution in electron momentum after combining E_{SC} and p estimates (solid circles), compared to those using the corrected SC energy (triangles), and the track momentum (squares), as a function of the generated energy for electrons in the barrel. Also shown is the resolution in momentum after combining E_{SC} and p estimates in terms of σ_{CB} (open circles), to illustrate the contribution of the Gaussian core of the distribution. Electrons are generated with uniform distributions in η and p_T. b) Reconstructed mass of the Higgs boson for $H(126) \to ZZ^* \to 4e$ simulated events, using either the corrected SC energy (open triangles) or the electron momentum after combining E_{SC} and p estimates (solid dots) [9].

events are used together with $J/\psi \to e^+e^-$ and $\Upsilon \to e^+e^-$ events that provide clean sources of electrons at low p_T. The reconstructed invariant masses of these resonances in data are compared with simulation to probe any remaining differences.

Figure 13 shows an example of such comparisons and their degree of agreement for two extreme categories of events: one where each electron is well measured, having a single-cluster SC (golden or big-brem class) in the barrel, and the other one where each electron has a multi-cluster SC, or is poorly-measured (showering, crack, or bad track class) in the endcaps. These two categories represent the breadth of performance in data that enters, for example, in the mass measurement of the benchmark process for Higgs boson decays to four leptons. The distributions in data and in simulation are fitted with a Breit–Wigner function convolved with a Crystal Ball function,

$$P(m_{e^+e^-}; m_Z, \Gamma_Z, \alpha, n, m_{CB}, \sigma_{CB}) = \mathrm{BW}(m_{e^+e^-}; m_Z, \Gamma_Z) \otimes f_{CB}(m_{e^+e^-}; \alpha, n, m_{CB}, \sigma_{CB}).$$

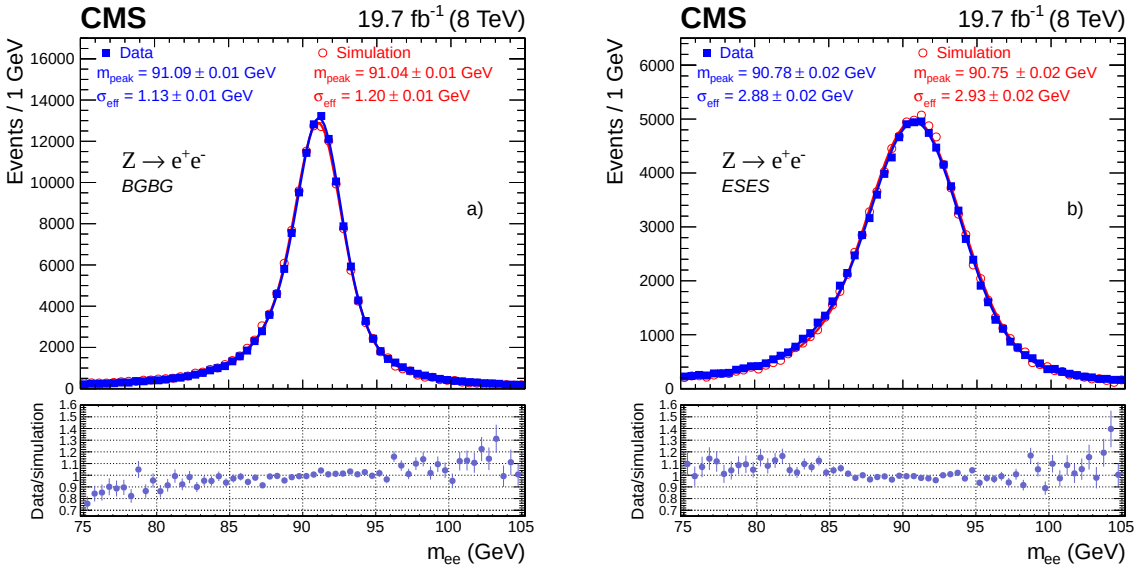

Figure 13: Dielectron invariant mass distribution from $Z \to e^+e^-$ events in data (solid squares) compared to simulation (open circles) fitted to a convolution of Crystal Ball and Gaussian functions, a) for the best-resolved event category with two well-measured single-cluster electrons in the barrel (BGBG), and b) for the worst-resolved category with two more-difficult patterns or multi-cluster electrons in the endcaps (ESES). The data-to-simulation factors are shown below the main panels.

The effective standard deviation σ_{eff}, which is indicated in the plots, is calculated as the effective standard deviation of the function f_{CB}, which therefore removes the contribution from the width of the Z boson. In both categories of events, the data and simulation show good agreement. The σ_{eff} in data for the $Z \to e^+e^-$ invariant mass are, respectively for the best and worst categories, 1.13 ± 0.01 GeV and 2.88 ± 0.02 GeV. Considering only the Gaussian cores of the distribution, the standard deviations (σ_{CB}) are 1.00 ± 0.01 GeV and 2.63 ± 0.02 GeV, for the best and the worst categories, respectively. The effective and Gaussian invariant mass resolutions of dielectron events in the data range, respectively, from 1.2 and 1.1% for the best category with two well-measured single-cluster electrons in the barrel, to 3.2 and 2.9% for the worst category with two poorly-measured or multi-cluster electrons in the endcaps. The effective and Gaussian momentum resolutions for single electrons, approximated by multiplying the dielectron mass resolution by $\sqrt{2}$, therefore range in data from 1.7 and 1.6%, to 4.5 and 4.1%, respectively.

The data-to-simulation comparisons are performed for different categories of events based on η, p_T, and class of electron, and for different instantaneous luminosities. The scale corrections are applied to data, and the resolutions are broadened in the simulated distributions, as discussed in Section 4.8.2.

For study of the momentum scale, the p_T and η categories are defined according to the p_T and η of one of the two electrons, the other electron is used to tag the Z event, it satisfies tight identification requirements (as described in Section 6), and has $p_T > 20\,\text{GeV}$. The fits are performed using signal templates (obtained from simulation as binned distributions) that are convolved with Gaussians with floating means and standard deviations. A p_T-dependence of the momentum scale of up to 0.6% in the barrel and 1.5% in the endcaps is observed and corrected in the p_T range between 7 and 70 GeV. The final performance of the momentum scale is shown in Fig. 14 a) as the relative difference between data and simulation of the $J/\psi \to e^+e^-$, $\Upsilon \to e^+e^-$, and the $Z \to e^+e^-$ mass peaks, as a function of the p_T of one electron and for several η regions of this electron, integrating over the p_T and η of the other electron. The residual scale difference between data and MC simulation is at most 0.2% in the barrel and 0.3% in the endcaps. These numbers are taken as systematic uncertainties on the momentum scale of electrons in the barrel and in the endcaps. For the study of the resolution, the p_T, η, and class categories are defined for both electrons from the Z decay. The fits are performed using a Breit–Wigner function convolved with a Crystal Ball function. The agreement between data and simulation in effective resolution is shown in Fig. 14 b), in terms of the relative difference between data and simulation for the $J/\psi \to e^+e^-$ and $Z \to e^+e^-$ events, as a function of the p_T of one electron, for different categories of electrons. Overall the relative difference in effective resolution between data and simulation is less than 10% for all the categories in this comparison.

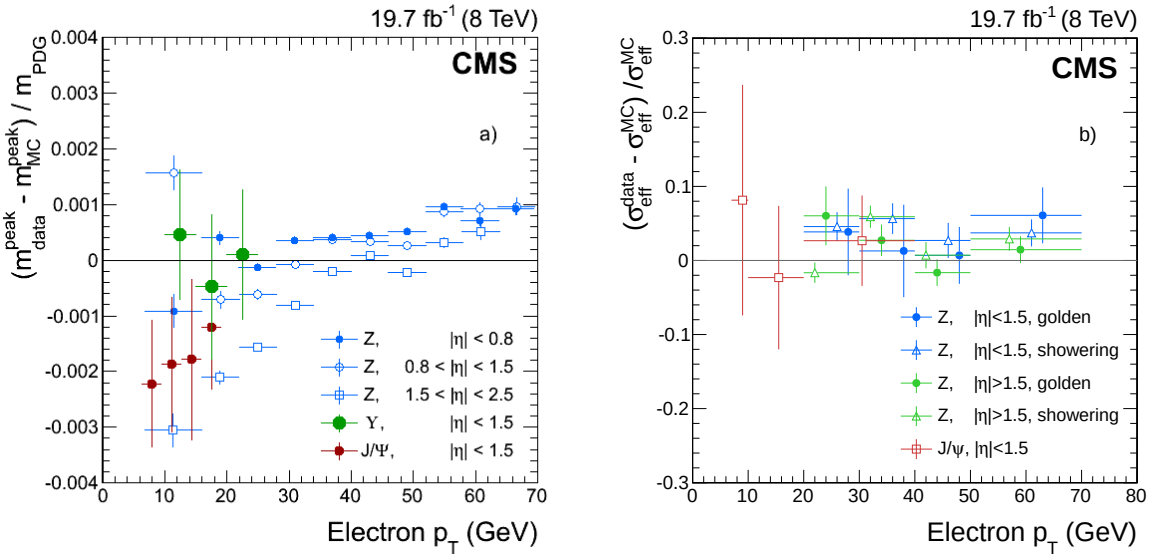

Figure 14: Relative differences between data and simulation as a function of electron p_T for different $|\eta|$ regions, a) for the momentum scale measured using $J/\psi \to e^+e^-$, $\Upsilon \to e^+e^-$, and $Z \to e^+e^-$ events [9], and b) for the effective momentum resolution of $Z \to e^+e^-$ and $J/\psi \to e^+e^-$ events for different electron categories.

4.8.5 High-energy electrons

For high-energy electrons, the E_{SC} and p combination is dominated entirely by the energy measurement in the ECAL. Because of this and for reasons of simplicity, analyses exploiting high-

energy electrons, with typical energies above 250 GeV, estimate the electron momentum using only the SC information. Moreover, energy deposition from very high-energy electrons (from about 1500 GeV in the barrel and from about 3000 GeV in the endcaps) lead to a saturation of the front-end electronics [11].

Both the calibration of high-energy electrons and the energy correction for saturated crystals are tuned with $Z \to e^+e^-$ events through a method that estimates the energy contained in the central (highest energy) crystal of a 5×5 matrix, using the 24 lower-energy surrounding crystals. The energy fraction contained in the central crystal relative to the 5×5 matrix ($E_1 / E_{5\times5}$) is parameterized as a function of the electron η, $E_{5\times5}$, as well as other SC shower-shape variables, using simulated high-mass DY events. The parameterization is validated with data through a comparison of the central crystal energy with the energy estimated from the parameterization. The energy scale is validated at the 1–2% level using electrons with energy larger than 500 GeV in data. The dominant uncertainty is mainly from the limited number of high-energy electrons available for this study.

5 Electron selection

5.1 Identification

Several strategies are used in CMS to identify prompt isolated electrons (signal), and to separate them from background sources, mainly originating from photon conversions, jets misidentified as electrons, or electrons from semileptonic decays of b and c quarks. Simple and robust algorithms have been developed to apply sequential selections on a set of discriminants. More complex algorithms combine variables in an MVA analysis to achieve better discrimination. In addition, dedicated selections are used for highly energetic electrons.

Variables that provide discriminating power are grouped into three main categories:

- Observables that compare measurements obtained from the ECAL and the tracker (track–cluster matching, including both geometrical as well as SC energy–track momentum matching).
- Purely calorimetric observables used to separate genuine electrons (signal electrons or electrons from photon conversions) from misidentified electrons (e.g., jets with large electromagnetic components), based on the transverse shape of electromagnetic showers in the ECAL and exploiting the fact that electromagnetic showers are narrower than hadronic showers. Also utilized are the energy fractions deposited in the HCAL (expected to be small, as electromagnetic showers are essentially fully contained in the ECAL), as well the energy deposited in the preshower in the endcaps.
- Tracking observables employed to improve the separation between electrons and charged hadrons, exploiting the information obtained from the GSF-fitted track, and the difference between the information from the KF and GSF-fitted tracks.

An example of the purely-tracking variable f_{brem} was given in Fig. 7. Figure 15 shows examples of ECAL-only and track–cluster matching variables. The simulated signal consists of reconstructed electrons compatible with those generated from $Z \to e^+e^-$ decays, using a run-dependent version of the simulation. The data are electrons reconstructed in a sample dominated by $Z \to e^+e^-$ events. To achieve sufficient purity in data, a stringent requirement of $|m_{e^+e^-} - m_Z| < 7.5\,\text{GeV}$ is made again in data and in simulation, on the invariant mass of the two electrons. Both electrons must be isolated namely, <10% of their transverse momentum is

located in a cone around their directions (using the combined PF-isolation variable, described in Section 5.2). The background sample consists of misidentified electrons from jets in Z+jets data. This sample is selected by requiring a pair of identified leptons (electrons or muons) with an invariant mass compatible with that of the Z boson. To suppress the contribution from events with associated production of W and Z bosons, the imbalance in the transverse momentum of the event is required to be smaller than 25 GeV (which also suppresses $\mathrm{t\bar{t}}$ events). One additional electron candidate must be present in the event, which is required not to be isolated by inverting the selection used for signal. In the $\mathrm{e^+e^-}$+jets events, the invariant mass of the dielectron pair with one misidentified-electron candidate and an electron of opposite sign from the $\mathrm{Z} \to \mathrm{e^+e^-}$ decay must be greater than 4 GeV, in order to reject contributions from lower-mass resonances. As a consequence of these requirements, the control sample consists largely of events with one Z boson and one jet that is misidentified as the additional electron. All signal and background electrons are also required to have $p_\mathrm{T} > 20\,\mathrm{GeV}$.

The distance $\Delta\eta$, previously defined in Section 4.4, is shown in Figs. 15 a) and b). The agreement between data and simulation is very good for electrons in the barrel. Disagreement is observed in the endcaps, which is related to the mismodelled material in simulation. The $\Delta\eta$ indeed increases with the amount of bremsstrahlung, which for the endcaps is somewhat larger in data than in simulation.

The lateral extension of the shower along the η direction is expressed in terms of the variable $\sigma_{\eta\eta}$, which is defined as $(\sigma_{\eta\eta})^2 = [\sum(\eta_i - \overline{\eta})^2 w_i] / \sum w_i$. The sum runs over the 5×5 matrix of crystals around the highest E_T crystal of the SC, and w_i is a weight that depends logarithmically on the contained energy. The positions η_i are expressed in units of crystals, which has the advantage that the variable-size gaps between ECAL crystals (in particular at modules boundary) can be ignored. The variable $\sigma_{\eta\eta}$ is shown in Figs. 15 c) and d). The discrimination power of the $\sigma_{\eta\eta}$ is greater than the analogous variable in ϕ, because bremsstrahlung strongly affects the pattern of energy deposition in the ECAL along the ϕ direction. A small disagreement between data and simulation is visible in the barrel, and is mainly due to the limited tuning of electromagnetic showers in simulation (improved in GEANT4 Release 10.0 [36]). For electrons in the endcaps, the main factor determining the resolution of the shower-shape variables is the pileup. Since this is well described in the run-dependent version of simulation, the agreement between data and simulation in these plots is regarded as quite good.

Finally, Figs. 15 e) and f) show the distributions in $1/E_\mathrm{SC} - 1/p$, where E_SC is the SC energy and p the track momentum at the point of closest approach to the vertex. Good agreement is observed between data and simulation both in the barrel and in the endcaps. In all cases, the distributions for signal and background electrons are well separated.

To maximize the sensitivity of electron identification, several variables are combined using the "boosted decision tree" (BDT) algorithm [26]. The set of observables in each category is extended relative to the simpler sequential selection as follows: the track–cluster matching observables are computed both at the ECAL surface and at the vertex, the SC substructure is exploited, more information related to the cluster shape is used, as well as the f_brem fraction. Similar sets of variables are used for electrons in the barrel and in the endcaps. Two types of BDT are defined that depend on whether the electron passes HLT identification requirements ("*triggering* electron") or does not ("*not-triggering* electron"). For triggering electrons, loose identification and isolation requirements are applied as a preselection, to mimic the requirements applied at the HLT. Dedicated training then can exploit the variables discriminating power at best in the remaining phase space. In the following, results are presented just for not-triggering electrons, since the training and performance of the two algorithms are similar. The

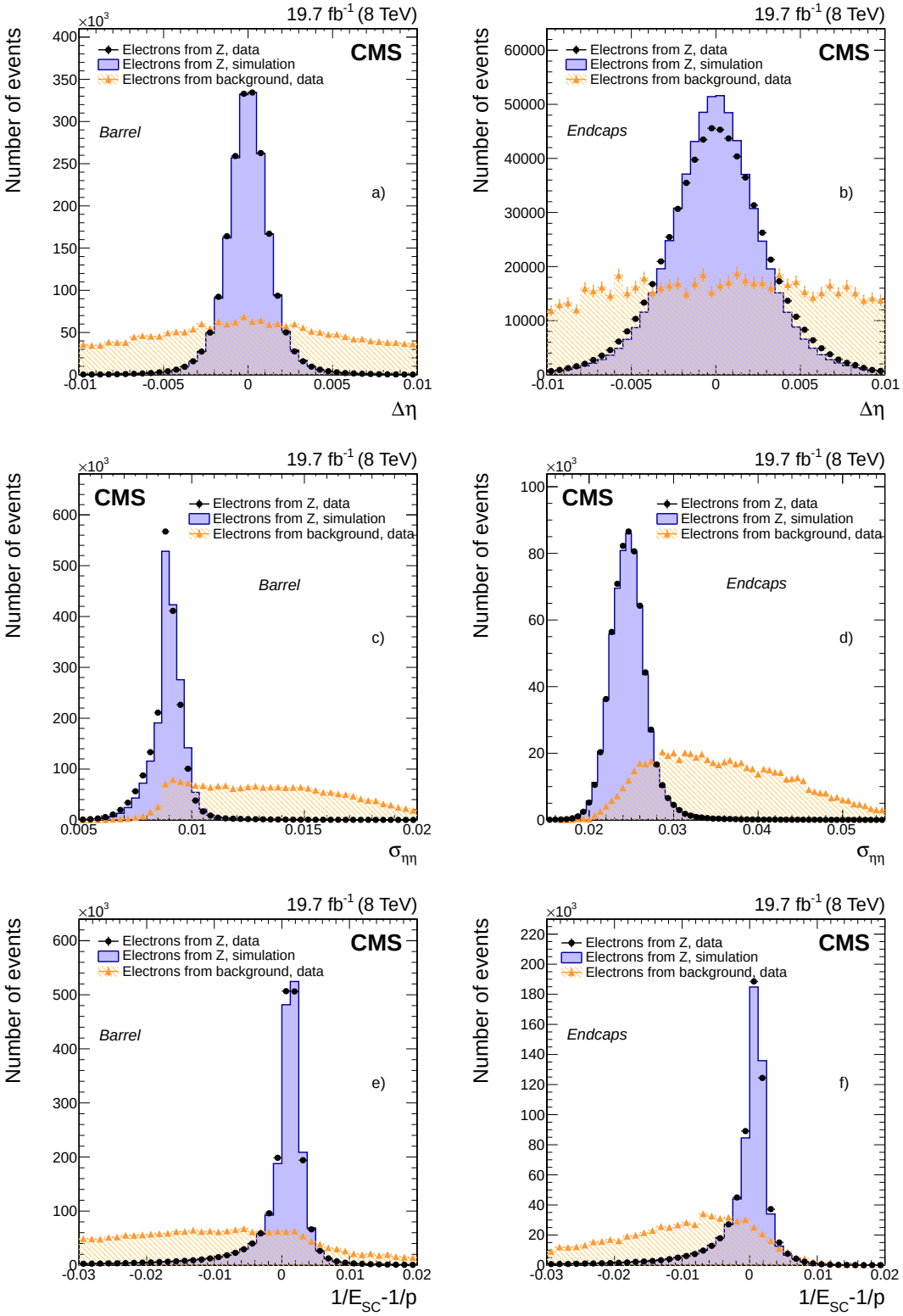

Figure 15: Distributions in the distance $\Delta\eta$ between the position of the SC and the track extrapolated to the point of closest approach to the SC are shown for a) the barrel and b) the endcaps. Distributions in the shower-shape variable $\sigma_{\eta\eta}$, defined in the text, are shown in c) and d). Distributions in energy-momentum matching $1/E_{\mathrm{SC}} - 1/p$, as defined in the text, are shown in e) and f). Distributions are shown for electrons from $Z \to e^+e^-$ data (dots) and simulated (solid histograms) events, and from background-enriched events in data (triangles). All distributions are normalized to their respective areas of the $Z \to e^+e^-$ data. (See text for details on the samples composition.)

BDT is trained in several bins of p_T and η. To model the signal, reconstructed electrons are used when they match electrons with p_T in the range between 5 and 100 GeV in generated events. The background is modelled using misidentified electrons reconstructed in W+jets events in data. The distribution of variables in these training samples is found to be in agreement with that in the analysis samples. The signal and background BDT output distributions are compared in Fig. 16, where there is also a comparison given between data and simulation for signal electrons. The same selections are used as in Fig. 15, and the same signal and background samples. The discriminating power of the MVA algorithm is evident, and the agreement between data and simulation is good. The small difference observed is due to the differences in input variables, which was described in the previous paragraphs.

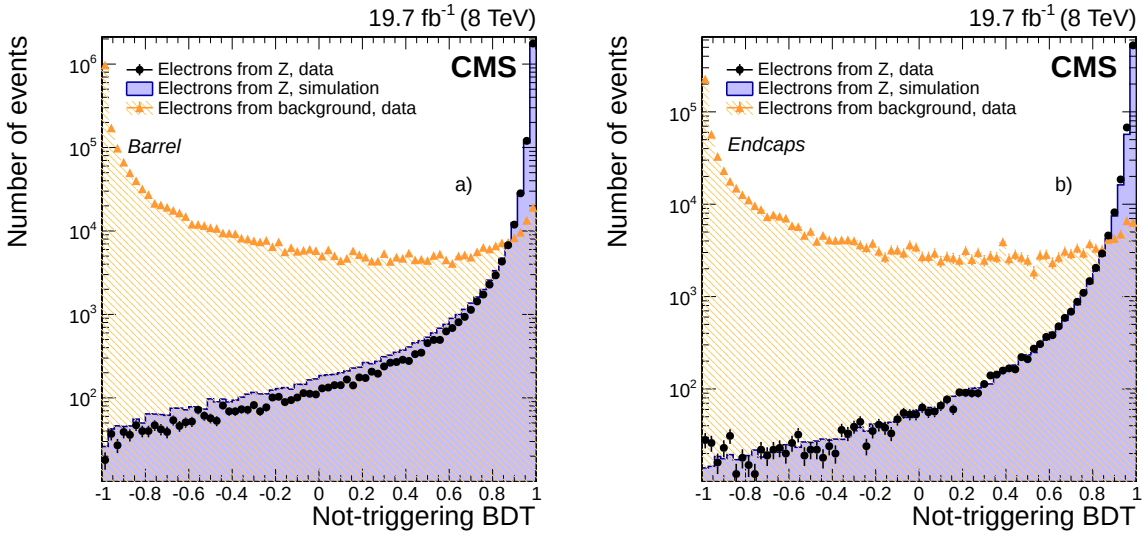

Figure 16: Output of the electron-identification BDT for electrons from $Z \to e^+e^-$ data (dots) and simulated (solid histograms) events, and from background-enriched events in data (triangles), in the ECAL a) barrel, and b) endcaps. All the distributions are normalized to the area of the respective $Z \to e^+e^-$ data. (See text for details on the samples composition.)

The results on the performance of the BDT-based and the sequential electron-identification algorithms for four selected working points are compared in Fig. 17 for electrons with $p_T >$ 20 GeV. Signal electrons from $Z \to e^+e^-$ events in a simulated sample are compared with misidentified electrons from jets reconstructed in data. The same selections and samples are used as in Fig. 15. As expected, better performance is obtained when the variables are combined in an MVA discriminant such as the BDT. In the ECAL barrel and endcaps, a working point of the sequential selection with respective efficiency for signal electrons of about 90% and 84%, has an efficiency of about 7% and 9% on background electrons. For the same signal efficiency, the misidentification probability using the BDT algorithm is reduced by about a factor of two.

Although the focus of the analysis thus far has been on electrons with $p_T > 20$ GeV, this identification strategy is also adopted at smaller p_T. The agreement between data and simulation in the p_T range between 7 and 15 GeV was studied using electrons from J/ψ meson decays. As an illustration, Fig. 18 shows a comparison between data and simulation for two variables, using events with both electrons in the barrel, and the run-dependent version of simulation. The remnant background is subtracted statistically, using the sPlot technique [37], through a fit to the dielectron invariant mass. The agreement between data and simulation is very good both for variables such as $\sigma_{\eta\eta}$ in Fig. 18 a), but also for more complex ones, such as the BDT output shown in Fig. 18 b).

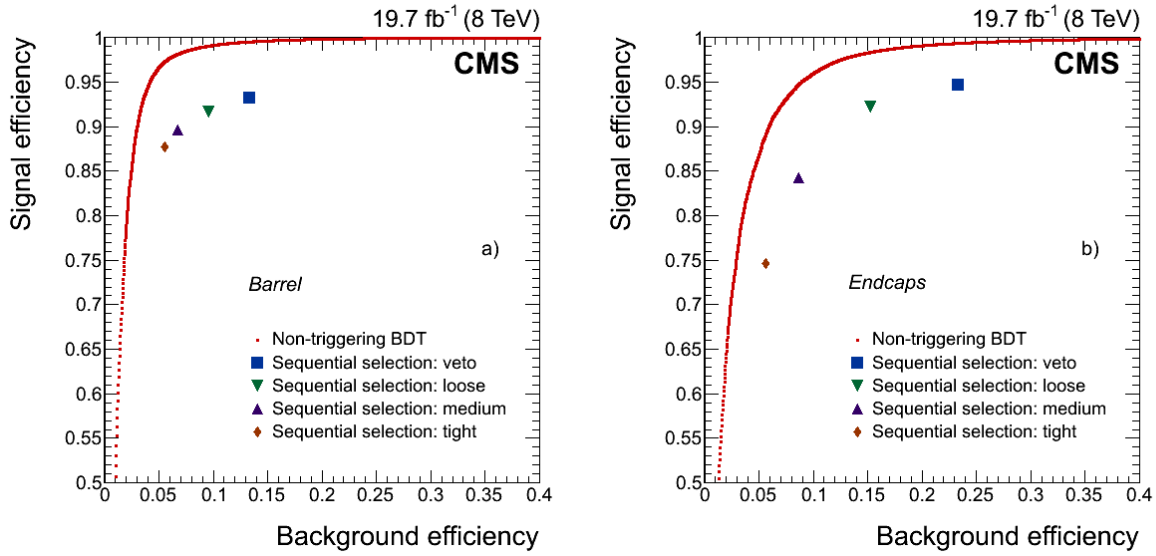

Figure 17: Performance of the electron BDT-based identification algorithm (red dots) compared with results from working points of the sequential selection (only the identification part) for electron candidates in the ECAL a) barrel, and b) endcaps. (See text for details on the samples composition.)

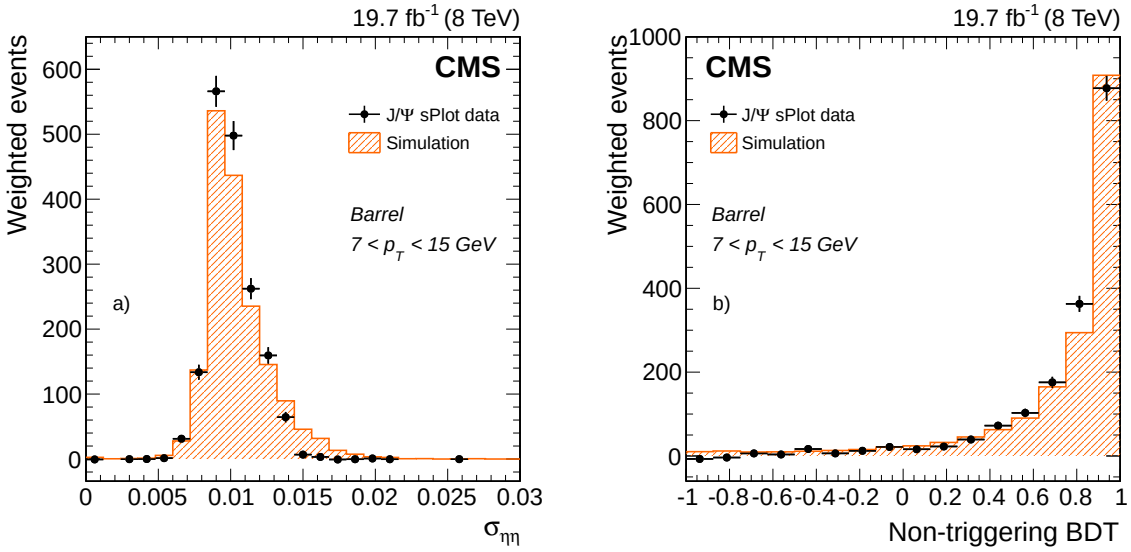

Figure 18: Distribution of a) the shower-shape variable $\sigma_{\eta\eta}$, defined in the text, and b) the output of the BDT electron identification algorithm for electron candidates in the ECAL barrel, in data (symbols) and simulation (histograms). A statistical subtraction of the background is applied using the sPlot technique. (See text for details.)

5.2 Isolation requirements

A significant fraction of background to isolated primary electrons is due to misidentified jets or to genuine electrons within a jet resulting from semileptonic decays of b or c quarks. In both cases, the electron candidates have significant energy flow near their trajectories, and requiring electrons to be isolated from such nearby activity greatly reduces these sources of background. The isolation requirements are separated from electron identification, as the interplay between them tends to be analysis-dependent. Moreover, the inversion of isolation requirements, independent of those used for identification, provides control of different sources of such backgrounds in data.

Two isolation techniques are used at CMS. The simplest one is referred to as detector-based isolation, and relies on the sum of energy depositions either in the ECAL or in the HCAL around each electron trajectory, or on the scalar sum of the p_T of all tracks reconstructed from the collision vertex. These sums are usually computed within cone radii of $\Delta R = 0.3$ or 0.4 around the electron direction, and remove contributions from the electron through smaller exclusion cones. This procedure, which has good performance in rejecting jets misidentified as electrons, is used by the HLT, and in certain analyses in which just mild background rejection suffices.

Most of the offline analyses, however, benefit from the PF technique for defining isolation quantities. Rather than using energy measurements in independent subdetectors, the isolation is defined using the PF candidates reconstructed with a momentum direction within some chosen cone of isolation. In this way, the correct calibration can be used, and a possible double-counting of energy assigned to particle candidates is avoided. When an electron candidate is misidentified by the PF as another particle, it enters the isolation sum, and artificially increases the size of the isolation observable. This effect increases when the identification efficiency of the PF decreases. Electron-candidate identification using PF performs very well for electrons in the ECAL barrel, where no additional corrections for removing electron contributions to the isolation sum are needed. However, in the endcaps, and in the version of the reconstruction used for the results discussed in this paper, the electron identification applied through the PF is not fully efficient. Therefore, in line with what is done in the detector-based approach, veto cones are applied for charged hadrons and photons when the isolation sums are computed.

A comparison between the performance of the two techniques is given in Fig. 19 for electrons with $p_T > 20\,\text{GeV}$ (with no pileup correction applied). Signal electrons from $Z \to e^+e^-$ events in a simulated sample are compared with misidentified electrons from jets reconstructed in Z+jets data. The run-dependent version of the simulation is used. A loose identification is applied in reconstructing PF electrons, and only the electron candidates that pass this selection are considered in performing a meaningful comparison. Better performance is obtained when the information from all detectors is combined using the PF technique, especially in the endcaps.

The PF isolation is defined as

$$\text{Iso}_{\text{PF}} = \sum p_T^{\text{charged}} + \max\Big[0,\ \sum p_T^{\text{neutral had}} + \sum p_T^{\gamma} - p_T^{\text{PU}}\Big], \tag{2}$$

where the sums run over the charged PF candidates, neutral hadrons and photons, within a chosen ΔR cone around the electron direction. The charged candidates are required to originate from the vertex of the event of interest, and p_T^{PU} is a correction related to event pileup. The isolation-related quantities are among the observables most sensitive to the extra energy from pileup interactions (either occurring in the same or earlier bunch crossings), which spoils the isolation efficiency when there are many interactions per bunch crossing. The contribution from pileup in the isolation cone, which must be subtracted, is computed using the FASTJET

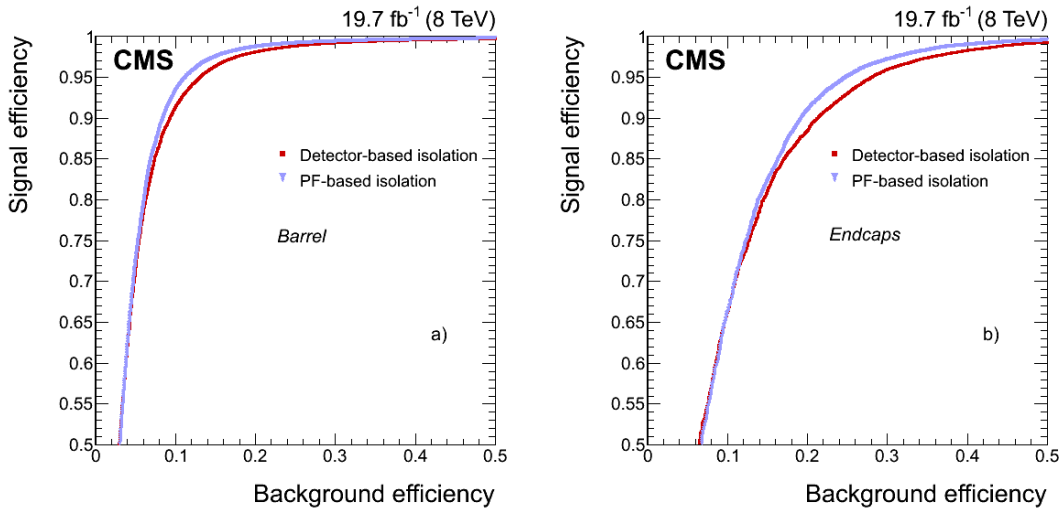

Figure 19: Performance of the detector-based isolation algorithm (red squares) compared with that using PF (blue triangles) in the ECAL a) barrel, and b) endcaps. (See text for the definition of the samples.)

technique [38–40], assuming $p_{\mathrm{T}}^{\mathrm{PU}} = \rho A_{\mathrm{eff}}$ (the variable ρ is defined in Section 4.8.2). The dependence of ρ on pileup is shown in Fig. 20 a), and refers to electrons selected in a data sample dominated by $\mathrm{Z} \to \mathrm{e}^{+}\mathrm{e}^{-}$ events. The dependence of both the charged and neutral components of the PF-based isolation is also shown as a function of the number of reconstructed proton-proton collision vertices. The charged component of the isolation becomes independent of pileup once only candidates compatible with the vertex of interest are considered. For both ρ and the neutral component of the isolation, the dependence is almost linear. The effective area A_{eff} in (η, ϕ) for each component of the isolation is defined by $(\Delta R)^2$, scaled by the ratio of the slopes for ρ and for that specific component shown in Fig. 20 a). Once the correction is applied to the neutral components, the dependence on the number of vertices is much reduced, as shown in Fig. 20 b). The plots refer to electrons with $|\eta| < 1$, but similar conclusions hold in any range of η.

Figure 21 shows the distributions of the $\mathrm{Iso}_{\mathrm{PF}}$ variable divided by the electron p_{T}, for signal and background electrons, after the correction for pileup contributions. For signal electrons, both data and simulation are shown. The samples and selection criteria presented in Section 5.1 are used without the isolation requirement which is replaced by a loose selection on the BDT identification discriminant. Excellent discrimination is observed between signal and background, and there is also good agreement between data and simulation. The remnant discrepancy in the endcaps is mostly due to the difference of the PF electron identification efficiency in data and in simulation, which is reflected in different contributions from misidentified particles to the isolation sums as discussed above. This difference is not completely recovered through the use of the additional exclusion cones.

5.3 Rejection of converted photons

An important source of background to prompt electrons arises from secondary electrons produced in conversions of photons in the tracker material.

To reject this background, CMS algorithms exploit the pattern of track hits. When photon conversions take place inside the volume of the tracker, the first hit on electron tracks from the converted photons is often not located in the innermost layer of the tracker, and missing hits

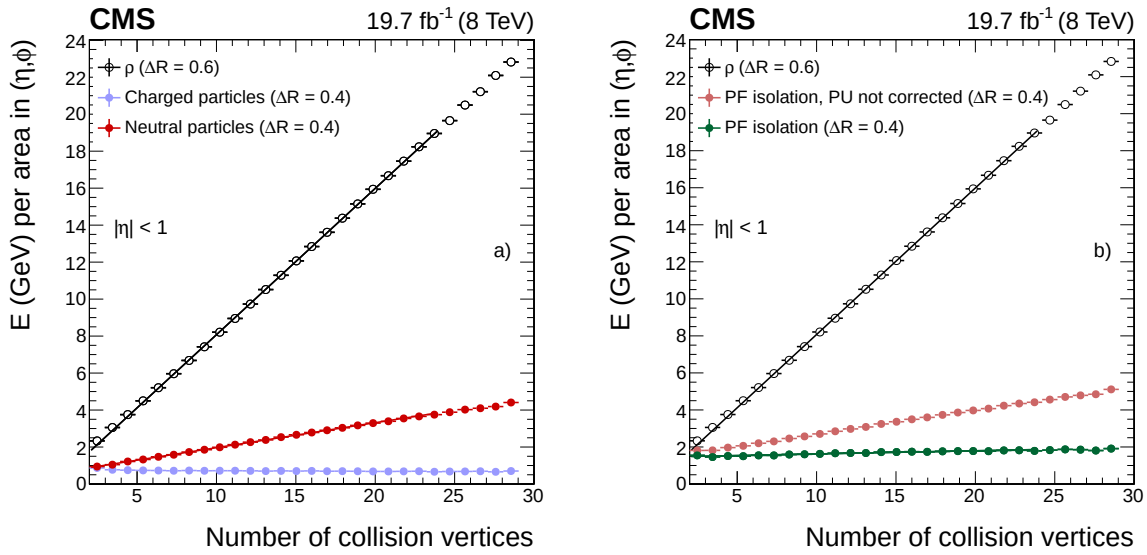

Figure 20: Average energy density as a function of the number of reconstructed proton-proton collision vertices, for electron candidates with $p_T > 20\,\text{GeV}$ and $|\eta| < 1$ from data dominated by $Z \to e^+e^-$ events. The energy density is shown a) for the event ρ (open dots) and separated components of the particle isolation: neutral particles (red dots) and charged particles associated with the vertex (blue dots), and b) after the correction for pileup on PF isolation.

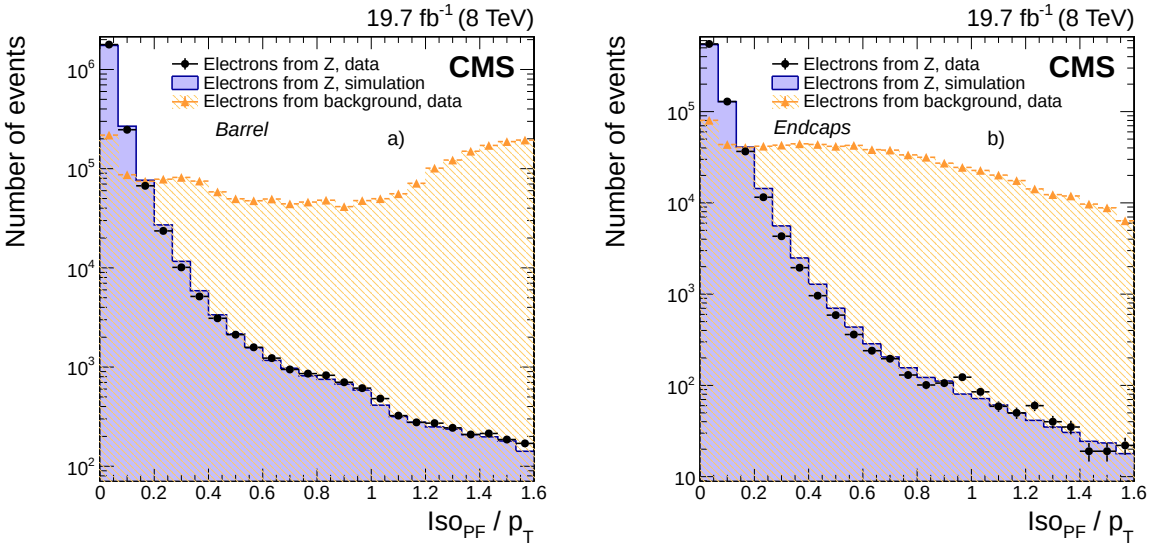

Figure 21: Distributions of PF isolation divided by electron p_T, after applying the pileup correction discussed in the text, for electrons from $Z \to e^+e^-$ data (dots) and simulated (solid histograms) events, and from background-enriched events in data (triangles), in the ECAL a) barrel, and b) endcaps. (See text for more details on the compositions of the samples.)

are therefore present in that region. For prompt electrons, whose trajectories start from the beamline, no missing hits are expected in the inner layers. In addition to the missing hits, photon conversion candidates can also be rejected using a fit to the reconstructed electron tracks. Since the photon is massless, and momentum transfer is in general small, the conversions have a well defined topology, with tracks that have essentially the same tangent at the conversion vertex in the (r, ϕ) and (r, z) planes. The strategy for rejecting these candidates consists of fitting the track pairs to a common vertex, incorporating this topological constraint, and then rejecting the converted photon candidates according to the χ^2 probability of the fit. Also, the impact parameters (ip) of the electron, such as the transverse (d_0) and longitudinal (d_z) distance to the vertex at the point of closest approach in the transverse plane, or the ratio of the uncertainties in the three-dimensional impact parameter relative to its value ($\sigma_{\mathrm{ip}}/\mathrm{ip}$) are used to reject secondary electrons.

Overall, when the requirement of no missing hits together with a selection on the χ^2 probability of the described fit to a common vertex are applied, the inefficiency for prompt electrons in a simulated $\mathrm{Z} \to \mathrm{e}^+\mathrm{e}^-$ sample is of the order of a percent. The rejection factor computed for the background data described in the previous paragraphs is about 45%. These performance figures depend strongly on the selections applied to define the electron candidates, since that affects the background composition, and therefore the fraction of photon conversions. The quoted numbers refer to electron candidates passing the "MVA selection" detailed in Section 5.4, without using the selection based on the number of missing hits.

The algorithms described above are used in combination with other selection variables discussed in the next section to select prompt electrons.

5.4 Reference selections

Scientific analyses must balance efficiency and purity, depending on the levels of signal and background, by defining their own electron selections through a combination of different algorithms. This subsection summarizes some of the basic selections used widely at CMS. The efficiency and misidentification rates, along with a discussion of a tag-and-probe method used to check the performance, are given in Section 6.

The sequential selection applies requirements on five identification variables among those discussed previously: $\Delta\eta$, $\Delta\phi$, H/E_{SC}, $\sigma_{\eta\eta}$, and $1/E_{\mathrm{SC}} - 1/p_{\mathrm{in}}$. In addition, a selection is also applied on the combined PF isolation relative to the electron p_{T}, and on the variables used to reject converted photons. Finally, the impact parameters of the electron, d_0 and d_z, are required to be small for the electron to originate from the vertex of interest. The sequential selection, initially developed for measuring the W boson and Z boson cross sections, is still used in standard model analyses, where the yield of signal is not too small so that the efficiency is not the most important issue. Three working points were originally designed to have average efficiencies of about 90, 80, and 70% for electrons from $\mathrm{Z} \to \mathrm{e}^+\mathrm{e}^-$ events, and were optimized separately for electrons in the ECAL barrel and endcaps. For the analysis of 8 TeV data, four working points are defined: loose, medium, tight, and a very loose point for analyses aiming at vetoing electrons. The selections corresponding to the medium working point are given in Table 6.

The MVA selection combines requirements on the output of the identification BDT described in Section 5.1, on the combined PF isolation, and on rejection variables for photon conversion. The example discussed in this paper is the selection used in the search for the $\mathrm{H} \to \mathrm{ZZ}^* \to 4\ell$ process [9], which exploits the BDT optimized to identify electrons that are not required to pass the trigger selection. In the training, the BDT for these not-triggering electrons does not use any variables related to electron impact parameters, or variables used to suppress conversions.

Table 6: Requirements corresponding to the medium working point of the sequential selection for electrons in the ECAL barrel and endcaps. At most one missing hit is allowed.

Variable	Upper value, barrel	Upper value, endcaps
$\lvert\Delta\eta\rvert$	0.004	0.007
$\lvert\Delta\phi\rvert$	0.06 rad	0.03 rad
H/E_{SC}	0.12	0.10
$\sigma_{\eta\eta}$	0.01	0.03
$\lvert 1/E_{\mathrm{SC}} - 1/p\rvert$	0.05 GeV^{-1}	0.05 GeV^{-1}
$\mathrm{Iso}_{\mathrm{PF}}$ (ΔR=0.3) / p_{T}	0.15	0.15
$\lvert d_0\rvert$	0.02 cm	0.02 cm
$\lvert d_z\rvert$	0.1 cm	0.1 cm
Missing hits	1	1
Conversion-fit probability	10^{-6}	10^{-6}

Therefore such variables can be exploited in scientific analyses. For the $\mathrm{H} \to \mathrm{ZZ}^* \to 4\ell$ analysis, a requirement on the significance of the three-dimensional impact parameter $\lvert\sigma_{\mathrm{ip}}/\mathrm{ip}\rvert < 4$ is applied, and the number of missing hits is required to be at most 1. The combined $\mathrm{Iso}_{\mathrm{PF}}/p_{\mathrm{T}}$ is required to be less than 0.4 in a cone of $\Delta R = 0.4$. The selection is optimized in six categories of electron p_{T} and η to maximize the expected sensitivity, using two p_{T} ranges ($7 < p_{\mathrm{T}} < 10\,\mathrm{GeV}$, and $p_{\mathrm{T}} > 10\,\mathrm{GeV}$), and three $\lvert\eta\rvert$ regions ($\lvert\eta\rvert < 0.80$, $0.80 < \lvert\eta\rvert < 1.48$, and $1.48 < \lvert\eta\rvert < 2.50$), corresponding to two regions in the barrel with different amounts of material in front of the ECAL, and one region in the endcaps. The MVA selection is used mainly in analyses that require high efficiency down to low p_{T}, as well as sufficient background rejection. Examples of such analyses are the Higgs boson searches in leptonic final states.

In addition, CMS has developed a specialized algorithm for the selection of high-p_{T} electrons (HEEP, i.e. High Energy Electron Pairs). Variables similar to those in the sequential selection are used to select large-p_{T} electrons, starting at 35 GeV and up to about 1 TeV. The main difference is the usage of the detector-based isolation instead of PF isolation (the two algorithms offer similar performance). Also, in the barrel, the ratio of the energy collected in $n \times m$ arrays of crystals (either $E_{1\times5}/E_{5\times5}$ or $E_{2\times5}/E_{5\times5}$) is used, since this is found to be more effective at high p_{T} than using $\sigma_{\eta\eta}$. This selection was adopted in many of the searches for exotic particles published by the CMS experiment, e.g. Ref. [10].

6 Electron efficiencies and misidentification probabilities

A method based on the tag-and-probe (T&P) technique [41] exploits $\mathrm{Z}/\gamma^* \to \mathrm{e}^+\mathrm{e}^-$ events in data to estimate the reconstruction and selection efficiencies for signal electrons. The method requires one electron candidate, called the "tag", to satisfy tight selection requirements. Different criteria are tried to define the tag electron, and it is found that the estimated efficiencies are almost insensitive to any specific definition of the tag. For the results in this paper, tag electrons are required to satisfy the tight working point of the sequential selection or, for analyses involving very high-p_{T} electrons, to satisfy the HEEP selection. A second electron candidate, called the "probe", is required to pass specific criteria that depend on the efficiency under study. The invariant mass of the two electrons is required to be within a window around the Z boson mass of $60 < m_{\mathrm{e^+e^-}} < 120\,\mathrm{GeV}$, ensuring thereby high purity of the probe sample and, at the same time, a sufficiently large mass region for fits to extract the background. A requirement for having leptons of opposite charge can also be enforced. When more than two tag–probe matches are found, they are all used in the procedure to minimize possible biases produced by some

specific choice.

The number of probes passing any chosen selection is determined from fits to the invariant mass distribution that include contributions from signal and background. Different models can be used in the fit to disentangle the two components. The background fraction is usually described by an exponential form, convolved with an error function that reflects the kinematic cutoffs of the p_T of the probe electron. The fit to the signal component can use analytic expressions, or be based on templates from simulation. When using analytical functions, a Breit–Wigner function with the Z boson mass and natural width taken from Ref. [42] is convolved with a Crystal Ball function that acts as the resolution function. If a template from simulation is used, the signal part of the distribution is modelled through a sample of simulated electrons from $Z \to e^+e^-$ decays, convolved with a resolution function to account for any remnant differences in resolution between data and simulation. In all cases, a simultaneous fit is performed for events where probes pass or fail the requirements, to account for their correlation. An alternative to fitting is the subtraction of the background contribution using predictions from simulation or techniques based on control samples in data. This is the case of the HEEP selection efficiency, as detailed in the following.

The same T&P technique is applied to data and simulated events to compare efficiencies, and to evaluate the data-to-simulation ratios. In many analyses, these scaling factors are applied as corrections to the simulation, or are used in computing systematic uncertainties. The efficiency in simulation is estimated from $Z \to e^+e^-$ signal samples that contain no background. A geometrical match with generated electrons is often requested to resolve ambiguities that may arise, mainly at low p_T. In data, the events used in the T&P procedure are required to satisfy HLT paths that do not bias the efficiency under study. For the reconstruction efficiency, only triggers requiring one electron and one SC are used, where the tag is matched to the trigger-electron candidate and the probe is matched to the trigger SC. For selection efficiencies, triggers requiring two electrons with requirements that are less restrictive than those under study can also be used. In such cases, the offline tag and probe are requested to match a trigger-electron candidate.

The fits are performed in η and p_T bins, and an example of a fit to data is shown in Fig. 22. The fits to probe electrons that pass or fail the selections are shown, respectively in a) and b).

Several sources of systematic uncertainty are considered in the fits. The main uncertainty is related to the model used in the fit, and is estimated by comparing alternative distributions for signal and background, in addition to comparing analytic functions with templates from simulation. Only a small dependence is found on the number of bins used in the fits and on the definition of the tag, such as on the reweighting of the simulation to match the pileup in data. Different event generators are also compared in the analyses, and the differences among them are found to be negligible.

6.1 Reconstruction efficiency

The reconstruction efficiency is computed as a function of the E_T^{SC} and η of the SC, and covers all reconstruction effects. The SC reconstruction efficiency for $E_T^{SC} > 5\,\text{GeV}$ is close to 100%. To illustrate the nature of the results, the electron reconstruction efficiencies measured in data and in DY simulated samples are shown in Fig. 23, together with the data-to-simulation scale factors, as a function of E_T^{SC}, for a) $|\eta| < 0.8$, and b) $1.57 < |\eta| < 2$.

The efficiencies are found to be >85% for $E_T^{SC} > 10\,\text{GeV}$, for all η. They are compatible in data and simulation, giving scale factors consistent with unity almost in the entire range. The

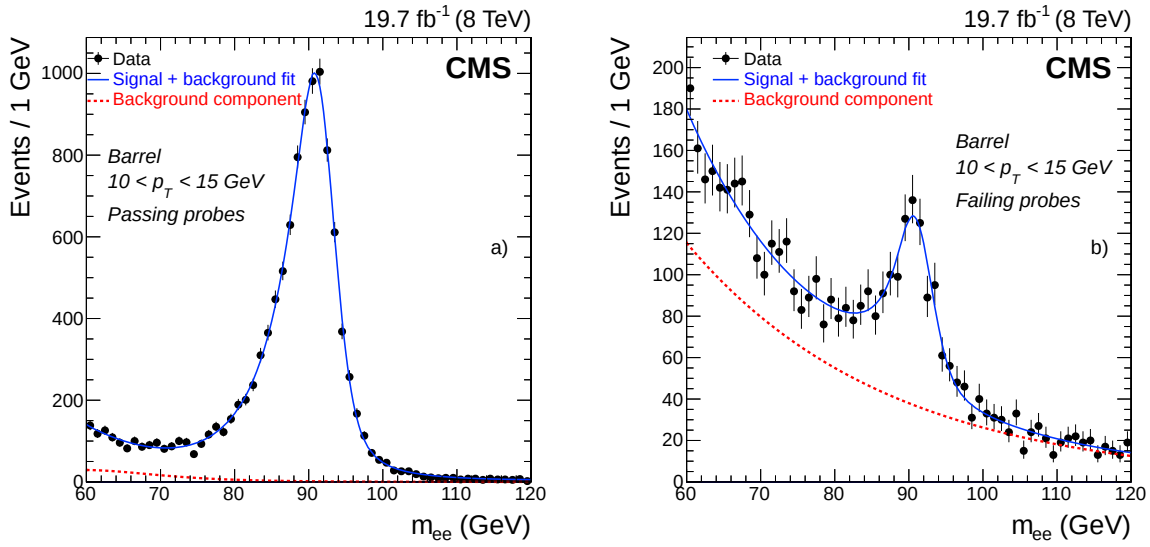

Figure 22: Example of fits to dielectron invariant mass distributions for probe electrons with $10 < p_{\mathrm{T}} < 15\,\mathrm{GeV}$ in the ECAL barrel that a) pass or b) fail the selections on isolation and impact parameter of the MVA selection used in Ref. [9]. Fits are shown for the signal+background hypothesis (full line), and for the background component alone (dashed line).

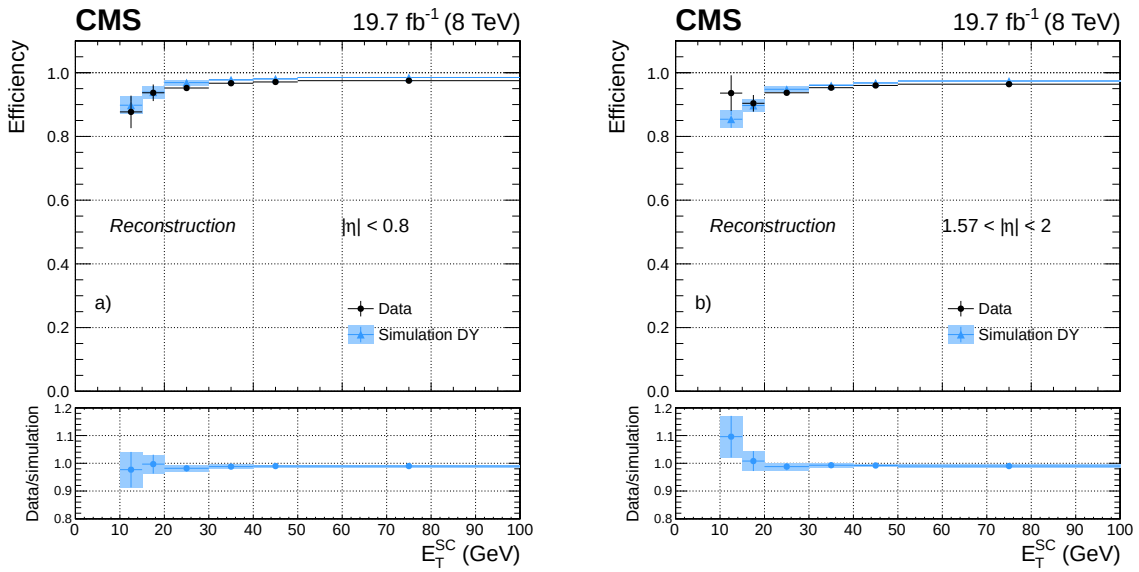

Figure 23: Electron reconstruction efficiency measured in dielectron events in data (dots) and DY simulation (triangles), as a function of the electron $E_{\mathrm{T}}^{\mathrm{SC}}$ for a) $|\eta| < 0.8$, and b) $1.57 < |\eta| < 2$. The bottom panels show the corresponding data-to-simulation scale factors.

uncertainties shown on the plots correspond to the quadratic sum of the statistical and systematic contributions, dominated by the systematic components, at the level of a few percent for $E_{\mathrm{T}}^{\mathrm{SC}} < 20\,\mathrm{GeV}$ and decreasing to <1% as $E_{\mathrm{T}}^{\mathrm{SC}}$ increases. The main uncertainty is related to the fitting function. The background contamination is large in the estimation of reconstruction efficiency, and additional requirements are therefore applied, such as requiring the imbalance in p_{T} in the event to be <20 GeV. Also, the probe must be isolated, and the p_{T} sum of all tracks from the vertex of interest that fall into the isolation cone must be <15% of the probe $E_{\mathrm{T}}^{\mathrm{SC}}$. The definition of these extra requirements is the second-highest source of systematic uncertainty in this measurement.

6.2 Selection efficiency

The selection efficiency is computed for reconstructed electrons in bins of the electron p_{T} and of the η of the SC. For the sequential selection, the efficiencies of the medium working point in data and in simulation are presented as a function of electron p_{T} in Fig. 24 for a) $|\eta| < 0.8$, and b) $1.57 < |\eta| < 2$. The corresponding data-to-simulation scale factors are shown in the bottom panels. Similarly, Figs. 24 c) and d) show the efficiencies as a function of p_{T} for the BDT selection, discussed in the previous section. The selections are optimized respectively for $p_{\mathrm{T}} > 10\,\mathrm{GeV}$ and $p_{\mathrm{T}} > 7\,\mathrm{GeV}$, which are the ranges shown in the plots. In general, data and simulation agree well. The scale factors are compatible with unity, with the exception of the low-p_{T} region ($7 < p_{\mathrm{T}} < 15\,\mathrm{GeV}$), where they can be as low as 0.85–0.90 depending on the selections. The uncertainties shown include contributions from both the statistical and systematic sources. They are again dominated by systematic contributions, which are at the level of several percent for $p_{\mathrm{T}} < 20\,\mathrm{GeV}$, and decrease below 2% when p_{T} increases, with the exception of the transition region between the barrel and the endcap. As for reconstruction efficiencies, the main uncertainty originates from the choice of the fitting function. It is verified that efficiencies are almost uniform as a function of the number of reconstructed interaction vertices. As expected, the less restrictive the selection, the smaller is the remnant dependence on pileup. For the working points illustrated in Fig. 24, the efficiencies decrease only by about 5% and 2% for up to 50 primary vertices, meaning that the proposed selections are almost independent of pileup. The average number of proton-proton interactions per bunch crossing is about 21 in the 8 TeV data.

For the HEEP selection, the efficiency is computed by subtracting the background contribution estimated from simulation, instead of using a fit. This is done especially because of the small number of events at large p_{T} in data. Multijet production, which is among the dominant contributions to the backgrounds to Z+jets, is estimated directly from data using the jet-to-electron misidentification probabilities measured in a dedicated control sample. The measured uncertainty of about 40% in the estimated background is the main source of systematic uncertainty. The efficiency of the HEEP selection in data and in simulation is shown as a function of electron p_{T} in Fig. 25, together with the data-to-simulation scale factors. Because of the limited number of events, only two η bins are considered, corresponding to the ECAL barrel and endcaps. The p_{T} region is restricted to $p_{\mathrm{T}} > 35\,\mathrm{GeV}$, and a wider p_{T} range is covered in the barrel because of the presence of more events there than in the endcaps. In the barrel, the efficiency ranges from 85 to 95%, and the data-to-simulation scale factors are compatible with unity. In the endcaps, the fluctuations are larger, with efficiencies ranging from about 80 to close to 100%. The uncertainties shown in the plots correspond to the quadratic sum of the statistical and systematic contributions. For electrons with $p_{\mathrm{T}} < 100\,\mathrm{GeV}$, the uncertainty is dominated by systematic sources, since this is the region where the background is more important, while above about 100 GeV the statistical uncertainty dominates.

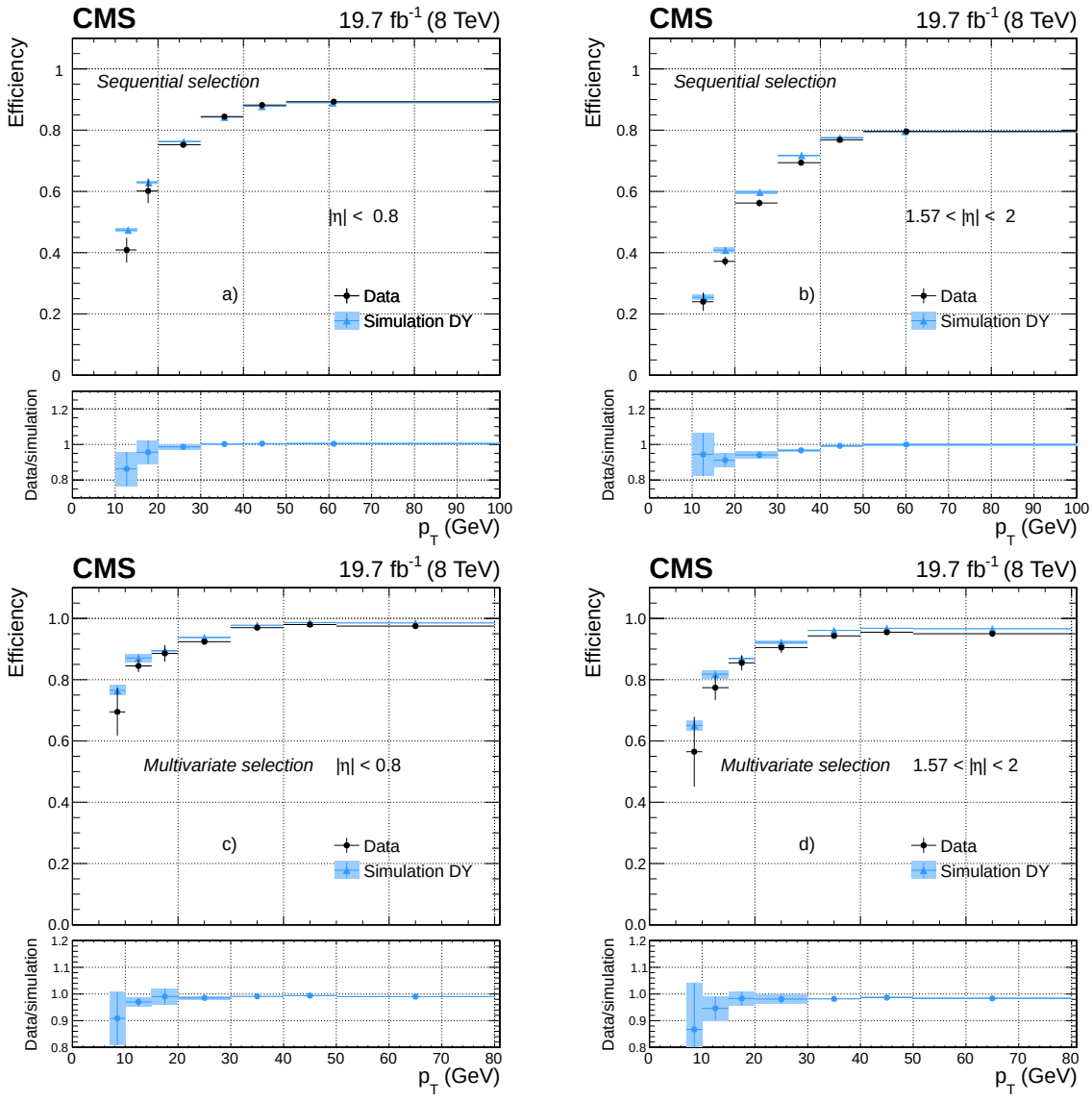

Figure 24: Efficiency as a function of electron p_{T} for dielectron events in data (dots) and DY simulation (triangles), for the medium working point of the sequential selection in a) $|\eta| < 0.8$, and b) $1.57 < |\eta| < 2$; and for the MVA selection used in Ref. [9] in c) $|\eta| < 0.8$, and d) $1.57 < |\eta| < 2$. The corresponding data-to-simulation scale factors are shown in the bottom panels of each plot.

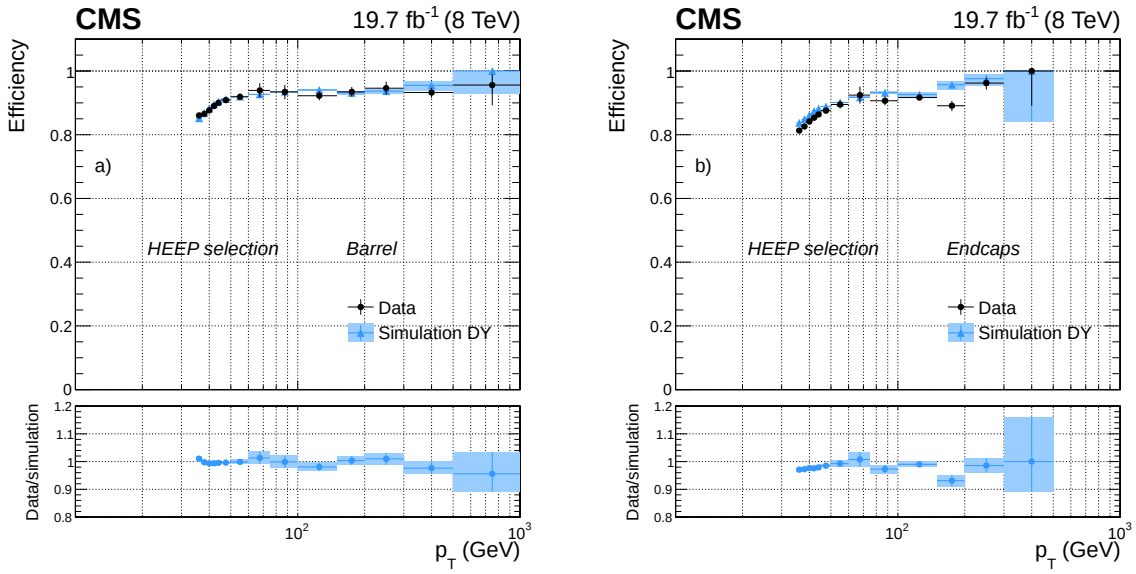

Figure 25: Efficiency of the HEEP selection as a function of electron p_{T} for dielectron events in data (dots) and DY simulation (triangles) in the ECAL a) barrel, and b) endcaps.

6.3 Misidentification probability

To each efficiency corresponds a misidentification probability, defined as the fraction of background candidates reconstructed as electrons that pass some set of selection criteria. The results have their misidentification probability computed using data enriched in Z bosons that also contain an additional electron, as described in Section 5.1.

The fraction of events in which additional reconstructed electron candidates from background contributions pass the medium working point of the sequential selection is shown in Fig. 26 a) as a function of the candidate p_{T}. The same fraction is shown in Fig. 26 b) for the MVA selection. In both cases, the misidentification probability increases with the p_{T} of the candidate. For the working point of the sequential selection, it ranges from 1 to 3.5%, depending on p_{T} and on the region of the detector. For the MVA selection, the chosen working point [9] is less restrictive and the misidentification probability is therefore larger (from 1 to 10.5%).

The main source of systematic uncertainty in the misidentification probability is related to the composition of the sample used to extract its value. For this particular choice, it is mainly related to the contamination from processes with genuine electrons, such as the associated production of W and Z bosons, and $\mathrm{t\bar{t}}$ events. The selection on the imbalance in transverse momentum strongly reduces such contamination, and therefore the systematic uncertainty, with the consequence that the main uncertainty in the analyses comes from the difference between the samples used to extract the misidentification probability and the one to which the result is applied. This is strongly analysis-dependent and therefore not discussed further.

7 Summary and conclusions

The performance of electron reconstruction and selection in CMS has been studied using data collected in proton-proton collisions at $\sqrt{s} = 8\,\mathrm{TeV}$ corresponding to an integrated luminosity of $19.7\,\mathrm{fb}^{-1}$.

Algorithms used to reconstruct electron trajectories and energy deposits in the tracker and ECAL respectively, have been presented. A Gaussian sum filter algorithm used for track recon-

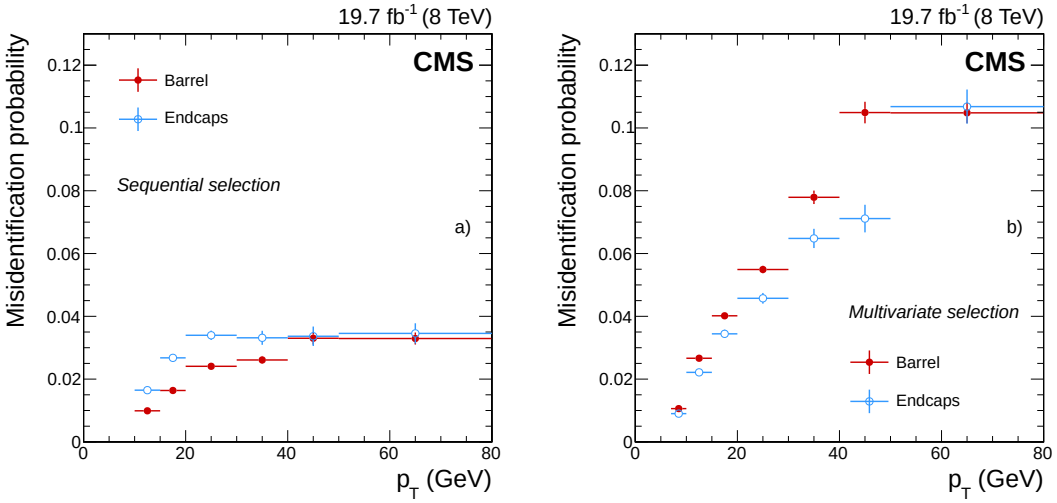

Figure 26: Misidentification probability, measured in data as described in the text, as a function of the electron p_T in the barrel (red dots) and endcaps (blue dots) for candidates passing a) the medium working point of the sequential selection, and b) the working point of the MVA selection used in Ref. [9].

struction provides a way to follow the track curvature and to account for bremsstrahlung loss up to the entrance into the ECAL. The strategies for finding seeds for electron tracks, constructing trajectories, and fitting track parameters are optimized to reconstruct the electrons down to small p_T values with high efficiency and accuracy. Moreover, the clustering of energy in the ECAL and its optimization to recover bremsstrahlung photons are discussed. Dedicated algorithms are used to correct the energy measured in the ECAL as well as to estimate the electron momentum by combining independent measurements in the ECAL and in the tracker.

The overall momentum scale is calibrated with an uncertainty smaller than 0.3% in the p_T range from 7 to 70 GeV. For electrons from Z boson decays, the effective momentum resolution varies from 1.7%, for well-measured electrons with a single-cluster supercluster in the barrel, to 4.5% for electrons with a multi-cluster supercluster, or poorly measured, in the endcaps. The electron momentum resolution is modelled in simulation with a precision better than 10% up to a p_T of 70 GeV.

The performance of the reconstruction algorithms in data is studied together with those of several benchmark selections designed to cover the needs of the physics programme of the CMS experiment. Good agreement is observed between data and predictions from simulation for most of the variables relevant to electron reconstruction and selection. The origin of small remaining discrepancies is understood and corrections will be implemented in the future.

The reconstruction efficiency as well as the efficiency of all the selections are measured using $Z \to e^+e^-$ samples in data and in simulation. The reconstruction efficiency in the data ranges from 88% to 98% in the barrel and from 90% to 96% in the endcaps in the p_T range from 10 to 100 GeV. The ratios of efficiencies of data to simulation, both for reconstruction and for the different proposed selections, are found to be in general compatible with unity within the respective uncertainties, over the full p_T range, down to a p_T as low as 7 GeV. Differences of up to 5% between data and simulation are observed in most cases, while differences of up to 15% are measured for a few points at small p_T values.

The analysis of electron performance with data has shown that, despite the challenging conditions of pileup at the LHC and the significant level of bremsstrahlung in the tracker, using dedi-

cated algorithms and a large number of recorded $Z \to e^+e^-$ decays provided successful means of reconstructing and identifying electrons in CMS. The quality of simulation at the beginning of the experiment was sufficiently good to require only a few adjustments to the originally conceived reconstruction algorithms, and also enabled quick deployment of sophisticated developments, such as PF reconstruction and the use of MVA methods for electron identification and, later, for momentum correction. The reconstruction and selection of electrons at low p_T have been achieved with a performance level close to that anticipated at the time the detector was designed. These achievements, especially for low-p_T electrons, played an essential role in the discovery of the Higgs boson at CMS [43, 44], and in the measurement of its properties [45] in the $H \to ZZ^* \to 4\ell$ channel.

Acknowledgments

We congratulate our colleagues in the CERN accelerator departments for the excellent performance of the LHC and thank the technical and administrative staffs at CERN and at other CMS institutes for their contributions to the success of the CMS effort. In addition, we gratefully acknowledge the computing centres and personnel of the Worldwide LHC Computing Grid for delivering so effectively the computing infrastructure essential to our analyses. Finally, we acknowledge the enduring support for the construction and operation of the LHC and the CMS detector provided by the following funding agencies: the Austrian Federal Ministry of Science, Research and Economy and the Austrian Science Fund; the Belgian Fonds de la Recherche Scientifique, and Fonds voor Wetenschappelijk Onderzoek; the Brazilian Funding Agencies (CNPq, CAPES, FAPERJ, and FAPESP); the Bulgarian Ministry of Education and Science; CERN; the Chinese Academy of Sciences, Ministry of Science and Technology, and National Natural Science Foundation of China; the Colombian Funding Agency (COLCIENCIAS); the Croatian Ministry of Science, Education and Sport, and the Croatian Science Foundation; the Research Promotion Foundation, Cyprus; the Ministry of Education and Research, Estonian Research Council via IUT23-4 and IUT23-6 and European Regional Development Fund, Estonia; the Academy of Finland, Finnish Ministry of Education and Culture, and Helsinki Institute of Physics; the Institut National de Physique Nucléaire et de Physique des Particules / CNRS, and Commissariat à l'Énergie Atomique et aux Énergies Alternatives / CEA, France; the Bundesministerium für Bildung und Forschung, Deutsche Forschungsgemeinschaft, and Helmholtz-Gemeinschaft Deutscher Forschungszentren, Germany; the General Secretariat for Research and Technology, Greece; the National Scientific Research Foundation, and National Innovation Office, Hungary; the Department of Atomic Energy and the Department of Science and Technology, India; the Institute for Studies in Theoretical Physics and Mathematics, Iran; the Science Foundation, Ireland; the Istituto Nazionale di Fisica Nucleare, Italy; the Ministry of Science, ICT and Future Planning, and National Research Foundation (NRF), Republic of Korea; the Lithuanian Academy of Sciences; the Ministry of Education, and University of Malaya (Malaysia); the Mexican Funding Agencies (CINVESTAV, CONACYT, SEP, and UASLP-FAI); the Ministry of Business, Innovation and Employment, New Zealand; the Pakistan Atomic Energy Commission; the Ministry of Science and Higher Education and the National Science Centre, Poland; the Fundação para a Ciência e a Tecnologia, Portugal; JINR, Dubna; the Ministry of Education and Science of the Russian Federation, the Federal Agency of Atomic Energy of the Russian Federation, Russian Academy of Sciences, and the Russian Foundation for Basic Research; the Ministry of Education, Science and Technological Development of Serbia; the Secretaría de Estado de Investigación, Desarrollo e Innovación and Programa Consolider-Ingenio 2010, Spain; the Swiss Funding Agencies (ETH Board, ETH Zurich, PSI, SNF, UniZH, Canton Zurich, and SER); the Ministry of Science and Technology, Taipei; the

Thailand Center of Excellence in Physics, the Institute for the Promotion of Teaching Science and Technology of Thailand, Special Task Force for Activating Research and the National Science and Technology Development Agency of Thailand; the Scientific and Technical Research Council of Turkey, and Turkish Atomic Energy Authority; the National Academy of Sciences of Ukraine, and State Fund for Fundamental Researches, Ukraine; the Science and Technology Facilities Council, UK; the US Department of Energy, and the US National Science Foundation.

Individuals have received support from the Marie-Curie programme and the European Research Council and EPLANET (European Union); the Leventis Foundation; the A. P. Sloan Foundation; the Alexander von Humboldt Foundation; the Belgian Federal Science Policy Office; the Fonds pour la Formation à la Recherche dans l'Industrie et dans l'Agriculture (FRIA-Belgium); the Agentschap voor Innovatie door Wetenschap en Technologie (IWT-Belgium); the Ministry of Education, Youth and Sports (MEYS) of the Czech Republic; the Council of Science and Industrial Research, India; the HOMING PLUS programme of Foundation for Polish Science, cofinanced from European Union, Regional Development Fund; the Compagnia di San Paolo (Torino); the Consorzio per la Fisica (Trieste); MIUR project 20108T4XTM (Italy); the Thalis and Aristeia programmes cofinanced by EU-ESF and the Greek NSRF; and the National Priorities Research Program by Qatar National Research Fund.

References

[1] CMS Collaboration, "CMS: The TriDAS project. Technical design report, Vol.2: Data acquisition and high-level trigger", CMS Technical Design Report CERN-LHCC-2002-026, 2002.

[2] CMS Collaboration, "CMS physics: Technical design report volume 1: Detector performance", CMS Technical Design Report CERN-LHCC-2006-001, 2006.

[3] S. Baffioni et al., "Electron reconstruction in CMS", *Eur. Phys. J. C* **49** (2007) 1099, doi:10.1140/epjc/s10052-006-0175-5.

[4] CMS Collaboration, "Energy calibration and resolution of the CMS electromagnetic calorimeter in pp collisions at $\sqrt{s}$ = 7 TeV", *JINST* **8** (2013) P09009, doi:10.1088/1748-0221/8/09/P09009, arXiv:1306.2016.

[5] CMS Collaboration, "Description and performance of track and primary vertex reconstruction with the CMS tracker", *JINST* **9** (2014) P10009, doi:10.1088/1748-0221/9/10/P10009, arXiv:1405.6569.

[6] CMS Collaboration, "Electron Reconstruction and Identification at $\sqrt{s} = 7$ TeV", CMS Physics Analysis Summary CMS-PAS-EGM-10-004, 2010.

[7] CMS Collaboration, "Electron commissioning results at $\sqrt{s}$ = 7 TeV", CMS Detector Performance Summary CERN-CMS-DP-2011-003, 2011.

[8] CMS Collaboration, "Electron performance with 19.6 fb^{-1} of data collected at $\sqrt{s}$ = 8 TeV with the CMS detector", CMS Detector Performance Summary CERN-CMS-DP-2013-003, 2013.

[9] CMS Collaboration, "Measurement of the properties of a Higgs boson in the four-lepton final state", *Phys. Rev. D* **89** (2014) 092007, doi:10.1103/PhysRevD.89.092007, arXiv:hep-ex/1312.5353.

[10] CMS Collaboration, "Search for heavy narrow dilepton resonances in pp collisions at $\sqrt{s} = 7$ TeV and $\sqrt{s} = 8$ TeV", *Phys. Lett. B* **720** (2013) 63, doi:10.1016/j.physletb.2013.02.003, arXiv:1212.6175.

[11] CMS Collaboration, "The CMS experiment at the CERN LHC", *JINST* **3** (2008) S08004, doi:10.1088/1748-0221/3/08/S08004.

[12] CMS Collaboration, "CMS Luminosity Based on Pixel Cluster Counting - Summer 2013 Update", CMS Physics Analysis Summary CMS-PAS-LUM-13-001, 2013.

[13] CMS Collaboration, "Alignment of the CMS tracker with LHC and cosmic ray data", *JINST* **9** (2014) P06009, doi:10.1088/1748-0221/9/06/P06009, arXiv:1403.2286.

[14] J. Alwall et al., "The automated computation of tree-level and next-to-leading order differential cross sections, and their matching to parton shower simulations", *JHEP* **07** (2014) 079, doi:10.1007/JHEP07(2014)079, arXiv:1405.0301.

[15] P. Nason, "A New method for combining NLO QCD with shower Monte Carlo algorithms", *JHEP* **11** (2004) 040, doi:10.1088/1126-6708/2004/11/040, arXiv:hep-ph/0409146.

[16] S. Frixione, P. Nason, and C. Oleari, "Matching NLO QCD computations with parton shower simulations: the POWHEG method", *JHEP* **11** (2007) 070, doi:10.1088/1126-6708/2007/11/070, arXiv:0709.2092.

[17] S. Alioli, P. Nason, C. Oleari, and E. Re, "A general framework for implementing NLO calculations in shower Monte Carlo programs: the POWHEG BOX", *JHEP* **06** (2010) 043, doi:10.1007/JHEP06(2010)043, arXiv:1002.2581.

[18] T. Sjöstrand, S. Mrenna, and P. Z. Skands, "PYTHIA 6.4 physics and manual", *JHEP* **05** (2006) 026, doi:10.1088/1126-6708/2006/05/026, arXiv:hep-ph/0603175.

[19] CMS Collaboration, "Study of the underlying event at foward rapidity in pp collisions at $\sqrt{s}$ = 0.9, 2.76, and 7 TeV", *JHEP* **04** (2013) 072, doi:10.1007/JHEP04(2013)072, arXiv:1302.2394v2.

[20] GEANT4 Collaboration, "GEANT4—a simulation toolkit", *Nucl. Instrum. Meth. A* **506** (2003) 250, doi:10.1016/S0168-9002(03)01368-8.

[21] J. Allison et al., "GEANT4 developments and applications", *IEEE Trans. Nucl. Sci.* **53** (2006) 270, doi:10.1109/TNS.2006.869826.

[22] CMS Collaboration, "Particle–Flow Event Reconstruction in CMS and Performance for Jets, Taus, and $E_{\mathrm{T}}^{\mathrm{miss}}$", CMS Physics Analysis Summary CMS-PAS-PFT-09-001, 2009.

[23] CMS Collaboration, "Commissioning of the Particle-flow Event Reconstruction with the first LHC collisions recorded in the CMS detector", CMS Physics Analysis Summary CMS-PAS-PFT-10-001, 2010.

[24] P. Adzic et al., "Energy resolution of the barrel of the CMS Electromagnetic Calorimeter", *JINST* **2** (2007) P04004, doi:10.1088/1748-0221/2/04/P04004.

[25] W. Adam, R. Frühwirth, A. Strandlie, and T. Todorov, "Reconstruction of electrons with the Gaussian-sum filter in the CMS tracker at LHC", *J. Phys. G* **31** (2005) N9, doi:10.1088/0954-3899/31/9/N01.

[26] H. Voss, A. Höcker, J. Stelzer, and F. Tegenfeldt, "TMVA, the Toolkit for Multivariate Data Analysis with ROOT", in *XIth International Workshop on Advanced Computing and Analysis Techniques in Physics Research (ACAT)*, p. 40. 2007. arXiv:physics/0703039.

[27] CMS Collaboration, "Performance of photon reconstruction and identification with the CMS detector in proton-proton collisions at $\sqrt{s} = 8$ TeV", (2015). Submitted to JINST.

[28] CMS Collaboration, "Measurement of the electron charge asymmetry in inclusive W production in pp collisions at $\sqrt{s} = 7$ TeV", *Phys. Rev. Lett.* **109** (2012) 111806, doi:10.1103/PhysRevLett.109.111806, arXiv:1206.2598.

[29] CMS Collaboration, "Search for new physics in events with same-sign dileptons and jets in pp collisions at $\sqrt{s} = 8$ TeV", *JHEP* **01** (2014) 163, doi:10.1007/JHEP01(2014)163, arXiv:1311.6736.

[30] M. Anfreville et al., "Laser monitoring system for the CMS lead tungstate crystal calorimeter", *Nucl. Instrum. Meth. A* **594** (2008) 292, doi:10.1016/j.nima.2008.01.104.

[31] L.-Y. Zhang et al., "Performance of the monitoring light source for the CMS lead tungstate crystal calorimeter", *IEEE Trans. Nucl. Sci.* **52** (2005) 1123, doi:10.1109/TNS.2005.852661.

[32] J. H. Friedman, "Greedy function approximation: A gradient boosting machine", *Ann. of Stat.* **29** (2001) 1189, doi:10.1214/aos/1013203451.

[33] S. Catani, Y. L. Dokshitzer, M. H. Seymour, and B. R. Webber, "Longitudinally invariant $k_\perp$ clustering algorithms for hadron-hadron collisions", *Nucl. Phys. B* **406** (1993) 187, doi:10.1016/0550-3213(93)90166-M.

[34] S. D. Ellis and D. E. Soper, "Successive combination jet algorithm for hadron collisions", *Phys. Rev. D* **48** (1993) 3160, doi:10.1103/PhysRevD.48.3160, arXiv:hep-ph/9305266.

[35] M. Oreglia, "A study of the reactions $\psi' \to \gamma\gamma\psi$". PhD thesis, Stanford University, 1980. SLAC Report SLAC-R-236.

[36] GEANT4 Collaboration, "GEANT4 10.0 Release Notes", 2013. http://geant4.cern.ch/support/ReleaseNotes4.10.0.

[37] M. Pivk and F. R. Le Diberder, "sPlot: a statistical tool to unfold data distributions", *Nucl. Instrum. Meth. A* **555** (2005) 356, doi:10.1016/j.nima.2005.08.106, arXiv:physics/0402083.

[38] M. Cacciari and G. P. Salam, "Pileup subtraction using jet areas", *Phys. Lett. B* **659** (2008) 119, doi:10.1016/j.physletb.2007.09.077, arXiv:0707.1378.

[39] M. Cacciari, G. P. Salam, and G. Soyez, "The catchment area of jets", *JHEP* **04** (2008) 005, doi:10.1088/1126-6708/2008/04/005, arXiv:0802.1188.

[40] M. Cacciari, G. P. Salam, and G. Soyez, "FastJet user manual", *Eur. Phys. J. C* **72** (2012) 1896, doi:10.1140/epjc/s10052-012-1896-2, arXiv:1111.6097.

[41] CMS Collaboration, "Measurements of Inclusive W and Z Cross Sections in pp Collisions at $\sqrt{s} = 7$ TeV", *JHEP* **01** (2011) 080, doi:10.1007/JHEP01(2011)080, arXiv:1012.2466.

[42] Particle Data Group, K. A. Olive et al., "The Review of Particle Physics", *Chin. Phys. C* **38** (2014) 090001, doi:10.1088/1674-1137/38/9/090001.

[43] CMS Collaboration, "Observation of a new boson at a mass of 125 GeV with the CMS experiment at the LHC", *Phys. Lett. B* **716** (2012) 30, doi:10.1016/j.physletb.2012.08.021.

[44] CMS Collaboration, "Observation of a new boson with mass near 125 GeV in pp collisions at $\sqrt{s}$ = 7 and 8 TeV", *JHEP* **06** (2013) 081, doi:10.1007/JHEP06(2013)081, arXiv:1303.4571.

[45] CMS Collaboration, "Precise determination of the mass of the Higgs boson and tests of compatibility of its couplings with the standard model predictions using proton collisions at 7 and 8 TeV", (2014). arXiv:1412.8662.

A The CMS Collaboration

Yerevan Physics Institute, Yerevan, Armenia
V. Khachatryan, A.M. Sirunyan, A. Tumasyan

Institut für Hochenergiephysik der OeAW, Wien, Austria
W. Adam, T. Bergauer, M. Dragicevic, J. Erö, M. Friedl, R. Frühwirth[1], V.M. Ghete, C. Hartl, N. Hörmann, J. Hrubec, M. Jeitler[1], W. Kiesenhofer, V. Knünz, M. Krammer[1], I. Krätschmer, D. Liko, I. Mikulec, D. Rabady[2], B. Rahbaran, H. Rohringer, R. Schöfbeck, J. Strauss, W. Treberer-Treberspurg, W. Waltenberger, C.-E. Wulz[1]

National Centre for Particle and High Energy Physics, Minsk, Belarus
V. Mossolov, N. Shumeiko, J. Suarez Gonzalez

Universiteit Antwerpen, Antwerpen, Belgium
S. Alderweireldt, S. Bansal, T. Cornelis, E.A. De Wolf, X. Janssen, A. Knutsson, J. Lauwers, S. Luyckx, S. Ochesanu, R. Rougny, M. Van De Klundert, H. Van Haevermaet, P. Van Mechelen, N. Van Remortel, A. Van Spilbeeck

Vrije Universiteit Brussel, Brussel, Belgium
F. Blekman, S. Blyweert, J. D'Hondt, N. Daci, N. Heracleous, J. Keaveney, S. Lowette, M. Maes, A. Olbrechts, Q. Python, D. Strom, S. Tavernier, W. Van Doninck, P. Van Mulders, G.P. Van Onsem, I. Villella

Université Libre de Bruxelles, Bruxelles, Belgium
C. Caillol, B. Clerbaux, G. De Lentdecker, D. Dobur, L. Favart, A.P.R. Gay, A. Grebenyuk, A. Léonard, A. Mohammadi, L. Perniè[2], A. Randle-conde, T. Reis, T. Seva, L. Thomas, C. Vander Velde, P. Vanlaer, J. Wang, F. Zenoni

Ghent University, Ghent, Belgium
V. Adler, K. Beernaert, L. Benucci, A. Cimmino, S. Costantini, S. Crucy, A. Fagot, G. Garcia, J. Mccartin, A.A. Ocampo Rios, D. Poyraz, D. Ryckbosch, S. Salva Diblen, M. Sigamani, N. Strobbe, F. Thyssen, M. Tytgat, E. Yazgan, N. Zaganidis

Université Catholique de Louvain, Louvain-la-Neuve, Belgium
S. Basegmez, C. Beluffi[3], G. Bruno, R. Castello, A. Caudron, L. Ceard, G.G. Da Silveira, C. Delaere, T. du Pree, D. Favart, L. Forthomme, A. Giammanco[4], J. Hollar, A. Jafari, P. Jez, M. Komm, V. Lemaitre, C. Nuttens, D. Pagano, L. Perrini, A. Pin, K. Piotrzkowski, A. Popov[5], L. Quertenmont, M. Selvaggi, M. Vidal Marono, J.M. Vizan Garcia

Université de Mons, Mons, Belgium
N. Beliy, T. Caebergs, E. Daubie, G.H. Hammad

Centro Brasileiro de Pesquisas Fisicas, Rio de Janeiro, Brazil
W.L. Aldá Júnior, G.A. Alves, L. Brito, M. Correa Martins Junior, T. Dos Reis Martins, J. Molina, C. Mora Herrera, M.E. Pol, P. Rebello Teles

Universidade do Estado do Rio de Janeiro, Rio de Janeiro, Brazil
W. Carvalho, J. Chinellato[6], A. Custódio, E.M. Da Costa, D. De Jesus Damiao, C. De Oliveira Martins, S. Fonseca De Souza, H. Malbouisson, D. Matos Figueiredo, L. Mundim, H. Nogima, W.L. Prado Da Silva, J. Santaolalla, A. Santoro, A. Sznajder, E.J. Tonelli Manganote[6], A. Vilela Pereira

Universidade Estadual Paulista [a], Universidade Federal do ABC [b], São Paulo, Brazil
C.A. Bernardes[b], S. Dogra[a], T.R. Fernandez Perez Tomei[a], E.M. Gregores[b], P.G. Mercadante[b], S.F. Novaes[a], Sandra S. Padula[a]

Institute for Nuclear Research and Nuclear Energy, Sofia, Bulgaria
A. Aleksandrov, V. Genchev[2], R. Hadjiiska, P. Iaydjiev, A. Marinov, S. Piperov, M. Rodozov, S. Stoykova, G. Sultanov, M. Vutova

University of Sofia, Sofia, Bulgaria
A. Dimitrov, I. Glushkov, L. Litov, B. Pavlov, P. Petkov

Institute of High Energy Physics, Beijing, China
J.G. Bian, G.M. Chen, H.S. Chen, M. Chen, T. Cheng, R. Du, C.H. Jiang, R. Plestina[7], F. Romeo, J. Tao, Z. Wang

State Key Laboratory of Nuclear Physics and Technology, Peking University, Beijing, China
C. Asawatangtrakuldee, Y. Ban, S. Liu, Y. Mao, S.J. Qian, D. Wang, Z. Xu, L. Zhang, W. Zou

Universidad de Los Andes, Bogota, Colombia
C. Avila, A. Cabrera, L.F. Chaparro Sierra, C. Florez, J.P. Gomez, B. Gomez Moreno, J.C. Sanabria

University of Split, Faculty of Electrical Engineering, Mechanical Engineering and Naval Architecture, Split, Croatia
N. Godinovic, D. Lelas, D. Polic, I. Puljak

University of Split, Faculty of Science, Split, Croatia
Z. Antunovic, M. Kovac

Institute Rudjer Boskovic, Zagreb, Croatia
V. Brigljevic, K. Kadija, J. Luetic, D. Mekterovic, L. Sudic

University of Cyprus, Nicosia, Cyprus
A. Attikis, G. Mavromanolakis, J. Mousa, C. Nicolaou, F. Ptochos, P.A. Razis, H. Rykaczewski

Charles University, Prague, Czech Republic
M. Bodlak, M. Finger, M. Finger Jr.[8]

Academy of Scientific Research and Technology of the Arab Republic of Egypt, Egyptian Network of High Energy Physics, Cairo, Egypt
Y. Assran[9], A. Ellithi Kamel[10], M.A. Mahmoud[11], A. Radi[12,13]

National Institute of Chemical Physics and Biophysics, Tallinn, Estonia
M. Kadastik, M. Murumaa, M. Raidal, A. Tiko

Department of Physics, University of Helsinki, Helsinki, Finland
P. Eerola, M. Voutilainen

Helsinki Institute of Physics, Helsinki, Finland
J. Härkönen, V. Karimäki, R. Kinnunen, M.J. Kortelainen, T. Lampén, K. Lassila-Perini, S. Lehti, T. Lindén, P. Luukka, T. Mäenpää, T. Peltola, E. Tuominen, J. Tuominiemi, E. Tuovinen, L. Wendland

Lappeenranta University of Technology, Lappeenranta, Finland
J. Talvitie, T. Tuuva

DSM/IRFU, CEA/Saclay, Gif-sur-Yvette, France
M. Besancon, F. Couderc, M. Dejardin, D. Denegri, B. Fabbro, J.L. Faure, C. Favaro, F. Ferri, S. Ganjour, A. Givernaud, P. Gras, G. Hamel de Monchenault, P. Jarry, E. Locci, J. Malcles, J. Rander, A. Rosowsky, M. Titov

Laboratoire Leprince-Ringuet, Ecole Polytechnique, IN2P3-CNRS, Palaiseau, France
S. Baffioni, F. Beaudette, P. Busson, E. Chapon, C. Charlot, T. Dahms, M. Dalchenko, L. Dobrzynski, N. Filipovic, A. Florent, R. Granier de Cassagnac, L. Mastrolorenzo, P. Miné, I.N. Naranjo, M. Nguyen, C. Ochando, G. Ortona, P. Paganini, S. Regnard, R. Salerno, J.B. Sauvan, Y. Sirois, C. Veelken, Y. Yilmaz, A. Zabi

Institut Pluridisciplinaire Hubert Curien, Université de Strasbourg, Université de Haute Alsace Mulhouse, CNRS/IN2P3, Strasbourg, France
J.-L. Agram[14], J. Andrea, A. Aubin, D. Bloch, J.-M. Brom, E.C. Chabert, C. Collard, E. Conte[14], J.-C. Fontaine[14], D. Gelé, U. Goerlach, C. Goetzmann, A.-C. Le Bihan, K. Skovpen, P. Van Hove

Centre de Calcul de l'Institut National de Physique Nucleaire et de Physique des Particules, CNRS/IN2P3, Villeurbanne, France
S. Gadrat

Université de Lyon, Université Claude Bernard Lyon 1, CNRS-IN2P3, Institut de Physique Nucléaire de Lyon, Villeurbanne, France
S. Beauceron, N. Beaupere, C. Bernet[7], G. Boudoul[2], E. Bouvier, S. Brochet, C.A. Carrillo Montoya, J. Chasserat, R. Chierici, D. Contardo[2], B. Courbon, P. Depasse, H. El Mamouni, J. Fan, J. Fay, S. Gascon, M. Gouzevitch, B. Ille, T. Kurca, M. Lethuillier, L. Mirabito, A.L. Pequegnot, S. Perries, J.D. Ruiz Alvarez, D. Sabes, L. Sgandurra, V. Sordini, M. Vander Donckt, P. Verdier, S. Viret, H. Xiao

Institute of High Energy Physics and Informatization, Tbilisi State University, Tbilisi, Georgia
Z. Tsamalaidze[8]

RWTH Aachen University, I. Physikalisches Institut, Aachen, Germany
C. Autermann, S. Beranek, M. Bontenackels, M. Edelhoff, L. Feld, A. Heister, K. Klein, M. Lipinski, A. Ostapchuk, M. Preuten, F. Raupach, J. Sammet, S. Schael, J.F. Schulte, H. Weber, B. Wittmer, V. Zhukov[5]

RWTH Aachen University, III. Physikalisches Institut A, Aachen, Germany
M. Ata, M. Brodski, E. Dietz-Laursonn, D. Duchardt, M. Erdmann, R. Fischer, A. Güth, T. Hebbeker, C. Heidemann, K. Hoepfner, D. Klingebiel, S. Knutzen, P. Kreuzer, M. Merschmeyer, A. Meyer, P. Millet, M. Olschewski, K. Padeken, P. Papacz, H. Reithler, S.A. Schmitz, L. Sonnenschein, D. Teyssier, S. Thüer

RWTH Aachen University, III. Physikalisches Institut B, Aachen, Germany
V. Cherepanov, Y. Erdogan, G. Flügge, H. Geenen, M. Geisler, W. Haj Ahmad, F. Hoehle, B. Kargoll, T. Kress, Y. Kuessel, A. Künsken, J. Lingemann[2], A. Nowack, I.M. Nugent, C. Pistone, O. Pooth, A. Stahl

Deutsches Elektronen-Synchrotron, Hamburg, Germany
M. Aldaya Martin, I. Asin, N. Bartosik, J. Behr, U. Behrens, A.J. Bell, A. Bethani, K. Borras, A. Burgmeier, A. Cakir, L. Calligaris, A. Campbell, S. Choudhury, F. Costanza, C. Diez Pardos, G. Dolinska, S. Dooling, T. Dorland, G. Eckerlin, D. Eckstein, T. Eichhorn, G. Flucke, J. Garay Garcia, A. Geiser, A. Gizhko, P. Gunnellini, J. Hauk, M. Hempel[15], H. Jung, A. Kalogeropoulos, O. Karacheban[15], M. Kasemann, P. Katsas, J. Kieseler, C. Kleinwort, I. Korol,

D. Krücker, W. Lange, J. Leonard, K. Lipka, A. Lobanov, W. Lohmann[15], B. Lutz, R. Mankel, I. Marfin[15], I.-A. Melzer-Pellmann, A.B. Meyer, G. Mittag, J. Mnich, A. Mussgiller, S. Naumann-Emme, A. Nayak, E. Ntomari, H. Perrey, D. Pitzl, R. Placakyte, A. Raspereza, P.M. Ribeiro Cipriano, B. Roland, E. Ron, M.Ö. Sahin, J. Salfeld-Nebgen, P. Saxena, T. Schoerner-Sadenius, M. Schröder, C. Seitz, S. Spannagel, A.D.R. Vargas Trevino, R. Walsh, C. Wissing

University of Hamburg, Hamburg, Germany
V. Blobel, M. Centis Vignali, A.R. Draeger, J. Erfle, E. Garutti, K. Goebel, M. Görner, J. Haller, M. Hoffmann, R.S. Höing, A. Junkes, H. Kirschenmann, R. Klanner, R. Kogler, T. Lapsien, T. Lenz, I. Marchesini, D. Marconi, J. Ott, T. Peiffer, A. Perieanu, N. Pietsch, J. Poehlsen, T. Poehlsen, D. Rathjens, C. Sander, H. Schettler, P. Schleper, E. Schlieckau, A. Schmidt, M. Seidel, V. Sola, H. Stadie, G. Steinbrück, D. Troendle, E. Usai, L. Vanelderen, A. Vanhoefer

Institut für Experimentelle Kernphysik, Karlsruhe, Germany
C. Barth, C. Baus, J. Berger, C. Böser, E. Butz, T. Chwalek, W. De Boer, A. Descroix, A. Dierlamm, M. Feindt, F. Frensch, M. Giffels, A. Gilbert, F. Hartmann[2], T. Hauth, U. Husemann, I. Katkov[5], A. Kornmayer[2], P. Lobelle Pardo, M.U. Mozer, T. Müller, Th. Müller, A. Nürnberg, G. Quast, K. Rabbertz, S. Röcker, H.J. Simonis, F.M. Stober, R. Ulrich, J. Wagner-Kuhr, S. Wayand, T. Weiler, R. Wolf

Institute of Nuclear and Particle Physics (INPP), NCSR Demokritos, Aghia Paraskevi, Greece
G. Anagnostou, G. Daskalakis, T. Geralis, V.A. Giakoumopoulou, A. Kyriakis, D. Loukas, A. Markou, C. Markou, A. Psallidas, I. Topsis-Giotis

University of Athens, Athens, Greece
A. Agapitos, S. Kesisoglou, A. Panagiotou, N. Saoulidou, E. Stiliaris, E. Tziaferi

University of Ioánnina, Ioánnina, Greece
X. Aslanoglou, I. Evangelou, G. Flouris, C. Foudas, P. Kokkas, N. Manthos, I. Papadopoulos, E. Paradas, J. Strologas

Wigner Research Centre for Physics, Budapest, Hungary
G. Bencze, C. Hajdu, P. Hidas, D. Horvath[16], F. Sikler, V. Veszpremi, G. Vesztergombi[17], A.J. Zsigmond

Institute of Nuclear Research ATOMKI, Debrecen, Hungary
N. Beni, S. Czellar, J. Karancsi[18], J. Molnar, J. Palinkas, Z. Szillasi

University of Debrecen, Debrecen, Hungary
A. Makovec, P. Raics, Z.L. Trocsanyi, B. Ujvari

National Institute of Science Education and Research, Bhubaneswar, India
S.K. Swain

Panjab University, Chandigarh, India
S.B. Beri, V. Bhatnagar, R. Gupta, U.Bhawandeep, A.K. Kalsi, M. Kaur, R. Kumar, M. Mittal, N. Nishu, J.B. Singh

University of Delhi, Delhi, India
Ashok Kumar, Arun Kumar, S. Ahuja, A. Bhardwaj, B.C. Choudhary, A. Kumar, S. Malhotra, M. Naimuddin, K. Ranjan, V. Sharma

Saha Institute of Nuclear Physics, Kolkata, India
S. Banerjee, S. Bhattacharya, K. Chatterjee, S. Dutta, B. Gomber, Sa. Jain, Sh. Jain, R. Khurana, A. Modak, S. Mukherjee, D. Roy, S. Sarkar, M. Sharan

Bhabha Atomic Research Centre, Mumbai, India
A. Abdulsalam, D. Dutta, V. Kumar, A.K. Mohanty[2], L.M. Pant, P. Shukla, A. Topkar

Tata Institute of Fundamental Research, Mumbai, India
T. Aziz, S. Banerjee, S. Bhowmik[19], R.M. Chatterjee, R.K. Dewanjee, S. Dugad, S. Ganguly, S. Ghosh, M. Guchait, A. Gurtu[20], G. Kole, S. Kumar, M. Maity[19], G. Majumder, K. Mazumdar, G.B. Mohanty, B. Parida, K. Sudhakar, N. Wickramage[21]

Indian Institute of Science Education and Research (IISER), Pune, India
S. Sharma

Institute for Research in Fundamental Sciences (IPM), Tehran, Iran
H. Bakhshiansohi, H. Behnamian, S.M. Etesami[22], A. Fahim[23], R. Goldouzian, M. Khakzad, M. Mohammadi Najafabadi, M. Naseri, S. Paktinat Mehdiabadi, F. Rezaei Hosseinabadi, B. Safarzadeh[24], M. Zeinali

University College Dublin, Dublin, Ireland
M. Felcini, M. Grunewald

INFN Sezione di Bari [a], Università di Bari [b], Politecnico di Bari [c], Bari, Italy
M. Abbrescia[a,b], C. Calabria[a,b], S.S. Chhibra[a,b], A. Colaleo[a], D. Creanza[a,c], L. Cristella[a,b], N. De Filippis[a,c], M. De Palma[a,b], L. Fiore[a], G. Iaselli[a,c], G. Maggi[a,c], M. Maggi[a], S. My[a,c], S. Nuzzo[a,b], A. Pompili[a,b], G. Pugliese[a,c], R. Radogna[a,b,2], G. Selvaggi[a,b], A. Sharma[a], L. Silvestris[a,2], R. Venditti[a,b], P. Verwilligen[a]

INFN Sezione di Bologna [a], Università di Bologna [b], Bologna, Italy
G. Abbiendi[a], A.C. Benvenuti[a], D. Bonacorsi[a,b], S. Braibant-Giacomelli[a,b], L. Brigliadori[a,b], R. Campanini[a,b], P. Capiluppi[a,b], A. Castro[a,b], F.R. Cavallo[a], G. Codispoti[a,b], M. Cuffiani[a,b], G.M. Dallavalle[a], F. Fabbri[a], A. Fanfani[a,b], D. Fasanella[a,b], P. Giacomelli[a], C. Grandi[a], L. Guiducci[a,b], S. Marcellini[a], G. Masetti[a], A. Montanari[a], F.L. Navarria[a,b], A. Perrotta[a], A.M. Rossi[a,b], T. Rovelli[a,b], G.P. Siroli[a,b], N. Tosi[a,b], R. Travaglini[a,b]

INFN Sezione di Catania [a], Università di Catania [b], CSFNSM [c], Catania, Italy
S. Albergo[a,b], G. Cappello[a], M. Chiorboli[a,b], S. Costa[a,b], F. Giordano[a,2], R. Potenza[a,b], A. Tricomi[a,b], C. Tuve[a,b]

INFN Sezione di Firenze [a], Università di Firenze [b], Firenze, Italy
G. Barbagli[a], V. Ciulli[a,b], C. Civinini[a], R. D'Alessandro[a,b], E. Focardi[a,b], E. Gallo[a], S. Gonzi[a,b], V. Gori[a,b], P. Lenzi[a,b], M. Meschini[a], S. Paoletti[a], G. Sguazzoni[a], A. Tropiano[a,b]

INFN Laboratori Nazionali di Frascati, Frascati, Italy
L. Benussi, S. Bianco, F. Fabbri, D. Piccolo

INFN Sezione di Genova [a], Università di Genova [b], Genova, Italy
R. Ferretti[a,b], F. Ferro[a], M. Lo Vetere[a,b], E. Robutti[a], S. Tosi[a,b]

INFN Sezione di Milano-Bicocca [a], Università di Milano-Bicocca [b], Milano, Italy
M.E. Dinardo[a,b], S. Fiorendi[a,b], S. Gennai[a,2], R. Gerosa[a,b,2], A. Ghezzi[a,b], P. Govoni[a,b], M.T. Lucchini[a,b,2], S. Malvezzi[a], R.A. Manzoni[a,b], A. Martelli[a,b], B. Marzocchi[a,b,2], D. Menasce[a], L. Moroni[a], M. Paganoni[a,b], D. Pedrini[a], S. Ragazzi[a,b], N. Redaelli[a], T. Tabarelli de Fatis[a,b]

INFN Sezione di Napoli [a], Università di Napoli 'Federico II' [b], Università della Basilicata (Potenza) [c], Università G. Marconi (Roma) [d], Napoli, Italy
S. Buontempo[a], N. Cavallo[a,c], S. Di Guida[a,d,2], F. Fabozzi[a,c], A.O.M. Iorio[a,b], L. Lista[a], S. Meola[a,d,2], M. Merola[a], P. Paolucci[a,2]

INFN Sezione di Padova [a], Università di Padova [b], Università di Trento (Trento) [c], Padova, Italy
P. Azzi[a], N. Bacchetta[a], M. Bellato[a], D. Bisello[a,b], R. Carlin[a,b], P. Checchia[a], M. Dall'Osso[a,b], T. Dorigo[a], S. Fantinel[a], F. Fanzago[a], F. Gasparini[a,b], U. Gasparini[a,b], F. Gonella[a], A. Gozzelino[a], S. Lacaprara[a], F. Montecassiano[a], J. Pazzini[a,b], M. Pegoraro[a], N. Pozzobon[a,b], P. Ronchese[a,b], M. Sgaravatto[a], M. Tosi[a,b], S. Ventura[a], A. Zucchetta[a,b], G. Zumerle[a,b]

INFN Sezione di Pavia [a], Università di Pavia [b], Pavia, Italy
M. Gabusi[a,b], S.P. Ratti[a,b], V. Re[a], C. Riccardi[a,b], P. Salvini[a], P. Vitulo[a,b]

INFN Sezione di Perugia [a], Università di Perugia [b], Perugia, Italy
M. Biasini[a,b], G.M. Bilei[a], D. Ciangottini[a,b,2], L. Fanò[a,b], P. Lariccia[a,b], G. Mantovani[a,b], M. Menichelli[a], A. Saha[a], A. Santocchia[a,b], A. Spiezia[a,b,2]

INFN Sezione di Pisa [a], Università di Pisa [b], Scuola Normale Superiore di Pisa [c], Pisa, Italy
K. Androsov[a,25], P. Azzurri[a], G. Bagliesi[a], J. Bernardini[a], T. Boccali[a], G. Broccolo[a,c], R. Castaldi[a], M.A. Ciocci[a,25], R. Dell'Orso[a], S. Donato[a,c,2], G. Fedi, F. Fiori[a,c], L. Foà[a,c], A. Giassi[a], M.T. Grippo[a,25], F. Ligabue[a,c], T. Lomtadze[a], L. Martini[a,b], A. Messineo[a,b], C.S. Moon[a,26], F. Palla[a,2], A. Rizzi[a,b], A. Savoy-Navarro[a,27], A.T. Serban[a], P. Spagnolo[a], P. Squillacioti[a,25], R. Tenchini[a], G. Tonelli[a,b], A. Venturi[a], P.G. Verdini[a], C. Vernieri[a,c]

INFN Sezione di Roma [a], Università di Roma [b], Roma, Italy
L. Barone[a,b], F. Cavallari[a], G. D'imperio[a,b], D. Del Re[a,b], M. Diemoz[a], C. Jorda[a], E. Longo[a,b], F. Margaroli[a,b], P. Meridiani[a], F. Micheli[a,b,2], G. Organtini[a,b], R. Paramatti[a], S. Rahatlou[a,b], C. Rovelli[a], F. Santanastasio[a,b], L. Soffi[a,b], P. Traczyk[a,b,2]

INFN Sezione di Torino [a], Università di Torino [b], Università del Piemonte Orientale (Novara) [c], Torino, Italy
N. Amapane[a,b], R. Arcidiacono[a,c], S. Argiro[a,b], M. Arneodo[a,c], R. Bellan[a,b], C. Biino[a], N. Cartiglia[a], S. Casasso[a,b,2], M. Costa[a,b], R. Covarelli, A. Degano[a,b], N. Demaria[a], L. Finco[a,b,2], C. Mariotti[a], S. Maselli[a], E. Migliore[a,b], V. Monaco[a,b], M. Musich[a], M.M. Obertino[a,c], L. Pacher[a,b], N. Pastrone[a], M. Pelliccioni[a], G.L. Pinna Angioni[a,b], A. Romero[a,b], M. Ruspa[a,c], R. Sacchi[a,b], A. Solano[a,b], A. Staiano[a], U. Tamponi[a], P.P. Trapani[a,b]

INFN Sezione di Trieste [a], Università di Trieste [b], Trieste, Italy
S. Belforte[a], V. Candelise[a,b,2], M. Casarsa[a], F. Cossutti[a], G. Della Ricca[a,b], B. Gobbo[a], C. La Licata[a,b], M. Marone[a,b], A. Schizzi[a,b], T. Umer[a,b], A. Zanetti[a]

Kangwon National University, Chunchon, Korea
S. Chang, A. Kropivnitskaya, S.K. Nam

Kyungpook National University, Daegu, Korea
D.H. Kim, G.N. Kim, M.S. Kim, D.J. Kong, S. Lee, Y.D. Oh, H. Park, A. Sakharov, D.C. Son

Chonbuk National University, Jeonju, Korea
T.J. Kim, M.S. Ryu

Chonnam National University, Institute for Universe and Elementary Particles, Kwangju, Korea
J.Y. Kim, D.H. Moon, S. Song

Korea University, Seoul, Korea
S. Choi, D. Gyun, B. Hong, M. Jo, H. Kim, Y. Kim, B. Lee, K.S. Lee, S.K. Park, Y. Roh

Seoul National University, Seoul, Korea
H.D. Yoo

University of Seoul, Seoul, Korea
M. Choi, J.H. Kim, I.C. Park, G. Ryu

Sungkyunkwan University, Suwon, Korea
Y. Choi, Y.K. Choi, J. Goh, D. Kim, E. Kwon, J. Lee, I. Yu

Vilnius University, Vilnius, Lithuania
A. Juodagalvis

National Centre for Particle Physics, Universiti Malaya, Kuala Lumpur, Malaysia
J.R. Komaragiri, M.A.B. Md Ali, W.A.T. Wan Abdullah

Centro de Investigacion y de Estudios Avanzados del IPN, Mexico City, Mexico
E. Casimiro Linares, H. Castilla-Valdez, E. De La Cruz-Burelo, I. Heredia-de La Cruz, A. Hernandez-Almada, R. Lopez-Fernandez, A. Sanchez-Hernandez

Universidad Iberoamericana, Mexico City, Mexico
S. Carrillo Moreno, F. Vazquez Valencia

Benemerita Universidad Autonoma de Puebla, Puebla, Mexico
I. Pedraza, H.A. Salazar Ibarguen

Universidad Autónoma de San Luis Potosí, San Luis Potosí, Mexico
A. Morelos Pineda

University of Auckland, Auckland, New Zealand
D. Krofcheck

University of Canterbury, Christchurch, New Zealand
P.H. Butler, S. Reucroft

National Centre for Physics, Quaid-I-Azam University, Islamabad, Pakistan
A. Ahmad, M. Ahmad, Q. Hassan, H.R. Hoorani, W.A. Khan, T. Khurshid, M. Shoaib

National Centre for Nuclear Research, Swierk, Poland
H. Bialkowska, M. Bluj, B. Boimska, T. Frueboes, M. Górski, M. Kazana, K. Nawrocki, K. Romanowska-Rybinska, M. Szleper, P. Zalewski

Institute of Experimental Physics, Faculty of Physics, University of Warsaw, Warsaw, Poland
G. Brona, K. Bunkowski, M. Cwiok, W. Dominik, K. Doroba, A. Kalinowski, M. Konecki, J. Krolikowski, M. Misiura, M. Olszewski

Laboratório de Instrumentação e Física Experimental de Partículas, Lisboa, Portugal
P. Bargassa, C. Beirão Da Cruz E Silva, P. Faccioli, P.G. Ferreira Parracho, M. Gallinaro, L. Lloret Iglesias, F. Nguyen, J. Rodrigues Antunes, J. Seixas, J. Varela, P. Vischia

Joint Institute for Nuclear Research, Dubna, Russia
S. Afanasiev, P. Bunin, M. Gavrilenko, I. Golutvin, I. Gorbunov, A. Kamenev, V. Karjavin, V. Konoplyanikov, A. Lanev, A. Malakhov, V. Matveev[28], P. Moisenz, V. Palichik, V. Perelygin, S. Shmatov, N. Skatchkov, V. Smirnov, A. Zarubin

Petersburg Nuclear Physics Institute, Gatchina (St. Petersburg), Russia
V. Golovtsov, Y. Ivanov, V. Kim[29], E. Kuznetsova, P. Levchenko, V. Murzin, V. Oreshkin, I. Smirnov, V. Sulimov, L. Uvarov, S. Vavilov, A. Vorobyev, An. Vorobyev

Institute for Nuclear Research, Moscow, Russia
Yu. Andreev, A. Dermenev, S. Gninenko, N. Golubev, M. Kirsanov, N. Krasnikov, A. Pashenkov, D. Tlisov, A. Toropin

Institute for Theoretical and Experimental Physics, Moscow, Russia
V. Epshteyn, V. Gavrilov, N. Lychkovskaya, V. Popov, I. Pozdnyakov, G. Safronov, S. Semenov, A. Spiridonov, V. Stolin, E. Vlasov, A. Zhokin

P.N. Lebedev Physical Institute, Moscow, Russia
V. Andreev, M. Azarkin[30], I. Dremin[30], M. Kirakosyan, A. Leonidov[30], G. Mesyats, S.V. Rusakov, A. Vinogradov

Skobeltsyn Institute of Nuclear Physics, Lomonosov Moscow State University, Moscow, Russia
A. Belyaev, E. Boos, M. Dubinin[31], L. Dudko, A. Ershov, A. Gribushin, A. Kaminskiy[32], V. Klyukhin, O. Kodolova, I. Lokhtin, S. Obraztsov, S. Petrushanko, V. Savrin

State Research Center of Russian Federation, Institute for High Energy Physics, Protvino, Russia
I. Azhgirey, I. Bayshev, S. Bitioukov, V. Kachanov, A. Kalinin, D. Konstantinov, V. Krychkine, V. Petrov, R. Ryutin, A. Sobol, L. Tourtchanovitch, S. Troshin, N. Tyurin, A. Uzunian, A. Volkov

University of Belgrade, Faculty of Physics and Vinca Institute of Nuclear Sciences, Belgrade, Serbia
P. Adzic[33], M. Ekmedzic, J. Milosevic, V. Rekovic

Centro de Investigaciones Energéticas Medioambientales y Tecnológicas (CIEMAT), Madrid, Spain
J. Alcaraz Maestre, C. Battilana, E. Calvo, M. Cerrada, M. Chamizo Llatas, N. Colino, B. De La Cruz, A. Delgado Peris, D. Domínguez Vázquez, A. Escalante Del Valle, C. Fernandez Bedoya, J.P. Fernández Ramos, J. Flix, M.C. Fouz, P. Garcia-Abia, O. Gonzalez Lopez, S. Goy Lopez, J.M. Hernandez, M.I. Josa, E. Navarro De Martino, A. Pérez-Calero Yzquierdo, J. Puerta Pelayo, A. Quintario Olmeda, I. Redondo, L. Romero, M.S. Soares

Universidad Autónoma de Madrid, Madrid, Spain
C. Albajar, J.F. de Trocóniz, M. Missiroli, D. Moran

Universidad de Oviedo, Oviedo, Spain
H. Brun, J. Cuevas, J. Fernandez Menendez, S. Folgueras, I. Gonzalez Caballero

Instituto de Física de Cantabria (IFCA), CSIC-Universidad de Cantabria, Santander, Spain
J.A. Brochero Cifuentes, I.J. Cabrillo, A. Calderon, J. Duarte Campderros, M. Fernandez, G. Gomez, A. Graziano, A. Lopez Virto, J. Marco, R. Marco, C. Martinez Rivero, F. Matorras, F.J. Munoz Sanchez, J. Piedra Gomez, T. Rodrigo, A.Y. Rodríguez-Marrero, A. Ruiz-Jimeno, L. Scodellaro, I. Vila, R. Vilar Cortabitarte

CERN, European Organization for Nuclear Research, Geneva, Switzerland
D. Abbaneo, E. Auffray, G. Auzinger, M. Bachtis, P. Baillon, A.H. Ball, D. Barney, A. Benaglia, J. Bendavid, L. Benhabib, J.F. Benitez, P. Bloch, A. Bocci, A. Bonato, O. Bondu, C. Botta, H. Breuker, T. Camporesi, G. Cerminara, S. Colafranceschi[34], M. D'Alfonso, D. d'Enterria, A. Dabrowski, A. David, F. De Guio, A. De Roeck, S. De Visscher, E. Di Marco, M. Dobson,

M. Dordevic, B. Dorney, N. Dupont-Sagorin, A. Elliott-Peisert, G. Franzoni, W. Funk, D. Gigi, K. Gill, D. Giordano, M. Girone, F. Glege, R. Guida, S. Gundacker, M. Guthoff, J. Hammer, M. Hansen, P. Harris, J. Hegeman, V. Innocente, P. Janot, K. Kousouris, K. Krajczar, P. Lecoq, C. Lourenço, N. Magini, L. Malgeri, M. Mannelli, J. Marrouche, L. Masetti, F. Meijers, S. Mersi, E. Meschi, F. Moortgat, S. Morovic, M. Mulders, L. Orsini, L. Pape, E. Perez, A. Petrilli, G. Petrucciani, A. Pfeiffer, M. Pimiä, D. Piparo, M. Plagge, A. Racz, G. Rolandi[35], M. Rovere, H. Sakulin, C. Schäfer, C. Schwick, A. Sharma, P. Siegrist, P. Silva, M. Simon, P. Sphicas[36], D. Spiga, J. Steggemann, B. Stieger, M. Stoye, Y. Takahashi, D. Treille, A. Tsirou, G.I. Veres[17], N. Wardle, H.K. Wöhri, H. Wollny, W.D. Zeuner

Paul Scherrer Institut, Villigen, Switzerland
W. Bertl, K. Deiters, W. Erdmann, R. Horisberger, Q. Ingram, H.C. Kaestli, D. Kotlinski, U. Langenegger, D. Renker, T. Rohe

Institute for Particle Physics, ETH Zurich, Zurich, Switzerland
F. Bachmair, L. Bäni, L. Bianchini, M.A. Buchmann, B. Casal, N. Chanon, G. Dissertori, M. Dittmar, M. Donegà, M. Dünser, P. Eller, C. Grab, D. Hits, J. Hoss, G. Kasieczka, W. Lustermann, B. Mangano, A.C. Marini, M. Marionneau, P. Martinez Ruiz del Arbol, M. Masciovecchio, D. Meister, N. Mohr, P. Musella, C. Nägeli[37], F. Nessi-Tedaldi, F. Pandolfi, F. Pauss, L. Perrozzi, M. Peruzzi, M. Quittnat, L. Rebane, M. Rossini, A. Starodumov[38], M. Takahashi, K. Theofilatos, R. Wallny, H.A. Weber

Universität Zürich, Zurich, Switzerland
C. Amsler[39], M.F. Canelli, V. Chiochia, A. De Cosa, A. Hinzmann, T. Hreus, B. Kilminster, C. Lange, J. Ngadiuba, D. Pinna, P. Robmann, F.J. Ronga, S. Taroni, Y. Yang

National Central University, Chung-Li, Taiwan
M. Cardaci, K.H. Chen, C. Ferro, C.M. Kuo, W. Lin, Y.J. Lu, R. Volpe, S.S. Yu

National Taiwan University (NTU), Taipei, Taiwan
P. Chang, Y.H. Chang, Y. Chao, K.F. Chen, P.H. Chen, C. Dietz, U. Grundler, W.-S. Hou, Y.F. Liu, R.-S. Lu, M. Miñano Moya, E. Petrakou, Y.M. Tzeng, R. Wilken

Chulalongkorn University, Faculty of Science, Department of Physics, Bangkok, Thailand
B. Asavapibhop, G. Singh, N. Srimanobhas, N. Suwonjandee

Cukurova University, Adana, Turkey
A. Adiguzel, M.N. Bakirci[40], S. Cerci[41], C. Dozen, I. Dumanoglu, E. Eskut, S. Girgis, G. Gokbulut, Y. Guler, E. Gurpinar, I. Hos, E.E. Kangal[42], A. Kayis Topaksu, G. Onengut[43], K. Ozdemir[44], S. Ozturk[40], A. Polatoz, D. Sunar Cerci[41], B. Tali[41], H. Topakli[40], M. Vergili, C. Zorbilmez

Middle East Technical University, Physics Department, Ankara, Turkey
I.V. Akin, B. Bilin, S. Bilmis, H. Gamsizkan[45], B. Isildak[46], G. Karapinar[47], K. Ocalan[48], S. Sekmen, U.E. Surat, M. Yalvac, M. Zeyrek

Bogazici University, Istanbul, Turkey
E.A. Albayrak[49], E. Gülmez, M. Kaya[50], O. Kaya[51], T. Yetkin[52]

Istanbul Technical University, Istanbul, Turkey
K. Cankocak, F.I. Vardarlı

National Scientific Center, Kharkov Institute of Physics and Technology, Kharkov, Ukraine
L. Levchuk, P. Sorokin

University of Bristol, Bristol, United Kingdom
J.J. Brooke, E. Clement, D. Cussans, H. Flacher, J. Goldstein, M. Grimes, G.P. Heath, H.F. Heath, J. Jacob, L. Kreczko, C. Lucas, Z. Meng, D.M. Newbold[53], S. Paramesvaran, A. Poll, T. Sakuma, S. Seif El Nasr-storey, S. Senkin, V.J. Smith

Rutherford Appleton Laboratory, Didcot, United Kingdom
K.W. Bell, A. Belyaev[54], C. Brew, R.M. Brown, D.J.A. Cockerill, J.A. Coughlan, K. Harder, S. Harper, E. Olaiya, D. Petyt, C.H. Shepherd-Themistocleous, A. Thea, I.R. Tomalin, T. Williams, W.J. Womersley, S.D. Worm

Imperial College, London, United Kingdom
M. Baber, R. Bainbridge, O. Buchmuller, D. Burton, D. Colling, N. Cripps, P. Dauncey, G. Davies, M. Della Negra, P. Dunne, A. Elwood, W. Ferguson, J. Fulcher, D. Futyan, G. Hall, G. Iles, M. Jarvis, G. Karapostoli, M. Kenzie, R. Lane, R. Lucas[53], L. Lyons, A.-M. Magnan, S. Malik, B. Mathias, J. Nash, A. Nikitenko[38], J. Pela, M. Pesaresi, K. Petridis, D.M. Raymond, S. Rogerson, A. Rose, C. Seez, P. Sharp[†], A. Tapper, M. Vazquez Acosta, T. Virdee, S.C. Zenz

Brunel University, Uxbridge, United Kingdom
J.E. Cole, P.R. Hobson, A. Khan, P. Kyberd, D. Leggat, D. Leslie, I.D. Reid, P. Symonds, L. Teodorescu, M. Turner

Baylor University, Waco, USA
J. Dittmann, K. Hatakeyama, A. Kasmi, H. Liu, N. Pastika, T. Scarborough, Z. Wu

The University of Alabama, Tuscaloosa, USA
O. Charaf, S.I. Cooper, C. Henderson, P. Rumerio

Boston University, Boston, USA
A. Avetisyan, T. Bose, C. Fantasia, P. Lawson, C. Richardson, J. Rohlf, J. St. John, L. Sulak

Brown University, Providence, USA
J. Alimena, E. Berry, S. Bhattacharya, G. Christopher, D. Cutts, Z. Demiragli, N. Dhingra, A. Ferapontov, A. Garabedian, U. Heintz, E. Laird, G. Landsberg, M. Narain, S. Sagir, T. Sinthuprasith, T. Speer, J. Swanson

University of California, Davis, Davis, USA
R. Breedon, G. Breto, M. Calderon De La Barca Sanchez, S. Chauhan, M. Chertok, J. Conway, R. Conway, P.T. Cox, R. Erbacher, M. Gardner, W. Ko, R. Lander, M. Mulhearn, D. Pellett, J. Pilot, F. Ricci-Tam, S. Shalhout, J. Smith, M. Squires, D. Stolp, M. Tripathi, S. Wilbur, R. Yohay

University of California, Los Angeles, USA
R. Cousins, P. Everaerts, C. Farrell, J. Hauser, M. Ignatenko, G. Rakness, E. Takasugi, V. Valuev, M. Weber

University of California, Riverside, Riverside, USA
K. Burt, R. Clare, J. Ellison, J.W. Gary, G. Hanson, J. Heilman, M. Ivova Rikova, P. Jandir, E. Kennedy, F. Lacroix, O.R. Long, A. Luthra, M. Malberti, M. Olmedo Negrete, A. Shrinivas, S. Sumowidagdo, S. Wimpenny

University of California, San Diego, La Jolla, USA
J.G. Branson, G.B. Cerati, S. Cittolin, R.T. D'Agnolo, A. Holzner, R. Kelley, D. Klein, J. Letts, I. Macneill, D. Olivito, S. Padhi, C. Palmer, M. Pieri, M. Sani, V. Sharma, S. Simon, M. Tadel, Y. Tu, A. Vartak, C. Welke, F. Würthwein, A. Yagil, G. Zevi Della Porta

University of California, Santa Barbara, Santa Barbara, USA
D. Barge, J. Bradmiller-Feld, C. Campagnari, T. Danielson, A. Dishaw, V. Dutta, K. Flowers, M. Franco Sevilla, P. Geffert, C. George, F. Golf, L. Gouskos, J. Incandela, C. Justus, N. Mccoll, S.D. Mullin, J. Richman, D. Stuart, W. To, C. West, J. Yoo

California Institute of Technology, Pasadena, USA
A. Apresyan, A. Bornheim, J. Bunn, Y. Chen, J. Duarte, A. Mott, H.B. Newman, C. Pena, M. Pierini, M. Spiropulu, J.R. Vlimant, R. Wilkinson, S. Xie, R.Y. Zhu

Carnegie Mellon University, Pittsburgh, USA
V. Azzolini, A. Calamba, B. Carlson, T. Ferguson, Y. Iiyama, M. Paulini, J. Russ, H. Vogel, I. Vorobiev

University of Colorado at Boulder, Boulder, USA
J.P. Cumalat, W.T. Ford, A. Gaz, M. Krohn, E. Luiggi Lopez, U. Nauenberg, J.G. Smith, K. Stenson, S.R. Wagner

Cornell University, Ithaca, USA
J. Alexander, A. Chatterjee, J. Chaves, J. Chu, S. Dittmer, N. Eggert, N. Mirman, G. Nicolas Kaufman, J.R. Patterson, A. Ryd, E. Salvati, L. Skinnari, W. Sun, W.D. Teo, J. Thom, J. Thompson, J. Tucker, Y. Weng, L. Winstrom, P. Wittich

Fairfield University, Fairfield, USA
D. Winn

Fermi National Accelerator Laboratory, Batavia, USA
S. Abdullin, M. Albrow, J. Anderson, G. Apollinari, L.A.T. Bauerdick, A. Beretvas, J. Berryhill, P.C. Bhat, G. Bolla, K. Burkett, J.N. Butler, H.W.K. Cheung, F. Chlebana, S. Cihangir, V.D. Elvira, I. Fisk, J. Freeman, E. Gottschalk, L. Gray, D. Green, S. Grünendahl, O. Gutsche, J. Hanlon, D. Hare, R.M. Harris, J. Hirschauer, B. Hooberman, S. Jindariani, M. Johnson, U. Joshi, B. Klima, B. Kreis, S. Kwan[†], J. Linacre, D. Lincoln, R. Lipton, T. Liu, R. Lopes De Sá, J. Lykken, K. Maeshima, J.M. Marraffino, V.I. Martinez Outschoorn, S. Maruyama, D. Mason, P. McBride, P. Merkel, K. Mishra, S. Mrenna, S. Nahn, C. Newman-Holmes, V. O'Dell, O. Prokofyev, E. Sexton-Kennedy, A. Soha, W.J. Spalding, L. Spiegel, L. Taylor, S. Tkaczyk, N.V. Tran, L. Uplegger, E.W. Vaandering, R. Vidal, A. Whitbeck, J. Whitmore, F. Yang

University of Florida, Gainesville, USA
D. Acosta, P. Avery, P. Bortignon, D. Bourilkov, M. Carver, D. Curry, S. Das, M. De Gruttola, G.P. Di Giovanni, R.D. Field, M. Fisher, I.K. Furic, J. Hugon, J. Konigsberg, A. Korytov, T. Kypreos, J.F. Low, K. Matchev, H. Mei, P. Milenovic[55], G. Mitselmakher, L. Muniz, A. Rinkevicius, L. Shchutska, M. Snowball, D. Sperka, J. Yelton, M. Zakaria

Florida International University, Miami, USA
S. Hewamanage, S. Linn, P. Markowitz, G. Martinez, J.L. Rodriguez

Florida State University, Tallahassee, USA
J.R. Adams, T. Adams, A. Askew, J. Bochenek, B. Diamond, J. Haas, S. Hagopian, V. Hagopian, K.F. Johnson, H. Prosper, V. Veeraraghavan, M. Weinberg

Florida Institute of Technology, Melbourne, USA
M.M. Baarmand, M. Hohlmann, H. Kalakhety, F. Yumiceva

University of Illinois at Chicago (UIC), Chicago, USA
M.R. Adams, L. Apanasevich, D. Berry, R.R. Betts, I. Bucinskaite, R. Cavanaugh, O. Evdokimov,

L. Gauthier, C.E. Gerber, D.J. Hofman, P. Kurt, C. O'Brien, I.D. Sandoval Gonzalez, C. Silkworth, P. Turner, N. Varelas

The University of Iowa, Iowa City, USA
B. Bilki[56], W. Clarida, K. Dilsiz, M. Haytmyradov, J.-P. Merlo, H. Mermerkaya[57], A. Mestvirishvili, A. Moeller, J. Nachtman, H. Ogul, Y. Onel, F. Ozok[49], A. Penzo, R. Rahmat, S. Sen, P. Tan, E. Tiras, J. Wetzel, K. Yi

Johns Hopkins University, Baltimore, USA
I. Anderson, B.A. Barnett, B. Blumenfeld, S. Bolognesi, D. Fehling, A.V. Gritsan, P. Maksimovic, C. Martin, M. Swartz, M. Xiao

The University of Kansas, Lawrence, USA
P. Baringer, A. Bean, G. Benelli, C. Bruner, J. Gray, R.P. Kenny III, D. Majumder, M. Malek, M. Murray, D. Noonan, S. Sanders, J. Sekaric, R. Stringer, Q. Wang, J.S. Wood

Kansas State University, Manhattan, USA
I. Chakaberia, A. Ivanov, K. Kaadze, S. Khalil, M. Makouski, Y. Maravin, L.K. Saini, N. Skhirtladze, I. Svintradze

Lawrence Livermore National Laboratory, Livermore, USA
J. Gronberg, D. Lange, F. Rebassoo, D. Wright

University of Maryland, College Park, USA
A. Baden, A. Belloni, B. Calvert, S.C. Eno, J.A. Gomez, N.J. Hadley, S. Jabeen, R.G. Kellogg, T. Kolberg, Y. Lu, A.C. Mignerey, K. Pedro, A. Skuja, M.B. Tonjes, S.C. Tonwar

Massachusetts Institute of Technology, Cambridge, USA
A. Apyan, R. Barbieri, K. Bierwagen, W. Busza, I.A. Cali, L. Di Matteo, G. Gomez Ceballos, M. Goncharov, D. Gulhan, M. Klute, Y.S. Lai, Y.-J. Lee, A. Levin, P.D. Luckey, C. Paus, D. Ralph, C. Roland, G. Roland, G.S.F. Stephans, K. Sumorok, D. Velicanu, J. Veverka, B. Wyslouch, M. Yang, M. Zanetti, V. Zhukova

University of Minnesota, Minneapolis, USA
B. Dahmes, A. Gude, S.C. Kao, K. Klapoetke, Y. Kubota, J. Mans, S. Nourbakhsh, R. Rusack, A. Singovsky, N. Tambe, J. Turkewitz

University of Mississippi, Oxford, USA
J.G. Acosta, S. Oliveros

University of Nebraska-Lincoln, Lincoln, USA
E. Avdeeva, K. Bloom, S. Bose, D.R. Claes, A. Dominguez, R. Gonzalez Suarez, J. Keller, D. Knowlton, I. Kravchenko, J. Lazo-Flores, F. Meier, F. Ratnikov, G.R. Snow, M. Zvada

State University of New York at Buffalo, Buffalo, USA
J. Dolen, A. Godshalk, I. Iashvili, A. Kharchilava, A. Kumar, S. Rappoccio

Northeastern University, Boston, USA
G. Alverson, E. Barberis, D. Baumgartel, M. Chasco, A. Massironi, D.M. Morse, D. Nash, T. Orimoto, D. Trocino, R.-J. Wang, D. Wood, J. Zhang

Northwestern University, Evanston, USA
K.A. Hahn, A. Kubik, N. Mucia, N. Odell, B. Pollack, A. Pozdnyakov, M. Schmitt, S. Stoynev, K. Sung, M. Velasco, S. Won

University of Notre Dame, Notre Dame, USA
A. Brinkerhoff, K.M. Chan, A. Drozdetskiy, M. Hildreth, C. Jessop, D.J. Karmgard, N. Kellams, K. Lannon, S. Lynch, N. Marinelli, Y. Musienko[28], T. Pearson, M. Planer, R. Ruchti, G. Smith, N. Valls, M. Wayne, M. Wolf, A. Woodard

The Ohio State University, Columbus, USA
L. Antonelli, J. Brinson, B. Bylsma, L.S. Durkin, S. Flowers, A. Hart, C. Hill, R. Hughes, K. Kotov, T.Y. Ling, W. Luo, D. Puigh, M. Rodenburg, B.L. Winer, H. Wolfe, H.W. Wulsin

Princeton University, Princeton, USA
O. Driga, P. Elmer, J. Hardenbrook, P. Hebda, S.A. Koay, P. Lujan, D. Marlow, T. Medvedeva, M. Mooney, J. Olsen, P. Piroué, X. Quan, H. Saka, D. Stickland[2], C. Tully, J.S. Werner, A. Zuranski

University of Puerto Rico, Mayaguez, USA
E. Brownson, S. Malik, H. Mendez, J.E. Ramirez Vargas

Purdue University, West Lafayette, USA
V.E. Barnes, D. Benedetti, D. Bortoletto, M. De Mattia, L. Gutay, Z. Hu, M.K. Jha, M. Jones, K. Jung, M. Kress, N. Leonardo, D.H. Miller, N. Neumeister, F. Primavera, B.C. Radburn-Smith, X. Shi, I. Shipsey, D. Silvers, A. Svyatkovskiy, F. Wang, W. Xie, L. Xu, J. Zablocki

Purdue University Calumet, Hammond, USA
N. Parashar, J. Stupak

Rice University, Houston, USA
A. Adair, B. Akgun, K.M. Ecklund, F.J.M. Geurts, W. Li, B. Michlin, B.P. Padley, R. Redjimi, J. Roberts, J. Zabel

University of Rochester, Rochester, USA
B. Betchart, A. Bodek, P. de Barbaro, R. Demina, Y. Eshaq, T. Ferbel, M. Galanti, A. Garcia-Bellido, P. Goldenzweig, J. Han, A. Harel, O. Hindrichs, A. Khukhunaishvili, S. Korjenevski, G. Petrillo, M. Verzetti, D. Vishnevskiy

The Rockefeller University, New York, USA
R. Ciesielski, L. Demortier, K. Goulianos, C. Mesropian

Rutgers, The State University of New Jersey, Piscataway, USA
S. Arora, A. Barker, J.P. Chou, C. Contreras-Campana, E. Contreras-Campana, D. Duggan, D. Ferencek, Y. Gershtein, R. Gray, E. Halkiadakis, D. Hidas, S. Kaplan, A. Lath, S. Panwalkar, M. Park, S. Salur, S. Schnetzer, D. Sheffield, S. Somalwar, R. Stone, S. Thomas, P. Thomassen, M. Walker

University of Tennessee, Knoxville, USA
K. Rose, S. Spanier, A. York

Texas A&M University, College Station, USA
O. Bouhali[58], A. Castaneda Hernandez, S. Dildick, R. Eusebi, W. Flanagan, J. Gilmore, T. Kamon[59], V. Khotilovich, V. Krutelyov, R. Montalvo, I. Osipenkov, Y. Pakhotin, R. Patel, A. Perloff, J. Roe, A. Rose, A. Safonov, I. Suarez, A. Tatarinov, K.A. Ulmer

Texas Tech University, Lubbock, USA
N. Akchurin, C. Cowden, J. Damgov, C. Dragoiu, P.R. Dudero, J. Faulkner, K. Kovitanggoon, S. Kunori, S.W. Lee, T. Libeiro, I. Volobouev

Vanderbilt University, Nashville, USA
E. Appelt, A.G. Delannoy, S. Greene, A. Gurrola, W. Johns, C. Maguire, Y. Mao, A. Melo, M. Sharma, P. Sheldon, B. Snook, S. Tuo, J. Velkovska

University of Virginia, Charlottesville, USA
M.W. Arenton, S. Boutle, B. Cox, B. Francis, J. Goodell, R. Hirosky, A. Ledovskoy, H. Li, C. Lin, C. Neu, E. Wolfe, J. Wood

Wayne State University, Detroit, USA
C. Clarke, R. Harr, P.E. Karchin, C. Kottachchi Kankanamge Don, P. Lamichhane, J. Sturdy

University of Wisconsin, Madison, USA
D.A. Belknap, D. Carlsmith, M. Cepeda, S. Dasu, L. Dodd, S. Duric, E. Friis, R. Hall-Wilton, M. Herndon, A. Hervé, P. Klabbers, A. Lanaro, C. Lazaridis, A. Levine, R. Loveless, A. Mohapatra, I. Ojalvo, T. Perry, G.A. Pierro, G. Polese, I. Ross, T. Sarangi, A. Savin, W.H. Smith, D. Taylor, C. Vuosalo, N. Woods

†: Deceased
1: Also at Vienna University of Technology, Vienna, Austria
2: Also at CERN, European Organization for Nuclear Research, Geneva, Switzerland
3: Also at Institut Pluridisciplinaire Hubert Curien, Université de Strasbourg, Université de Haute Alsace Mulhouse, CNRS/IN2P3, Strasbourg, France
4: Also at National Institute of Chemical Physics and Biophysics, Tallinn, Estonia
5: Also at Skobeltsyn Institute of Nuclear Physics, Lomonosov Moscow State University, Moscow, Russia
6: Also at Universidade Estadual de Campinas, Campinas, Brazil
7: Also at Laboratoire Leprince-Ringuet, Ecole Polytechnique, IN2P3-CNRS, Palaiseau, France
8: Also at Joint Institute for Nuclear Research, Dubna, Russia
9: Also at Suez University, Suez, Egypt
10: Also at Cairo University, Cairo, Egypt
11: Also at Fayoum University, El-Fayoum, Egypt
12: Also at British University in Egypt, Cairo, Egypt
13: Now at Ain Shams University, Cairo, Egypt
14: Also at Université de Haute Alsace, Mulhouse, France
15: Also at Brandenburg University of Technology, Cottbus, Germany
16: Also at Institute of Nuclear Research ATOMKI, Debrecen, Hungary
17: Also at Eötvös Loránd University, Budapest, Hungary
18: Also at University of Debrecen, Debrecen, Hungary
19: Also at University of Visva-Bharati, Santiniketan, India
20: Now at King Abdulaziz University, Jeddah, Saudi Arabia
21: Also at University of Ruhuna, Matara, Sri Lanka
22: Also at Isfahan University of Technology, Isfahan, Iran
23: Also at University of Tehran, Department of Engineering Science, Tehran, Iran
24: Also at Plasma Physics Research Center, Science and Research Branch, Islamic Azad University, Tehran, Iran
25: Also at Università degli Studi di Siena, Siena, Italy
26: Also at Centre National de la Recherche Scientifique (CNRS) - IN2P3, Paris, France
27: Also at Purdue University, West Lafayette, USA
28: Also at Institute for Nuclear Research, Moscow, Russia
29: Also at St. Petersburg State Polytechnical University, St. Petersburg, Russia
30: Also at National Research Nuclear University "Moscow Engineering Physics

Institute" (MEPhI), Moscow, Russia
31: Also at California Institute of Technology, Pasadena, USA
32: Also at INFN Sezione di Padova; Università di Padova; Università di Trento (Trento), Padova, Italy
33: Also at Faculty of Physics, University of Belgrade, Belgrade, Serbia
34: Also at Facoltà Ingegneria, Università di Roma, Roma, Italy
35: Also at Scuola Normale e Sezione dell'INFN, Pisa, Italy
36: Also at University of Athens, Athens, Greece
37: Also at Paul Scherrer Institut, Villigen, Switzerland
38: Also at Institute for Theoretical and Experimental Physics, Moscow, Russia
39: Also at Albert Einstein Center for Fundamental Physics, Bern, Switzerland
40: Also at Gaziosmanpasa University, Tokat, Turkey
41: Also at Adiyaman University, Adiyaman, Turkey
42: Also at Mersin University, Mersin, Turkey
43: Also at Cag University, Mersin, Turkey
44: Also at Piri Reis University, Istanbul, Turkey
45: Also at Anadolu University, Eskisehir, Turkey
46: Also at Ozyegin University, Istanbul, Turkey
47: Also at Izmir Institute of Technology, Izmir, Turkey
48: Also at Necmettin Erbakan University, Konya, Turkey
49: Also at Mimar Sinan University, Istanbul, Istanbul, Turkey
50: Also at Marmara University, Istanbul, Turkey
51: Also at Kafkas University, Kars, Turkey
52: Also at Yildiz Technical University, Istanbul, Turkey
53: Also at Rutherford Appleton Laboratory, Didcot, United Kingdom
54: Also at School of Physics and Astronomy, University of Southampton, Southampton, United Kingdom
55: Also at University of Belgrade, Faculty of Physics and Vinca Institute of Nuclear Sciences, Belgrade, Serbia
56: Also at Argonne National Laboratory, Argonne, USA
57: Also at Erzincan University, Erzincan, Turkey
58: Also at Texas A&M University at Qatar, Doha, Qatar
59: Also at Kyungpook National University, Daegu, Korea